AN INVESTIGATION OF VELOCITY AND TEMPERATURE FIELDS IN TAYLOR-COUETTE FLOWS

Thesis by

Rajesh Kedia

In Partial Fulfillment of the Requirements

for the Degree of

Doctor of Philosophy

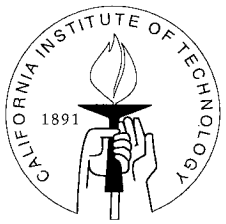

California Institute of Technology

Pasadena, California

1997

(Submitted May 15, 1997)

Acknowledgements

First and foremost, I thank my advisor, Professor Melany Hunt for her guidance, support and patience in my pursuit of this research. I am immensely grateful to her for accepting me as a student and for giving me a lot of freedom in my work. Next, I owe thanks to Professor Tim Colonius for helping me with the numerical simulations and for allotting time on his computer. I would also like to acknowledge Professors Tony Leonard and Bob Moser for taking the time to discuss the numerical issues associated with the problem. I am grateful to Professors Allan Acosta and Rolf Sabersky for their interest in my work and for serving on my committee.

This research was performed in part using the CSCC parallel computer system operated by Caltech on behalf of the Concurrent Supercomputing Consortium. Access to this facility was provided by Caltech.

Last but not the least, love go to my mother for all the sacrifices she made for my education. To her I dedicate this work.

Abstract

In many experiments, especially those investigating aspects of fluid flow, it is common to observe time series data exhibiting chaos. Chaos lies in the realm of nonlinear dynamics, and specialized methods are available for the analysis of nonlinear time series. One particular method, called time delay analysis, is particularly useful for extracting information from time series representing measurements at a single point in space. In this thesis, hot-wire anemometry is used to obtain velocity time series from experiments on isothermal Taylor-Couette flow. For R/R_c=1.6, a simple limit cycle is observed, yielding an attractor of dimension 1. For R/R_c=11.1, the attractor dimension increases, and the reconstructed attractor exhibits features characteristic of a transition to turbulence. In addition, various other states and transitions of the Taylor-Couette system are studied as well.

Direct numerical simulations (DNS) have also been performed to study the effects of the gravitational and the centrifugal potentials on the stability of heated, incompressible Taylor-Couette flow. The flow is confined between two differentially heated, concentric cylinders and the inner cylinder is allowed to rotate. The Navier-Stokes equations and the coupled energy equation are solved using a spectral method. To validate the code, comparisons are made with existing linear stability analysis and with experiments. The code is used to calculate the local and average heat transfer coefficients for a fixed Reynolds number (R=100) and a range of Grashof numbers. The variation of the local coefficients of heat transfer on the cylinder surface is investi-

gated, and maps showing different stable states of the flow are presented. Calculations of the time and space averaged equivalent conductivity show that the heat transfer decreases with Grashof number in axisymmetric Taylor vortex flow regime and increases with Grashof number after the flow becomes non-axisymmetric.

The numerical simulations also demonstrate the existence of a hysteresis loop in heated Taylor-Couette flow, obtained by slowly varying the Grashof number. Two different stable states with same heat transfer are found to exist at the same Grashof number. The validity of Colburn's correlation is investigated as well; the Prandtl number dependence is found to be slightly different from $Pr^{\frac{2}{3}}$ for the range of Reynolds number investigated. Finally, a time delay analysis of the radial velocity and the local heat transfer coefficient time series obtained from the numerical simulation of the radially heated Taylor-Couette flow is performed. The two-dimensional projection of the reconstructed attractor shows a limit cycle for Gr=-1700. The limit cycle behavior disappears at Gr=-2100, and the reconstructed attractor becomes irregular. The attractor dimension increases to about 3.2 from a value of 1 for the limit cycle case.

Contents

List of Figures

List of Tables

Nomenclature

A	acceleration ratio, $\omega^2 r_i/g$
$\ddot{A}, \ddot{B}, \ddot{C}, \ddot{D}$	matrices
$a(j,t)$	coefficients
B	body force
b	gap width, $(r_o - r_i)$
C	Courant number
C_f	friction factor
C_p	heat capacity at constant pressure
$C(\tau)$	auto-correlation function
c	wave speed
D	mass diffusivity of the fluid
D_q	generalized dimension
D_1	pointwise dimension
D_2	correlation dimension
d	number of degrees of freedom
$E(k)$	energy spectrum
F	external force field
$F^{(t)}(x)$	local map
$\dot{F}, \dot{G}$	column vectors

f	frequency of heat transfer coefficient fluctuation,
	forcing function (nonlinear terms in the Navier-Stokes equations)
f_c	inner cylinder frequency
f_{sp}	normalized fundamental frequency in the power spectrum
	of n=2 spiral flow
f_w	normalized fundamental frequency in the power spectrum
	of isothermal flow
$f(Pr)$	function of Pr
$f(Pr, Gr)$	function of Pr and Gr
G	torque
Gr	Grashof number, $g\beta(T_1 - T_2)b^3/\nu^2$
g	acceleration due to gravity,
	forcing function (nonlinear terms in the energy equation)
g_l, h_l	quasi-orthogonal trial functions
h	local heat transfer coefficient,
	height of the annulus
$h_{\bar{\theta},\bar{z},\bar{t}}$	spatially and temporally averaged heat transfer coefficient
$I(\tau)$	mutual information function
K_{eq}	mean equivalent conductivity, $r_i \ln(1/\eta) h_{\bar{\theta},\bar{z},\bar{t}}/k$
K_z, K_θ	wave numbers in the z and θ directions
k	thermal conductivity of the fluid,
	magnitude of the wave number vector
L	number of radial modes
L_z, L_θ	periods in the z and θ directions
L_z	normalized axial wavelength, λ/b
L_1, L_2	linear operators

m	local mass transfer coefficient,
	number of azimuthal waves
N_z, N_θ	number of modes in the z and θ directions
$N(\epsilon)$	number of points in a hyper-sphere of radius ϵ
Nu	Nusselt number, $2hb/k$
n	number of starts $(2\pi r_o \tan\Psi/L_z)$,
	time level
$\hat{n}$	normal vector
P	pressure
Pr	Prandtl number, ν/α
$P(X), P(Y)$	probability density
$P(X,Y)$	joint probability density
Q_m, P_m	quasi-orthogonal test functions
R	Reynolds number, $\omega r_i b/\nu$
R_c	critical Reynolds number for the onset of Taylor vortex flow
r, θ, z	cylindrical coordinates
r_i	inner cylinder radius
r_o	outer cylinder radius
Sc	Schmidt number, ν/D
Sh	Sherwood number, $2mb/D$
St	Stanton number
S_{rel}	relative speed of the scalar machine with respect
	to each parallel processor
T	temperature field
T_C	steady state conduction temperature solution
T_l	Chebyshev polynomial of order l

T_s	truncated temperature series solution
T_1	inner cylinder temperature
T_2	outer cylinder temperature
$\overline{T_o}$	dimensionless reference temperature
t	time
t_p	computation time taken by a parallel machine
t_s	computation time taken by a scalar machine
u_r, u_θ, u_z	velocity components in cylindrical coordinate system
u_l	velocity r-trial functions
$\overline{u}_\theta$	z-averaged tangential velocity
V	velocity field
V_s	truncated velocity series solution
V_{CF}	circular Couette flow velocity solution
$v(t)$	time series
W	vorticity, $\nabla \times V$
Γ	aspect ratio, h/b
α_{jml}	expansion coefficients for velocity
γ_{jml}	expansion coefficients for temperature
ϵ	radius of the hyper-sphere
ω	inner cylinder angular velocity
ρ	density of the fluid
ν	kinematic viscosity of the fluid
μ	dynamic viscosity of the fluid
α	thermal diffusivity of the fluid
β	thermal expansion coefficient of the fluid
β^*	$\beta(T_1 - T_2)$

λ	wavelength of a pair of vortices
η	radius ratio, r_i/r_o
σ	eigenvalue
τ	delay time
τ_l	temperature r-trial functions
$\tau_w\|_{\overline{\theta},\overline{z},\overline{t}}$	spatially and temporally averaged wall shear stress
Ψ	the angle of inclination of the Taylor cells from the horizontal
ψ_m	temperature r-test functions
$\Phi_j(x)$	a basis set
$\chi(t,\ \tau)$	time delay vectors
ξ_m	velocity r-test functions
Δt	time step of integration
$\Delta r, \Delta\theta, \Delta z$	grid spacing in the radial, circumferential and axial directions
$\Delta\phi$	phase angle between the modulation of successive azimuthal waves
$\widehat{\nabla\times}$	Fourier-transformed curl operator
$\widehat{\nabla\times^*}$	complex conjugate Fourier-transformed curl operator

Chapter 1

Introduction

1.1 Motivation

The transition from laminar to turbulent flow is not well understood. Taylor-Couette flow consists of the flow in the annulus between two (possibly rotating) concentric circular cylinders is a convenient fluid system to study transition and turbulence. It is not difficult to construct; the flow is not very sensitive to small imperfections of the experimental setup; the rotation rates of the inner cylinder can also be controlled to a very high degree of accuracy. The Taylor-Couette problem offers a range of features in the transition to turbulence which have been studied for over 40 years. Circular Couette flow is a well behaved laminar flow to which exact solutions exist. As the driving force is increased by increasing the speed of the inner cylinder, the system unveils rich characteristics of nonlinear dynamical systems. The transition to turbulence is slow, and with each transition, a new feature is added to the flow. The flow passes through a chaotic regime on its route to fully-developed turbulence as the control parameter (Reynolds number) is increased. It is widely believed that the chaotic flow might contain information important to the understanding of turbulent flow.

In addition to theoretical studies of transition and turbulence, the Taylor-Couette system is also in a number of engineering devices. For example, in Boiling Water Reactor (BWR) power plants, high-speed pumps are used to transport water at high pressure and temperature. A simple sketch (Shih, 1994) of such a pump is shown in Fig. 1.1. The temperature of hot water is around 280°C. Clean and cold water at 65°C is injected into the annular space between the shaft and the shaft cover. This keeps the annulus free of foreign dirt particles and also lowers the temperature of the rotating shaft. The hot reactor water and the injected cold water create a thermal mixing region. Over the past decade, maintenance inspections have revealed cracks up to 6mm deep on both the shaft and the shaft cover of such pumps; these cracks arise after approximately 20,000 to 30,000 hours of operation (Kato, et al., 1992; Gopalakrishnan, et al., 1992). In extreme instances, these cracks actually cause pumps to fail. The manufacturers and operators of the pumps have surmised that the cracking is due to thermal loading caused by an unsteady flow. Gopalakrishnan, et al. (1992) of the pump division for BW/IP International, Inc., did a simple analytical study of such a flow and concluded that the cracks are caused by large temperature fluctuations at frequencies below 25 Hz. Kato, et al. (1992, 1993) conducted an experimental investigation by constructing a full scale mock-up pump and by simulating a similar thermal environment. Thermocouples were used to measure the temperature fluctuations on the surfaces of the shaft and the shaft cover. The study showed that the magnitude of the temperature fluctuations increased with the increase in the axial flow rate of the cold water. The results of the mock-up test also showed that the mean axial temperature distribution increased with the increase in the rotational speed of the inner cylinder. The mean axial temperature distribution also increased with decrease of the axial flow rate of the cold water. They concluded that high-amplitude, low-frequency temperature fluctuations were the main cause of

the cracks. These temperature fluctuations were also believed to be caused by a thermal mixing region formed by the inner rotating shaft and the axial through flow. To counter the problem of large temperature fluctuations, a seal purge heater was used to heat the cold water before it was injected into the annulus. The tests showed that the magnitude of temperature fluctuations were reduced significantly and after 500 hours of operation under various conditions, no thermal cracks were observed. To understand the flow near the heater area, a flow visualization study was also done. But no vortices were observed. Similar studies on temperature fluctuation mechanisms and heat transfer characteristics of fluid flow in an annular gap have been conducted by Narabayashi, et al. (1993), Shiina, et al. (1993) and Watanabe, et al. (1993).

Even though the manufacturers of these pumps believe that the seal purge heater would eliminate the cracks, there is a need for numerical simulations to understand the complex fluid motion resulting from the rotation of the shaft and the radial temperature gradients within the annulus. To predict thermal fatigue in these pumps, a thermal stress analysis would require information about the frequencies and amplitudes of the thermal environment. The aim of this work is to understand the physics that causes the temperature fluctuations and to obtain the frequency and amplitude information for the thermal stress analysis model. Other applications of this research is in the cooling of electrical motor shafts and turbine rotors (Kreith, 1968; Gardiner and Sabersky, 1978; Lee and Minkowycz, 1989). In these mechanical systems, a faster and efficient transfer of heat is important for high compactness and power density. The development of rotating devices such as heat exchangers, blood oxygenators (Strong, et al., 1976) and gas centrifuges (Wood, 1983) needs a thorough understanding of Taylor-Couette flow. Also applications include modeling of atmospheric flows (Greenspan, 1968) and techniques of chemical vapor deposition (CVD) used in semiconductor device fabrication (Singer, 1984). During the process of CVD,

the solid products of a vapor phase chemical reaction are deposited on a substrate placed on a rotating turret. The flow characteristics of the hot gases between the turret and the enclosed bell jar determines the deposition process. A very fundamental objective of the study of Taylor-Couette flow is the understanding of mechanisms that lead to the growth of laminar instabilities into turbulence.

1.2 Taylor-Couette Flow

Like the BWR pumps, most industrial applications of Taylor-Couette flow only have an inner rotating cylinder. Based on the angular velocity of the inner cylinder, a non-dimensional parameter, the Reynolds number, arises from the equations of motion. The Reynolds number is defined as, $R = \omega r_i b/\nu$. Taylor (1923), in his classic experimental and analytical paper showed that at a critical Reynolds number, the base flow became unstable to axisymmetric, counter-rotating, toroidal vortices stacked one on top of another along the axis of the concentric cylinders. These vortices were later named appropriately as Taylor vortices and correspondingly the flow as Taylor vortex flow (TVF). TVF is depicted schematically in Fig. 1.2 (White, 1991). Taylor calculated the critical wavelength and the critical speed for the onset of counter-rotating toroidal vortices by performing a linear stability analysis. His theoretically calculated values agreed remarkably well with his experiments. Taylor vortices were also seen in other flow visualization studies conducted by Burkhalter and Koschmieder (1973) and Koschmieder (1979) at higher Reynolds number.

Coles (1965) performed a flow visualization experiment with suspended aluminum particles. His experiments detected azimuthally periodic waves which traveled around the inner cylinder superposed on the Taylor cells. The transition to this "Wavy Vortex Flow" (WVF) occurred at a rotational speed approximately 20% higher than the critical speed for transition to Taylor vortices. Coles (1965) system had a radius ratio

of 0.874 and an aspect ratio of 27.9. Coles observed 26 different stable states for a fixed Reynolds number by varying the inner cylinder rotational speed slowly. Coles also recorded approximately 75 transitions from one state to another by increasing the Reynolds number from 114 to 1348. These transitions were labeled by the number of Taylor vortex pairs and the number of azimuthal waves. Therefore, he was successful in showing that the final state was not unique and depended not only on the Reynolds number but also on the history of the flow. He also concluded that, regardless of the state, the angular velocity of these waves was nearly 0.34 times the angular velocity of the inner cylinder. The wave speed was later found to be a function of radius ratio, but was correct for his experimental setup. After Coles' results were known, wavy vortices were also reported by Nissan, et al. (1963) and Schwarz, et al. (1964).

In addition to TVF and WVF, the flow undergoes a series of transitions before it becomes fully turbulent at very high rotational rates of the inner cylinder. Fenstermacher, Swinney and Gollub (1979) did an experimental investigation of the transition to chaotic Taylor-Couette flow. The cylinders had a radius ratio of 0.877 and an aspect ratio of 20. Water was used as a working fluid and the radial component of velocity was measured using Laser-Doppler Velocimetry. The power spectrum of their velocity time series at R/R_c=1.2 showed a single frequency confirming the wavy vortex flow. At R/R_c=10.06, they observed a second fundamental frequency which was two orders of magnitude lower in power than the first one. At R/R_c=12, a broad weak component was observed in the power spectrum that was classified as chaotic. At $R/R_c \approx$22, there were no sharp peaks seen in the power spectrum, which indicated the disappearance of the traveling waves. For values of the Reynolds number close to 40 times the critical Reynolds number, their results showed that the Taylor vortices still existed.

The fluid motion corresponding to the second fundamental frequency seen in the

power spectrum of Fenstermacher, et al. (1979) was identified in a flow visualization experiment conducted by Gorman and Swinney (1982). They found that the second frequency corresponded to the modulation of the azimuthal waves. They observed this modulation as a periodic flattening of the wavy-vortex outflow boundaries and named this flow regime as Modulated Wavy Vortex Flow (MWVF). With the aid of a complicated mirror arrangement and a frame-by-frame analysis of the movie films, they discovered 11 doubly periodic flow states. Each state was labeled with two integers m and k, where m denoted the number of azimuthal waves and k was related to the phase angle between the modulation of the successive azimuthal waves by $\Delta\phi = 2\pi k/m$. For k=0, all the azimuthal waves flattened at the same time and for k=1, every other wave flattened.

The flow becomes even more complex if either radial heating or superimposed axial flow (Shih and Hunt, 1992; Gardiner and Sabersky, 1978) are present or if the cylinders are eccentrically oriented (Cole, 1967; 1969). Gardiner and Sabersky measured heat transfer coefficients for the flow in the annular space between an inner rotating cylinder and an outer stationary one, with superimposed axial flow. The experiments were done with water as the working fluid for three different Prandtl numbers. They observed that heat transfer coefficients increased with the onset of Taylor vortices. Experimental heat transfer data were also presented for four different radius ratios and for several combinations of outer to inner cylinder speeds by Bjorklund and Kays (1959). Cole's results showed that eccentricity had a stabilizing effect on the flow which resulted in a higher critical Reynolds number. The effects of a radial temperature gradient on the stability of Taylor-Couette flows has been the subject of considerable investigation (Ali and Weidman, 1990; Chen and Kuo, 1990).

Two dominant parameters in heated Taylor-Couette flow are the Reynolds number ($R = \omega r_i b/\nu$) and the Grashof number ($Gr = g\beta(T_1 - T_2)b^3/\nu^2$). In the definition of

Gr, T_1 and T_2 are the temperatures of the inner and the outer cylinders respectively. Typically in an experiment, the Reynolds number is increased by increasing the rotational speed of the inner cylinder and the Grashof number is increased by increasing the temperature difference between the inner and the outer cylinders. As these two parameters are varied, the flow changes from one state to another and there is a subsequent change in momentum and heat transfer characteristics. Another focus of this work is to understand these transitions and document the transport properties.

Stability analyses show that when gravity is neglected and the Reynolds number is sufficiently high that the Taylor cells are stabilized when $T_1 > T_2$ and destabilized when $T_2 > T_1$ (Yih, 1961; Lai, 1962; Becker and Kaye, 1962; Walowit, Tsao and DiPrima, 1964). Roesner (1978) included the effect of gravity through the Boussinesq approximation (Gray and Giorgini, 1976) but only considered axisymmetric disturbances. He showed that isothermal Taylor cells are stabilized by both negative and positive radial heating, and the stability boundaries are perfect symmetric with respect to the direction of radial heating. Ali and Weidman (1990) tested stability with respect to non-axisymmetric disturbances of both toroidal and helical type and found that the number of critical modes increased dramatically for large radius ratio. Chen and Kuo (1990) took into account the effects of both the centrifugal and gravitational potential on the axisymmetric stability problem. They concluded that the stability boundary depended on the ratio of the centrifugal and the gravitational potentials, the Prandtl number and the Grashof number.

Snyder and Karlsson (1964) performed an experimental study with a small annulus using glycerine/water mixtures. They found that small temperature gradients, both positive and negative, stabilized the Taylor cells, and that heating the inner cylinder was slightly more stabilizing than heating the outer one. They also observed that sufficiently large temperature gradients destabilized the flow, causing a spiral

form of instability, and concluded that stability is affected by the axial flow induced by gravity. Sorour and Coney (1979) used oil of high Prandtl number to conduct experiments in a small annular gap. They reported flow destabilization for small positive temperature gradients, and they observed only toroidal vortices over the whole range of their experimental parameters. The discrepancy between these two experiments may be due to a large difference in the Prandtl number of the fluids used. A novel experimental study was performed by Kataoka, et al. (1977) with the aid of an electrochemical technique under the assumption of analogy between heat and mass transfer. They reported that the regular sinusoidal variation of the Sherwood number (Sh) is distorted by an added axial flow and both the mean and the amplitude are greatly reduced. Ball and co-workers (1989) performed a parametric study of the mean heat transfer rates across the annular gap for three different radius ratios. Their results show that the heat transfer can be described by a power-law relationship and correlated as functions of the Reynolds number and radius ratio.

Numerical simulations for axisymmetric, isothermal Taylor-Couette flow have been performed by Meyer (1967) using a finite difference technique. Computation of steady axisymmetric Taylor vortex flow by a transient implicit method was also performed by Alziary De Roquefort, et al. (1978). Numerical computation of time-dependent Taylor vortex flows in a finite-length annulus was done by Neitzel (1984). The transient development of a Taylor vortex structure was discussed and the axial wavelength was compared with experimental results for an impulsively started cylinder. Wave speeds of traveling waves have also been computed numerically for axially periodic flows in infinite-length cylinders with a pseudospectral technique by King, et al. (1984). Their computations show that the wave speed for a given radius ratio decreases with increasing Reynolds number until a plateau is reached. In this plateau region, the wave speed normalized by the inner cylinder rotation frequency increases

monotonically from 0.14 at η=0.63 to 0.45 at η=0.95. They also concluded that there was a much weaker dependence of the wave speed on the axial wavelength, azimuthal wave number, and the aspect ratio. The transition from Taylor vortex flow to wavy vortex flow was also numerically studied by Edwards, Beane and Varma (1991). Their results of the critical Reynolds number for the onset of wavy vortex flow, azimuthal wave numbers and wave speeds were in good agreement with experimental values for a radius ratio of 0.87 and aspect ratios between 8 and 34. Similar computations of Taylor vortex flow and wavy vortex flow were also presented by Marcus (1984). He used a fractional step scheme and solved the equations pseudospectrally. Marcus conjectured that the traveling waves were a secondary instability caused by the strong radial motion in the outflow boundaries of the Taylor vortices and were not shear instabilities associated with inflection points of the azimuthal flow. He also demonstrated numerically that at the point of onset of the traveling waves, the speed of the waves was equal to the angular velocity of the fluid at the center of the Taylor vortices. Coughlin and Marcus (1992) did numerical simulations of modulated waves in Taylor-Couette flow using a three-dimensional initial value code for imposed values of the axial and azimuthal periodicity. They showed that both the 'two-traveling-wave' (GS flow) and the 'non-traveling modulation' (ZS flow) were instabilities of the outflow jet between adjacent Taylor vortices. Moser, et al. (1983) used a spectral method for solving the incompressible Navier-Stokes equations between concentric cylinders.

The effects of buoyancy on bifurcation in small-to-moderate aspect ratio Taylor-Couette systems have been studied numerically by Ball and Farouk (1987, 1988). A more recent numerical work by Kuo and Ball (1997) in a wide gap, $\eta = 0.5$, and a finite aspect ratio, $\Gamma = 10$, show onset of spiral flow in certain Reynolds number and Grashof number parameter space.

When the centrifugal acceleration is of the same order as the acceleration due

to gravity, the density variation of the fluid becomes important for instabilities that are primarily centrifugal. The effect of this density variation is accounted for in the centrifugal term, in addition to the Boussinesq approximation for gravity. Therefore the present study examines the interaction of gravitational and centrifugal potentials with the radial temperature gradient. The simulations reported here are motivated by the need to characterize the thermal environment that is encountered during chaotic and fully turbulent flows. The method by Moser, et al. (1983) is extended to solve both the heat equation and the equations of motion, which are coupled through the centrifugal and gravitational potentials.

1.3 Dynamical Systems and Deterministic Chaos

In any fluid system, the motion of a fluid particle is governed by the Navier-Stokes equations and the equation of continuity, with constraints imposed by the boundary. These equations together with the appropriate boundary conditions constitutes a dynamical system. The solution of these equations gives the time evolution of the system. It is very important to characterize a dynamical system quantitatively by a few meaningful numbers, called invariants of the system. These invariants help in classifying or identifying the physical source of the observations and provide means to make models for prediction and control of the nonlinear system.

The irregular, chaotic motion that is generated by nonlinear systems whose dynamical laws uniquely determine the time evolution of a state of the system from a knowledge of its previous history is called deterministic chaos (Schuster, 1987). Nonlinearity is a necessary but not a sufficient condition for a dynamical system to exhibit chaos. The observed chaotic behavior in time is neither due to external sources of noise nor to an infinite number of degrees of freedom. The reason for irregular motion

is the property of the nonlinear system of separating initially close trajectories exponentially fast in a bounded region of phase space. It is therefore practically impossible to predict the long-time behavior of chaotic dynamical systems, because in practice the initial conditions can only be fixed with some finite accuracy.

1.3.1 Dynamical systems

The simplest example of a dynamical system is the linear harmonic oscillator. The equation of motion of such a system can easily be derived as :

$$\frac{d^2x}{dt^2} = -x \tag{1.1}$$

Usually, this is written as a system of two first-order ordinary differential equations:

$$\begin{aligned} \frac{dx}{dt} &= +y \\ \frac{dy}{dt} &= -x \end{aligned} \tag{1.2}$$

The solution of the linear harmonic oscillator with the initial conditions; $x(0) = x_o$, $y(0) = 0$ is $x = x_o \cos t$, $y = -x_o \sin t$. Shown in Fig. 1.3 are the solutions which are periodic orbits in the phase space, (x,y). The trajectory is a limit cycle which repeats itself every period. For two incommensurate frequencies associated with the motion, the trajectory would be quasi-periodic. If this were plotted in a three-dimensional phase space, it would look like a donut shaped structure called a torus. In general, if there were q incommensurate frequencies, the motion would be q-periodic.

A more complex example of a nonlinear dynamical system is the damped oscillator. The equations are :

$$\begin{aligned} \frac{dx}{dt} &= +y \\ \frac{dy}{dt} &= -\sin x - y \end{aligned} \tag{1.3}$$

The system has damping and it will eventually come to rest at the fixed point of the system, (x=0,y=0). This stationary point is the simplest example of an attractor (Fig. 1.4). An attractor is the limit set of the trajectory as time goes to infinity. The basin of attraction is the set of states in phase space in which all initial conditions approach the attractor.

1.3.2 Chaotic attractors

A chaotic attractor has the following properties:

i. The motion is bounded in phase space.

ii. The motion is deterministic.

iii. The motion is sensitive to initial conditions.

The first property means that the motion occurs in some finite region of the phase space. The second property means that if the equations of motion were solved exactly, the trajectory in the phase space would be known exactly for all times. The third property is what is called SIC (Sensitive dependence on Initial Conditions). This means that the evolution of the system from two slightly different initial conditions will be totally different. The two trajectories will diverge exponentially in time, no matter how close they are. This divergence can be quantized by a positive Lyapunov

exponent. Lyapunov exponents characterize the exponentially fast divergence or convergence of nearby trajectories in phase space. If the Lyapunov exponent is negative, the divergence decreases with time. For limit cycles, the Lyapunov exponent is zero and the trajectories stay close to each other at all times.

For the trajectories to diverge exponentially yet remain bounded, the attractor undergoes continuous stretching and folding. The chaotic attractor has a highly complex topology, which is usually fractal. Due to this fractal nature of the attractor, its dimension is always a non-integer. The dimension of a point, a line and a torus is zero, one and two respectively. Another important characteristic of a chaotic attractor is that the motion on the attractor is aperiodic. Therefore, a frequency spectrum from a chaotic dynamical system is broad-banded, but it is important to note that a broad-band frequency spectrum is insufficient by itself to classify a system as chaotic.

1.3.3 Transitions in Taylor-Couette flow

Taylor-Couette flow is a nonlinear and dissipative dynamical system. The forcing comes from the inner rotating cylinder. This flow undergoes various transitions (Brandstater and Swinney, 1987) as the rotation rate of the inner cylinder is increased. The experimental facility of Brandstater, et al. (1987) had a radius ratio of 0.875 and an aspect ratio of 20.

On starting the rotation of the inner cylinder, the first flow encountered is circular Couette flow. The only non-zero velocity is the azimuthal velocity, which has a radial dependence. This is time independent and corresponds to a fixed point. Upon increasing the Reynolds number, the next transition is to Taylor Vortex Flow (TVF) at a critical Reynolds number ($R_c = 118.4$). The Taylor Vortex Flow arises from symmetrical supercritical steady bifurcations from the base flow. The flow is still time independent but periodic in the axial direction. This also corresponds to a

fixed point. Upon further increasing the Reynolds number, another transition is made to Wavy Vortex Flow (WVF) at approximately R/R_c=1.3. The Wavy Vortex Flow is a time-periodic supercritical bifurcation (a Hopf bifurcation) from Taylor Vortex Flow to Wavy Vortex Flow. This is a first time-dependent solution with breaking of the azimuthal symmetry. The waves travel around the cylinder with a constant speed. The trajectory is a limit cycle in phase space and hence the corresponding attractor dimension is 1. A power spectrum would show a fundamental frequency corresponding to the azimuthal wave number and its harmonics. As the Reynolds number is increased further, Modulated Wavy Vortex Flow (MWVF) is formed at R/R_c=10. This is doubly-periodic with an attractor dimension of 2. There are two incommensurate frequencies and the flow is on a torus. At even higher Reynolds number (R/R_c=11.7), the flow becomes chaotic or "weakly turbulent". The calculated fractal dimension is 2.4 for R/R_c=12.4. The largest Lyapunov exponent becomes positive and the frequency spectrum is broad-banded. Hereafter, with the continuous increase of Reynolds number, the flow becomes "fully turbulent" and the fractal dimension continues to increase monotonically. The aim of the experimental part of this thesis is to determine whether such a "weakly turbulent" or chaotic regime of the flow exists in the Taylor-Couette experimental setup, which was initially designed for high Reynolds number studies.

1.3.4 Reynolds number dependence of the attractor dimension

For a given dynamical system there is an upper limit to the value of the attractor dimension. This is simply the dimension of the phase space of the system. In the case of a dissipative dynamical system, the dimension of the space occupied by the attractor is, in general, less than the dimension of the phase space. This happens

because dissipation damps some of the degrees of freedom. For example, if the phase space is three dimensional, then the attractor dimension must be less than three. Also there can be only one positive Lyapunov exponent because the attractor is bounded. There must be at least one negative Lyapunov exponent associated with the direction of contraction because the final volume is smaller than the initial volume. There is also a zero Lyapunov exponent because different points on the same trajectory neither diverge nor contract. On the other hand, the volume in phase space of a set of trajectories is conserved for attractors in conservative systems.

Since the solutions of the Navier-Stokes equations are functions of a continuous range of spatial points, the phase space is infinite dimensional. In the derivation of these equations, it is assumed that the medium is continuous. This assumption is justified because viscosity damps out the fluid motion on a scale much larger than the distance between molecules. However, in a physical system, there is a finite number of particles per volume and thus the phase space must be finite dimensional. Mathematically, the dissipative part of the Navier-Stokes equations must restrict the solutions to a finite dimensional attractor as well. Intuitively, both the number of excited modes and the dimension of the attractor must increase with the increase in the energy input to the system. Constantin, et al., (1985) estimated that:

$$d \sim R^3 \tag{1.4}$$

where d is the number of degrees of freedom and R is the Reynolds number. This derivation had no prior knowledge that the spectrum of homogeneous isotropic turbulence is the Kolmogorov spectrum. In the inertial range, the energy spectrum exhibits a scaling behavior:

$$E(k) = k^{-n} \tag{1.5}$$

where k is the magnitude of the wave number vector and n is close to 5/3. The spectrum with n=5/3 is the famous Kolmogorov spectrum. The assumption that the energy spectrum in the flow is the Kolmogorov spectrum gives a more conventional estimate of :

$$d \sim R^{\frac{9}{4}} \tag{1.6}$$

Both the above estimates are valid for very high Reynolds number and are inapplicable at low and medium Reynolds numbers. Therefore fluid systems have a finite number of degrees of freedom, and the number of degrees of freedom generally increases with the increase in Reynolds number.

1.4 Objectives

The numerical simulations were performed with the following objectives:

i. Verify a fully spectral numerical method to study the effects of the gravitational and the centrifugal potentials on the stability of heated, incompressible Taylor-Couette flow.

ii. Document the information about the frequencies and amplitudes of the thermal environment in this flow.

iii. Map the different stable states in the flow for a fixed Reynolds number and different Grashof numbers.

iv. Calculate the local and average heat transfer coefficients in the Reynolds number and Grashof number parameter space and compare them with the existing experimental results.

v. Investigate the existence of a hysteresis loop in radially heated Taylor-Couette flow.

vi. Perform time delay analysis on local heat transfer coefficient time series obtained from the numerical simulation and calculate the dimension of the flow. The dimension can then be used for making models to predict the value of the heat transfer coefficient.

In addition to the numerical simulations, experimental studies of isothermal Taylor-Couette flow were also performed to investigate the dependence of the attractor dimension on the Reynolds number. The experiments were also conducted to verify the existence of a "chaotic regime" before the flow became fully turbulent at higher Reynolds numbers.

1.5 Organization of This Report

Chapter 2 begins with some general comments about DNS. An analogy between the Stokes equations and the Navier-Stokes and energy equations is drawn. Taylor-Couette flow with radial heating is introduced and the boundary conditions are discussed. In section 2.4, the momentum equations and the energy equation governing the velocity and the temperature fields are given. The divergence-free vector expansion solution for the velocity and the temperature are included in section 2.5. A detailed treatment of the vector functions and the quasi-orthogonal functions is provided, as is a discussion of the nonlinear terms and the time-advancement scheme. Both scalar and parallel code implementations are presented, including the corresponding speed-up. Section 2.11 presents the results of the code validation. Several cases of isothermal and heated Taylor-Couette flow were run and validated. Comparisons are also made with linear stability analysis.

A time delay analysis of velocity time series using dynamical systems methods is discussed in chapter 3. Reconstruction of the attractor, the choice of a suitable time delay, and the calculation of the attractor dimension is described in details. In section 3.2, the time delay method is validated by applying the procedure to a model system given by the Lorenz equations. A description of the experiment facility, data acquisition and velocity time series measurements using a hot-wire anemometer is also given. Various states and transitions in Taylor-Couette flow are studied and the adequacy of the experimental apparatus to study transitions in Taylor-Couette flow is investigated.

Chapter 4 contains the results. Comparisons are made with experimentally available data from two different sets of experiments. Maps of different stable states in the flow are presented. The space and time averaged heat transfer coefficient from the inner to the outer cylinder is reported. The variation of the size of the Taylor cells with increasing Grashof number is discussed. In section 4.2, a numerical study of the existence of a hysteresis loop is also conducted. The validity of Colburn's analogy is checked in section 4.3. Finally, a time delay analysis of the time series obtained from the experiments and numerical simulations of Taylor-Couette flow is performed. Also, the power spectra, the reconstructed attractor, and the estimates of the attractor dimension are given at the conclusion of the chapter.

The dissertation ends with conclusions in chapter 5 summarizing the results of the study.

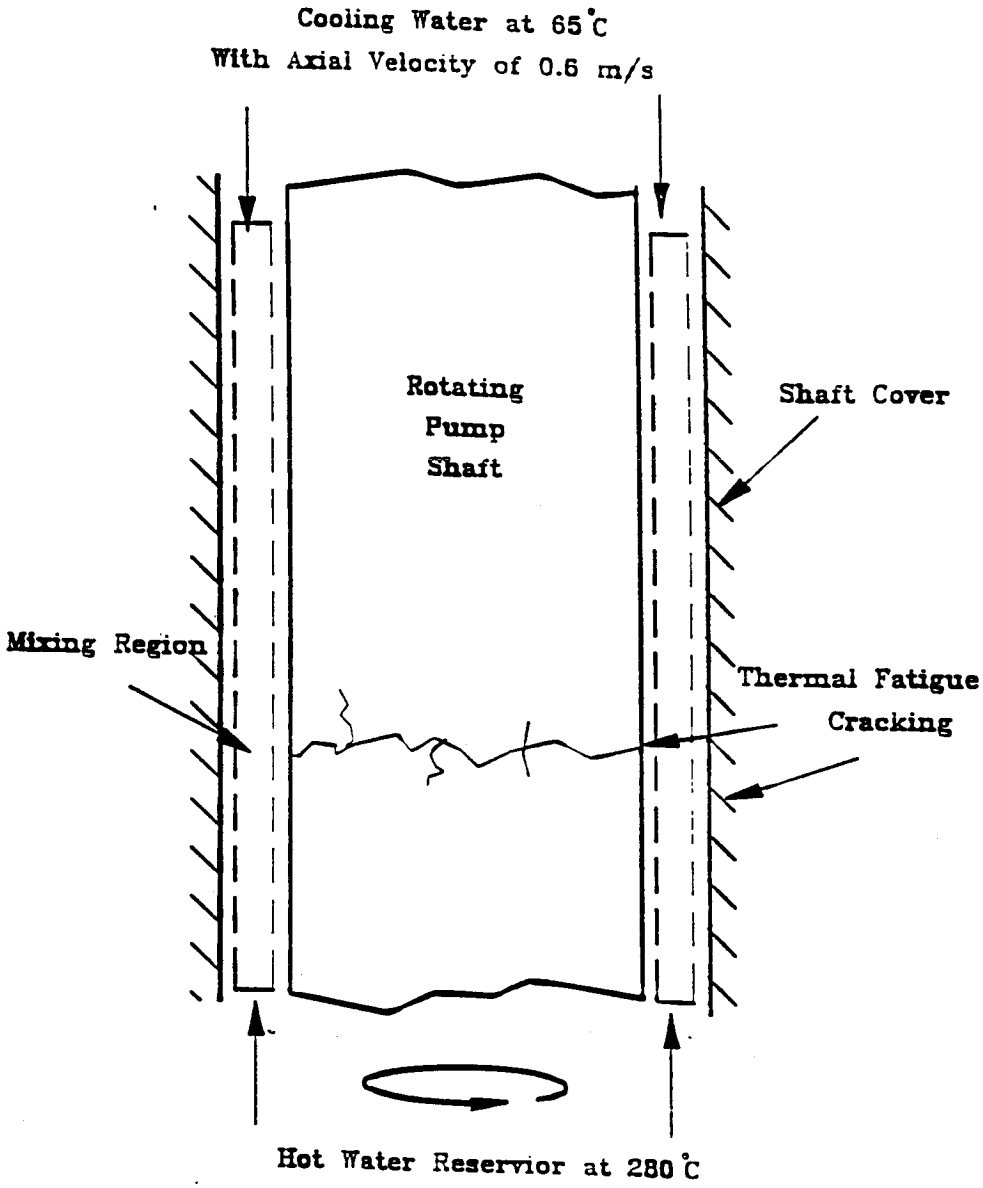

Figure 1.1: Sketch of the pump.

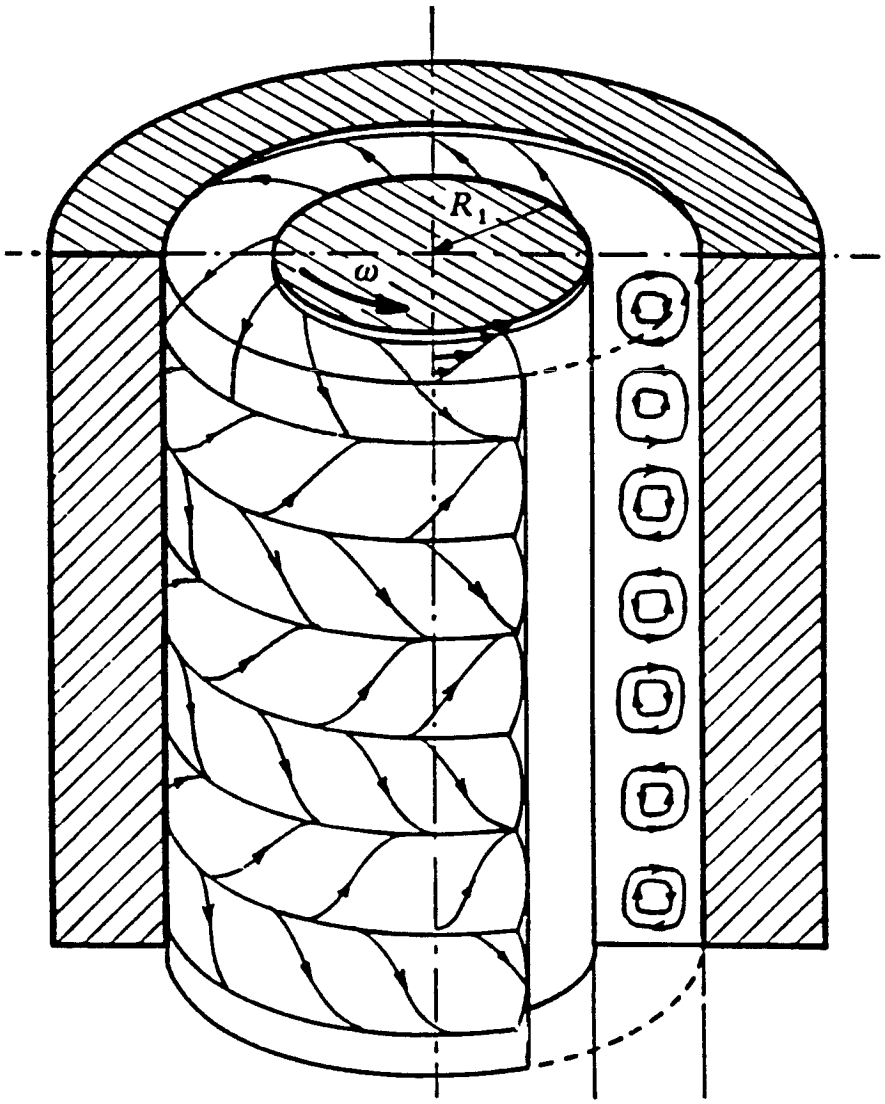

Figure 1.2: Schematic of Taylor cells.

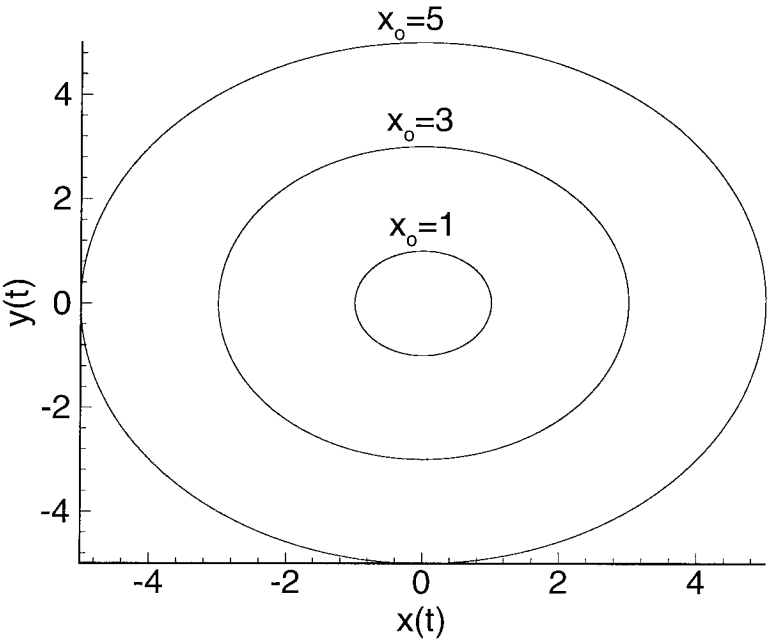

Figure 1.3: Phase space for a simple harmonic oscillator.

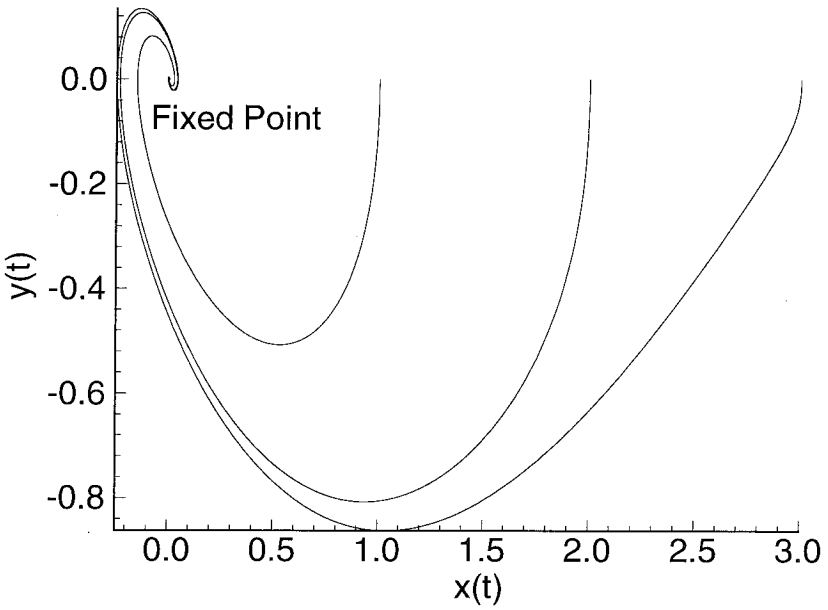

Figure 1.4: Phase space for a damped oscillator.

Chapter 2

Methodology I: Numerical Simulations

2.1 Background

With the development of large-scale sequential and parallel computers, direct numerical simulation of complex fluid flows has become feasible. Direct Numerical Simulation (DNS) is a technique for studying turbulence that compliments laboratory experiments. In DNS, the associated partial differential equations are numerically solved. Turbulent flows contain a wide range of length and time scales. The length scale is bounded above by the geometric dimension of the flow field and bounded below by the action of viscous dissipation. Hence a numerical simulation must resolve all spatial and temporal scales important in the problem. Since the range of these scales increases with Reynolds number, DNS is limited to low Reynolds numbers.

Fluid flow DNS are now routinely performed using spectral methods. The fundamental step is the reduction of the original partial differential equations to a set of ordinary differential or algebraic equations that can then be solved by existing numerical techniques. For infinitely smooth solutions, spectral methods have a very

high accuracy. The advantage of using a spectral method is not the high accuracy that can be obtained for large number of modes, but rather the small number of modes needed for a reasonably accurate solution. The use of a small number of modes becomes additionally important in three-dimensional simulations as there is a limited number of modes available in each spatial direction. If periodic boundary conditions are present in the flow, then spectral methods based on Fourier expansion functions become the natural choice. Fourier spectral methods are easy to apply to unbounded flows, but problems arise for wall-bounded flows. The imposition of the no-slip boundary conditions in the direction normal to the wall degrades the accuracy of these Fourier functions. Another constraint to the Navier-Stokes equations is the continuity equation. Both the no-slip boundary condition and the continuity constraint must be imposed at every time step during the time evolution of the incompressible Navier-Stokes equations. Moin and Kim (1980) have shown that these constraints cannot be properly enforced if an explicit time-advancement is used; the corresponding solution obtained is incorrect. On the other hand, an implicit time-advancement of the pressure and the viscous terms lead to the correct solution.

Various methods have been used for solving the three-dimensional time-dependent Navier-Stokes equations. Moin and Kim (1980) expanded the flow variables into Fourier series in the homogeneous directions and the Chebyshev polynomials in the direction normal to the wall. They solved the continuity equation directly rather than the Poisson equation for pressure. Implicit time differencing was used for the pressure and the viscous terms, while the remaining terms were treated explicitly. They concluded that by solving the continuity equation instead of the Poisson equation for pressure, and by treating the pressure and the viscous terms implicitly, the problem of a nonconvergent series solution for the dependent variables can be avoided.

Marcus, Orszag and Patera (1982) developed an initial value code to study the

various transitions in cylindrical Couette flow. The authors used a splitting scheme which consists of three time steps. The first step is an advection step in which the nonlinear terms are time-advanced explicitly, giving an intermediate velocity field. In the second step, the pressure correction is applied with the continuity constraint on the second intermediate velocity field. In the final step, the viscous correction is performed to yield the final velocity field. This final velocity field is not completely divergence-free, since the continuity equation is enforced in the second fractional step. They also reduced the time-splitting error by solving the pressure equation with an inviscid boundary condition and by using a Richardson extrapolation. Similar approaches were used by Orszag and Kells (1980) for the channel flow and by Patera and Orszag (1981) for the flow in a pipe.

Leonard and Wray (1982) developed a new numerical method for the simulation of pipe flow. They used divergence-free vector functions in the expansion of the velocity field. These vector functions also satisfied the viscous boundary conditions. A spectral representation based on Jacobi polynomials demonstrated rapid convergence of the eigenfunctions as the number of radial modes was increased. The same method was used by Moser, Moin and Leonard (1983) to solve incompressible Navier-Stokes equations in a plane channel and between concentric cylinders. For the cylinder problem, this method yielded doubly-bordered, band-diagonal matrices which were efficiently solved in $235L$ operations, where L denotes the number of radial modes.

The method of Moser, et al. (1983), is followed here. Again, the trial functions satisfy the continuity constraint and the no-slip boundary condition. Pressure in the incompressible Navier-Stokes equation is not a thermodynamic variable satisfying an equation of state, but rather an implicit dynamic variable which adjusts itself instantaneously in a time-dependent flow to satisfy the incompressibility or divergence-free condition. Hence, satisfying the continuity equation eliminates pressure and there is

no need to solve a Poisson equation if the pressure is not desired. The Navier-Stokes equations and the energy equation are solved together for the Taylor-Couette problem. The trial functions are appropriately chosen to satisfy the constant temperature boundary conditions as well.

2.2 Forced Stokes Equations

The method described by Moser, Moin and Leonard (1983) is used here for numerically solving the incompressible Navier-Stokes equations and the energy equation between two differentially heated, concentric cylinders. A part of the numerical material presented in this thesis appears in Moser, et al. (1983) but it is included here for completeness.

The forced Stokes equation is given by:

$$\begin{aligned} &\frac{\partial V}{\partial t} = -\nabla P - \frac{1}{R}\nabla \times \nabla \times V + f \\ &\nabla \cdot V = 0 \\ &V = 0 \qquad \text{at the boundaries} \end{aligned} \tag{2.1}$$

where V is the velocity field, P is the dynamic pressure and f is a known forcing function.

The Navier-Stokes equations and the energy equation are almost similar to the forced Stokes equations. The only difference is that the nonlinear terms in both the momentum and the heat equation are replaced by a known forcing function in the Stokes equations. Therefore, if these nonlinear terms are computed explicitly, any scheme for solving the forced Stokes equations can be used for solving the Navier-Stokes equations and the energy equation. The explicitly computed nonlinear terms

become the forcing function in the Stokes equations. The viscous and diffusion terms in the momentum and the heat equations are time-advanced implicitly; this method is appropriately called a mixed explicit-implicit one.

2.3 Flow Configuration

A sketch of the flow configuration in (r, θ, z) cylindrical coordinates is shown in Fig. 2.1. The radii of the inner and the outer cylinders are r_i and r_o, respectively, and the radius ratio is defined as $\eta = r_i/r_o$. The inner cylinder rotates with a constant angular velocity ω about the vertical z-axis while the outer cylinder is stationary. The two cylinders are at different uniform temperatures. The temperature of the inner cylinder is T_1 and that of the outer one is T_2. Gravity acts in the negative z-direction, which makes it perpendicular to the radial temperature gradient. The centrifugal force is parallel to the temperature gradient. The temperature difference can be assumed sufficiently small so that the density is treated as a constant everywhere in the Navier-Stokes equations, with the exception of the gravitational (z-momentum equation) and the centrifugal (r-momentum equation) terms, i.e., the Boussinesq approximation. All other fluid properties are assumed to be independent of temperature. The flow is axially periodic (i.e., infinite aspect ratio) and no-slip boundary conditions are used at the inner and the outer cylinders. Figure 2.2 shows schematically, the familiar axisymmetric counter-rotating Taylor cells. The axial distance between a pair of Taylor cells is λ and b is the gap width. The axial wavelength is normalized by the gap width to define L_z, $L_z = \lambda/b$.

2.4 Momentum and Energy Equations

The non-dimensional momentum equations are cast into the form of "forced Stokes equations" :

$$\begin{aligned} & \nabla \cdot V = 0 \\ & \frac{\partial V}{\partial t} = -\nabla P - \frac{1}{R}\nabla \times \nabla \times V + f \qquad (2.2) \\ \text{with} \quad & (u_r, u_\theta, u_z) = (0, 1, 0) \ \text{ at the inner cylinder} \\ \text{and} \quad & (u_r, u_\theta, u_z) = (0, 0, 0) \ \text{ at the outer cylinder} \end{aligned}$$

where $f = V \times W + B$, $W = \nabla \times V$ and B is the body force. The non-dimensional energy equation is given by:

$$\begin{aligned} & \frac{\partial T}{\partial t} + V \cdot \nabla T = \frac{1}{Pr\ R}\nabla^2 T \qquad (2.3) \\ \text{with} \quad & T = 1 \ \text{ at the inner cylinder} \\ \text{and} \quad & T = 0 \ \text{ at the outer cylinder} \end{aligned}$$

In the previous equations, the length scales, the velocity scales, the time scale and the dynamic pressure are non-dimensionalized by the gap width (b), the inner cylinder velocity (ωr_i), $b/\omega r_i$ and $\omega^2 {r_i}^2$ respectively. The temperature is non-dimensionalized as $(T - T_2)/(T_1 - T_2)$. The non-dimensional equations governing the flow for the velocity component (u_r, u_θ, u_z), pressure P and temperature T are (in rotational form):

Continuity:

$$\frac{\partial u_r}{\partial r} + \frac{u_r}{r} + \frac{1}{r}\frac{\partial u_\theta}{\partial \theta} + \frac{\partial u_z}{\partial z} = 0 \qquad (2.4)$$

Momentum:

$$\frac{\partial u_r}{\partial t}+\frac{u_\theta}{r}\frac{\partial u_r}{\partial \theta}+u_z\frac{\partial u_r}{\partial z}-u_z\frac{\partial u_z}{\partial r}-u_\theta\frac{\partial u_\theta}{\partial r}$$
$$-\Big(1-\beta^*(T-\overline{T_o})\Big)\frac{u_\theta^2}{r}=-\frac{\partial P}{\partial r}$$
$$+\frac{1}{R}\Big(\frac{1}{r^2}\frac{\partial^2 u_r}{\partial \theta^2}-\frac{1}{r^2}\frac{\partial u_\theta}{\partial \theta}-\frac{1}{r}\frac{\partial^2 u_\theta}{\partial \theta \partial r}+\frac{\partial^2 u_r}{\partial z^2}-\frac{\partial^2 u_z}{\partial r \partial z}\Big)$$

$$\frac{\partial u_\theta}{\partial t}+\frac{u_r u_\theta}{r}+u_r\frac{\partial u_\theta}{\partial r}-\frac{u_r}{r}\frac{\partial u_r}{\partial \theta}-\frac{u_z}{r}\frac{\partial u_z}{\partial \theta}$$
$$+u_z\frac{\partial u_\theta}{\partial z}=-\frac{1}{r}\frac{\partial P}{\partial \theta}+\frac{1}{R}\Big(\frac{1}{r}\frac{\partial u_\theta}{\partial r}\qquad(2.5)$$
$$-\frac{u_\theta}{r^2}+\frac{\partial^2 u_\theta}{\partial r^2}+\frac{1}{r^2}\frac{\partial u_r}{\partial \theta}-\frac{1}{r}\frac{\partial^2 u_r}{\partial r \partial \theta}-\frac{1}{r}\frac{\partial^2 u_z}{\partial z \partial \theta}+\frac{\partial^2 u_\theta}{\partial z^2}\Big)$$

$$\frac{\partial u_z}{\partial t}-u_r\frac{\partial u_r}{\partial z}+u_r\frac{\partial u_z}{\partial r}+\frac{u_\theta}{r}\frac{\partial u_z}{\partial \theta}-u_\theta\frac{\partial u_\theta}{\partial z}$$
$$=-\frac{\partial P}{\partial z}+\frac{1}{R}\Big(\frac{1}{r}\frac{\partial u_z}{\partial r}-\frac{1}{r}\frac{\partial u_r}{\partial z}-\frac{\partial^2 u_r}{\partial r \partial z}$$
$$+\frac{\partial^2 u_z}{\partial r^2}+\frac{1}{r^2}\frac{\partial^2 u_z}{\partial \theta^2}-\frac{1}{r}\frac{\partial^2 u_\theta}{\partial z \partial \theta}\Big)+\frac{Gr}{R^2}(T-\overline{T_o})$$

Energy:

$$\frac{\partial T}{\partial t}+u_r\frac{\partial T}{\partial r}+\frac{u_\theta}{r}\frac{\partial T}{\partial \theta}+u_z\frac{\partial T}{\partial z}=\qquad(2.6)$$
$$\frac{1}{Pr\ R}\Big(\frac{1}{r}\frac{\partial T}{\partial r}+\frac{\partial^2 T}{\partial r^2}+\frac{1}{r^2}\frac{\partial^2 T}{\partial \theta^2}+\frac{\partial^2 T}{\partial z^2}\Big)$$

where,

$$R=\frac{\omega r_i b}{\nu}\qquad Gr=\frac{g\beta(T_1-T_2)b^3}{\nu^2}$$

$$Pr=\frac{\nu}{\alpha}\qquad \beta^*=\beta(T_1-T_2)$$

Here R is the Reynolds number, Gr the Grashof number, Pr the Prandtl number,

and β^* is the non-dimensional thermal expansion coefficient of the fluid. Geometric parameters include η and L_z. Another useful parameter is the acceleration ratio, $A = \omega^2 r_i/g$, which is the ratio of the centrifugal to gravitational accelerations. It can be derived from the independent parameters ($A = R^2\beta^*[1/\eta - 1]/Gr$).

2.5 Divergence-Free Vector Expansions

The three-dimensional incompressible equations of motion, together with the energy equation, are discretized using a Chebyshev/Fourier spectral method. Writing the solution V_s and T_s as a truncated series expansion, using trial functions as basis functions:

$$V_s(r,\theta,z,t) = \sum_{K_\theta}\sum_{K_z}\sum_{l=0}^{L} \alpha_{jml}(t) u_l(r;K_\theta,K_z) e^{iK_\theta\theta} e^{iK_z z} \tag{2.7}$$

$$T_s(r,\theta,z,t) = \sum_{K_\theta}\sum_{K_z}\sum_{l=0}^{L} \gamma_{jml}(t) \tau_l(r;K_\theta,K_z) e^{iK_\theta\theta} e^{iK_z z} \tag{2.8}$$

$$\text{where} \quad K_z = j2\pi/L_z, \quad -N_z/2 \le j \le N_z/2 - 1$$
$$K_\theta = m2\pi/L_\theta, \quad -N_\theta/2 \le m \le N_\theta/2 - 1$$

where K_z and K_θ are the wave numbers, L_z and L_θ are the periods in the z and θ directions respectively. The expansion coefficients are given by $\alpha_{jml}(t)$ and $\gamma_{jml}(t)$; $u_l(r;K_\theta,K_z)$ and $\tau_l(r;K_\theta,K_z)$ are the r-trial functions for the velocity and the temperature fields chosen to satisfy the following continuity constraint and the boundary

conditions:

$$\begin{aligned} &\nabla \cdot u_l(r; K_\theta, K_z) e^{iK_\theta \theta} e^{iK_z z} = 0 \\ &u_l(r = r_i, r_o; K_\theta, K_z) = 0 \\ &\tau_l(r = r_i, r_o; K_\theta, K_z) = 0 \end{aligned} \tag{2.9}$$

For a sufficiently large number of modes N_z, N_θ and L, the velocity field $V_s(r, \theta, z, t)$ and the temperature field $T_s(r, \theta, z, t)$ are assumed to be complete and fully represent the flow.

In the method of weighted residuals (MWR), the test functions are used to ensure that the differential equation is satisfied closely by the truncated series expansion. This is achieved by minimizing the residual or the error in the differential equation produced by using the truncated series instead of the exact solution, with respect to a suitable norm. In other words, the residual satisfies an orthogonality condition with respect to each of the test functions. Test functions for the velocity ($\xi_m e^{-iK_\theta \theta} e^{-iK_z z}$) and temperature ($\psi_m e^{-iK_\theta \theta} e^{-iK_z z}$) fields are chosen such that:

$$\begin{aligned} &\nabla \cdot \xi_m(r; K_\theta, K_z) e^{-iK_\theta \theta} e^{-iK_z z} = 0 \\ &\xi_m(r = r_i, r_o; K_\theta, K_z) \cdot \hat{n} = 0 \\ &\psi_m(r = r_i, r_o; K_\theta, K_z) \cdot \hat{n} = 0 \end{aligned} \tag{2.10}$$

where $\hat{n}$ is a unit vector normal to the wall. The series expansion solutions (2.7) and (2.8) are substituted into the momentum and the energy equations (2.5) and (2.6). The equations then are dot multiplied by a set of test functions and integrated over the entire computational domain. The pressure term is eliminated from the momentum equations using integration by parts. Consequently, the following set of

equations are obtained for each wave number pair K_z and K_θ:

$$\sum_{l=0}^{L} \frac{d\alpha_l}{dt} \int_{r_i}^{r_o} \xi_m \cdot u_l \, r dr = -\frac{1}{R} \sum_{l=0}^{L} \alpha_l \int_{r_i}^{r_o} \xi_m \cdot \widehat{\nabla \times \nabla \times} u_l \, r dr + \int_{r_i}^{r_o} \xi_m \cdot \hat{f} \, r dr \tag{2.11}$$

$$\sum_{l=0}^{L} \frac{d\gamma_l}{dt} \int_{r_i}^{r_o} \psi_m \cdot \tau_l \, r dr = -\frac{1}{Pr \; R} \sum_{l=0}^{L} \gamma_l \int_{r_i}^{r_o} \psi_m \cdot \widehat{\nabla^2} \tau_l \, r dr + \int_{r_i}^{r_o} \psi_m \cdot \hat{g} \, r dr \tag{2.12}$$

where f and g are the nonlinear terms from the Navier-Stokes and the energy equations. $\hat{f}$ denote the Fourier transform of f and $\widehat{\nabla \times}$ is the Fourier-transformed curl operator. The partial differential equations are reduced to ordinary differential equations for the expansion coefficients $\alpha_{jml}(t)$ and $\gamma_{jml}(t)$. The resulting ODE's can be written as:

$$\begin{aligned} \ddot{A} \frac{d\alpha}{dt} &= \frac{1}{R} \ddot{B} \alpha + \dot{F} \\ \ddot{C} \frac{d\gamma}{dt} &= \frac{1}{Pr \; R} \ddot{D} \gamma + \dot{G} \end{aligned} \tag{2.13}$$

where

$$\ddot{A}_{m,l} = \int_{r_i}^{r_o} \xi_m \cdot u_l \; r dr$$
$$\ddot{B}_{m,l} = \int_{r_i}^{r_o} \xi_m \cdot \widehat{\nabla \times \nabla} \times u_l \; r dr$$
$$\dot{F}_m = \int_{r_i}^{r_o} \xi_m \cdot \hat{f} \; r dr$$
$$\ddot{C}_{m,l} = \int_{r_i}^{r_o} \psi_m \cdot \tau_l \; r dr$$
$$\ddot{D}_{m,l} = \int_{r_i}^{r_o} \psi_m \cdot \widehat{\nabla^2} \tau_l \; r dr$$
$$\dot{G}_m = \int_{r_i}^{r_o} \psi_m \cdot \hat{g} \; r dr$$

$\ddot{A}$, $\ddot{B}$, $\ddot{C}$ and $\ddot{D}$ are matrices and $\dot{F}$ and $\dot{G}$ are column vectors. Equation (2.13) is a system of coupled linear ordinary differential equations and can be solved using any standard numerical scheme.

2.6 Vector Functions

The present spectral method uses spectral expansion functions that inherently satisfy the boundary conditions and the divergence-free constraint. Many such functions that would satisfy the above-mentioned properties exist. The result is an immense freedom in the choice of the trial and the test functions. During the construction of the vector functions, it should be ensured that the resulting matrices $\ddot{A}$, $\ddot{B}$, $\ddot{C}$ and $\ddot{D}$ (section 2.5) have small bandwidths.

The trial functions (u_l) and the test functions (ξ_m) for the velocity are split into two classes (u_l^+, u_l^-) and (ξ_m^+, ξ_m^-). The two classes have two different functional forms. This is analogous to independently selecting two components of the velocity vector. The third component comes from the continuity constraint. It is also advan-

tageous to decouple the equations for u_l^+ from the equations for u_l^-. The reason for doing this is to make the matrices $\ddot{A}$ and $\ddot{B}$ tightly banded. The decoupling constraints are:

$$\begin{aligned}
&\int_{r_i}^{r_o} \xi_m^+ \cdot u_l^- \; r dr = 0 \\
&\int_{r_i}^{r_o} \xi_m^- \cdot u_l^+ \; r dr = 0 \\
&\int_{r_i}^{r_o} \xi_m^+ \cdot \widehat{\nabla \times \nabla} \times u_l^- \; r dr = 0 \\
&\int_{r_i}^{r_o} \xi_m^- \cdot \widehat{\nabla \times \nabla} \times u_l^+ \; r dr = 0
\end{aligned} \tag{2.14}$$

The following vectors are chosen which satisfy the decoupling constraint (2.14) :

$$u_l^+ = \widehat{\nabla \times} \begin{pmatrix} i\ g_l \\ g_l \\ 0 \end{pmatrix} = \begin{pmatrix} -i\ K_z\ g_l \\ -K_z\ g_l \\ g_l' + \frac{K_\theta + 1}{r}\ g_l \end{pmatrix}$$

$$u_l^- = \widehat{\nabla \times} \begin{pmatrix} -i\ g_l \\ g_l \\ 0 \end{pmatrix} = \begin{pmatrix} -i\ K_z\ g_l \\ K_z\ g_l \\ g_l' + \frac{1 - K_\theta}{r}\ g_l \end{pmatrix}$$

$$\xi_m^+ = \widehat{\nabla \times \nabla \times}^* \begin{pmatrix} -i\ Q_m \\ Q_m \\ 0 \end{pmatrix} \tag{2.15}$$

$$\xi_m^- = \widehat{\nabla \times \nabla \times}^* \begin{pmatrix} i\ Q_m \\ Q_m \\ 0 \end{pmatrix}$$

$$\tau_l = h_l$$

$$\psi_m = P_m$$

Here g_l, h_l, Q_m and P_m are functions of r and $\widehat{\nabla\times^*}$ is the complex conjugate Fourier-transformed curl operator. Derivative with respect to r is denoted by $'$. To enforce the boundary conditions, it is required of the r-trial and r-test functions that they satisfy the following conditions:

$$\begin{aligned} g_l(r = r_i, r_o) &= 0 \\ g_l'(r = r_i, r_o) &= 0 \\ h_l(r = r_i, r_o) &= 0 \\ Q_m(r = r_i, r_o) &= 0 \\ Q_m'(r = r_i, r_o) &= 0 \\ P_m(r = r_i, r_o) &= 0 \end{aligned} \tag{2.16}$$

Enforcing $g_l'(r = r_i, r_o) = 0$, constrains the tangential velocity u_θ to satisfy the condition:

$$\left.\frac{\partial u_\theta}{\partial r}\right|_{r=r_i,r_o} = 0 \tag{2.17}$$

There is no physical reason for the tangential velocity to satisfy the above derivative condition. To eliminate this problem, two extra vectors are added to the test and the trial functions:

$$u_l^o = \begin{pmatrix} 0 \\ -2\ K_z\ h_l \\ \frac{2\ K_\theta}{r}\ h_l \end{pmatrix} \tag{2.18}$$

$$\xi_m^o = \begin{pmatrix} i\ K_\theta\ P_m \\ r\ P_m' + P_m \\ 0 \end{pmatrix}$$

Since $h_l'(r = r_i, r_o) \neq 0$, $\partial u_\theta / \partial r$ can now have any arbitrary value at the walls, selected by the appropriate solution. With the selection of all the vector functions, the resulting ODE's are:

$$\begin{aligned}
\ddot{A}_+^+ \frac{d\alpha^+}{dt} + \ddot{A}_o^+ \frac{d\alpha^0}{dt} &= \frac{1}{R}(\ddot{B}_+^+ \alpha^+ + \ddot{B}_o^+ \alpha^0) + \dot{F}^+ \\
\ddot{A}_-^- \frac{d\alpha^-}{dt} + \ddot{A}_o^- \frac{d\alpha^0}{dt} &= \frac{1}{R}(\ddot{B}_-^- \alpha^- + \ddot{B}_o^- \alpha^0) + \dot{F}^- \\
\ddot{A}_+^o \frac{d\alpha^+}{dt} + \ddot{A}_-^o \frac{d\alpha^-}{dt} + \ddot{A}_o^o \frac{d\alpha^o}{dt} &= \frac{1}{R}(\ddot{B}_+^o \alpha^+ + \ddot{B}_-^o \alpha^- + \ddot{B}_o^o \alpha^o) + \dot{F}^o \\
\ddot{C} \frac{d\gamma}{dt} &= \frac{1}{Pr\ R} \ddot{D} \gamma + \dot{G}
\end{aligned} \tag{2.19}$$

where the matrices $\ddot{A}$, $\ddot{B}$, $\ddot{C}$ and $\ddot{D}$ are given by:

$$\begin{aligned}
(\ddot{A}_b^a)_{m,l} &= \int_{r_i}^{r_o} \xi_m^a \cdot u_l^b \ r dr \\
(\ddot{B}_b^a)_{m,l} &= \int_{r_i}^{r_o} \xi_m^a \cdot \widehat{\nabla \times \nabla \times} u_l^b \ r dr \\
\ddot{C}_{m,l} &= \int_{r_i}^{r_o} \psi_m \cdot \tau_l \ r dr \\
\ddot{D}_{m,l} &= \int_{r_i}^{r_o} \psi_m \cdot \widehat{\nabla^2} \tau_l \ r dr
\end{aligned}$$

and the vectors $\dot{F}$ and $\dot{G}$ are:

$$\begin{aligned}
\dot{F}_m^a &= \int_{r_i}^{r_o} \xi_m^a \cdot \hat{f} \ r dr \\
\dot{G}_m &= \int_{r_i}^{r_o} \psi_m \cdot \hat{g} \ r dr
\end{aligned}$$

The subscript (b) and superscript (a) of $\ddot{A}$, $\ddot{B}$ and $\dot{F}$ can be $+$, $-$ or o. For the case $K_z = 0$ and $K_\theta \neq 0$, the following vectors are used:

$$u_l^+ = \begin{pmatrix} -i\frac{K_\theta}{r} g_l \\ g_l' \\ 0 \end{pmatrix}, \qquad u_l^- = \begin{pmatrix} 0 \\ 0 \\ h_l \end{pmatrix} \tag{2.20}$$

$$\xi_m^+ = \begin{pmatrix} i\ \frac{K_\theta}{r}\ Q_m \\ Q_m' \\ 0 \end{pmatrix}, \qquad \xi_m^- = \begin{pmatrix} 0 \\ 0 \\ P_m \end{pmatrix}$$

When $K_z = 0$ and $K_\theta = 0$, the above vectors are incomplete and the following vectors are used:

$$u_l^+ = \begin{pmatrix} 0 \\ h_l \\ 0 \end{pmatrix}, \qquad u_l^- = \begin{pmatrix} 0 \\ 0 \\ h_l \end{pmatrix} \tag{2.21}$$

$$\xi_m^+ = \begin{pmatrix} 0 \\ P_m \\ 0 \end{pmatrix}, \qquad \xi_m^- = \begin{pmatrix} 0 \\ 0 \\ P_m \end{pmatrix}$$

2.7 Quasi-Orthogonal Functions

The r-expansion functions g_l, h_l, Q_m and P_m consist of Chebyshev polynomials. The Chebyshev polynomials are efficient in resolving the boundary layers near the walls. Also, they are cosine functions after a coordinate transformation; thus the Fast Fourier Transform (FFT) can be used for computing the nonlinear terms. Pure orthogonal functions would give rise to diagonal matrices. At the same time, extra conditions on higher derivatives of these orthogonal functions are imposed, which leads to some

convergence problems. Therefore, quasi-orthogonal functions are used, yielding band-diagonal matrices and the solution converges rapidly. The quasi-orthogonal functions are constructed by taking linear combinations of Chebyshev functions, because the Chebyshev functions themselves do not satisfy any boundary conditions. These functions are given by:

$$\begin{aligned} g_l &= r(1-y^2)^2 T_l(y) \\ h_l &= r(1-y^2) T_l(y) \\ Q_m &= \frac{r^2}{(1-y^2)^{1/2}}\left(\frac{T_{m-2}}{4(m-1)m} - \frac{T_m}{2(m-1)(m+1)} + \frac{T_{m+2}}{4(m+1)m}\right) \\ P_m &= \frac{1}{2m(1-y^2)^{1/2}}(T_{m-1} - T_{m+1}) \end{aligned} \tag{2.22}$$

Here

$$y = \frac{2r - r_o - r_i}{r_o - r_i}$$

which makes $y = -1$ at $r = r_i$ and $y = +1$ at $r = r_o$. The set of coupled ODE's (2.19) is written as a single equation. The form of the resulting matrix is shown in Fig. 2.3. This is called a doubly-bordered band-diagonal matrix and can be inverted using any standard scheme (Press, Flannery, Teukolsky and Vetterling, 1992).

2.8 Nonlinear Terms

The nonlinear terms act as forcing terms to the implicit part of the calculation and are computed using the pseudospectral (collocation) technique. In the pseudospectral method, the inverse discrete Fourier transform is used to transform the Fourier-Chebyshev coefficients to physical space, perform a multiplication to compute the nonlinear terms (f and g), and then use the forward discrete Fourier transform to

compute $\hat{f}$ and $\hat{g}$.

It is required to solve Eqns. (2.2) and (2.3) with non-homogeneous boundary conditions. However, the expansion functions defined in Eqns. (2.15), (2.18), (2.20) and (2.21) only satisfy homogeneous boundary conditions. To make both the velocity and the temperature boundary conditions homogeneous, the laminar Couette flow velocity solution and the steady state conduction solution are subtracted from the actual velocity and temperature fields respectively such that:

$$V' = V - V_{CF} \tag{2.23}$$
$$T' = T - T_C$$

where V_{CF} and T_C are given by the analytical solution of the Navier-Stokes and the energy equations:

$$V_{CF} = \begin{pmatrix} 0 \\ -\frac{r_i}{r_o^2(1-\eta^2)} r + \frac{r_i}{(1-\eta^2)} \frac{1}{r} \\ 0 \end{pmatrix} \tag{2.24}$$
$$T_C = \frac{\ln \frac{r}{r_o}}{\ln \frac{r_i}{r_o}}$$

Now V' and T' satisfy the homogeneous boundary conditions. This change leads to incorporation of some additional terms in the nonlinear part, which can be performed without any difficulty. The treatment of the boundary conditions is given in Appendix A.

When the nonlinear terms are evaluated as described above, the method is not truly a spectral Galerkin method, but is called a 'pseudospectral method'. The advantage of this method is that the nonlinear terms can be evaluated faster. The disadvantage is that in the process of evaluating the nonlinear terms by this method,

a small error is introduced in the numerical solution. The error is called an 'aliasing error'. It is unknown how aliasing affects the real solution. Fully resolved numerical codes are not affected by aliasing errors. But codes with marginal resolution are most susceptible to the problem of aliasing. In all of the computations performed here, the nonlinear terms were computed on a grid large enough to eliminate aliasing by the $\frac{3}{2}$ rule (Canuto, et al., 1988).

2.9 Time-Advancement Scheme

The viscous and heat conduction terms are treated implicitly using the Crank-Nicholson scheme, whereas the convective terms are time-advanced explicitly using the second-order Adams-Bashforth scheme. The time discretized equations are :

$$\begin{aligned}\Big(\ddot{A} - \frac{\Delta t}{2R}\ddot{B}\Big)\alpha^{n+1} &= \Big(\ddot{A} + \frac{\Delta t}{2R}\ddot{B}\Big)\alpha^{n} + \frac{\Delta t}{2}\Big(3\dot{F}^{n} - \dot{F}^{n-1}\Big) \\ \Big(\ddot{C} - \frac{\Delta t}{2Pr\ R}\ddot{D}\Big)\gamma^{n+1} &= \Big(\ddot{C} + \frac{\Delta t}{2Pr\ R}\ddot{D}\Big)\gamma^{n} + \frac{\Delta t}{2}\Big(3\dot{G}^{n} - \dot{G}^{n-1}\Big)\end{aligned} \tag{2.25}$$

where $\ddot{A}$, $\ddot{B}$, $\ddot{C}$, $\ddot{D}$, $\dot{F}$ and $\dot{G}$ are defined in Eqn. 2.19. The ODE's are in the unknowns α's and γ's, which are the Fourier-Chebyshev coefficients. Once these coefficients are known, the entire velocity and the temperature field is determined.

The integrals in the matrices $\ddot{A}$, $\ddot{B}$, $\ddot{C}$ and $\ddot{D}$ in the above equations are numerically computed once, using Gauss-Chebyshev quadratures and are stored in the computer's memory to be used at every time-step. The matrices themselves are functions of the wave numbers K_z and K_θ. Therefore, to construct the matrices, the wave numbers are simply multiplied by the stored integrals. Storing the full matrices for the wave number pairs K_z and K_θ is memory extensive and is not done here. The vectors $\dot{F}$ and $\dot{G}$ are also numerically computed. In the above equations, Δt is the non-dimensional time-step. A time-step of 0.05 was used in all the computations, which yielded a

maximum Courant number of 0.75, where the Courant number C is defined as:

$$C = \pi \Delta t \left(\left| \frac{u_r}{\Delta r} \right| + \left| \frac{u_\theta}{r \Delta \theta} \right| + \left| \frac{u_z}{\Delta z} \right| \right) \tag{2.26}$$

2.10 Parallel Computing

The numerical code was written in Fortran and was initially implemented on the SGI Onyx computer. SGI Onyx is a scalar machine with an IP21 processor and a clockspeed of 75MHz. The simulations with 16 modes in all the three spatial directions (16^3) could be run quickly on this machine, but 32^3 calculations were taking much longer. To make the run time shorter for 32^3 calculations, a parallel version of the same code was also written in Fortran. The parallel code was implemented on the Paragon L38 supercomputer. It has a maximum of 512 compute nodes. Each node is an Intel i860XP microprocessor. The configuration is a 2D mesh of 16 rows and 36 columns. Memory per compute node on Paragon is 32MBytes with peak performance of each of its node being 75MFlops. Each i860XP is approximately two and a half times slower than an IP21.

The domain decomposition was done by breaking the 3D problem into a number of 2D problems. For example, a 32^3 simulation was decomposed into 32, 2D problems. In other words, 32 processors were used to run a 32^3 simulation. The benchmarks for the parallel speed-up are given in Tables 2.1 and 2.2. The tables show that the speed-up for 16^3 and 32^3 calculations are 2.5 times and 9 times respectively. The efficiency for a 32^3 simulation is approximately 70%. However, the efficiency for a 16^3 simulation is a mere 40%. The efficiency is defined as:

$$\text{efficiency} = \frac{1}{\text{number of parallel processors}} \left(\frac{t_s}{t_p} \times S_{rel} \right) \tag{2.27}$$

Here t_s and t_p are the time taken by the scalar and the parallel machines respectively. The relative speed of the scalar machine with respect to each parallel processor is given by S_{rel}. Subsequently, all the 16^3 simulations were performed on the scalar machine and 32^3 simulations were performed on the parallel supercomputer.

2.11 Code Validation

Code validation was achieved by computing several states of isothermal and heated Taylor-Couette flows. These states were then compared with a large body of existing theoretical, experimental and numerical literature on Taylor-Couette flows.

2.11.1 Isothermal Taylor-Couette flow

The first state to be computed was that of circular Couette flow. For η=0.9, the critical Reynolds number for the onset of Taylor vortices is 131.61 (DiPrima and Swinney, 1981). A Reynolds number lower than this value gives rise to pure Couette flow. An analytical solution for Couette flow exists, and shows a non-zero azimuthal velocity with a radial dependence. The axial and the radial velocities are identically zero. Shown in Fig. 2.4 is the analytical solution (solid line) and the numerical solution (symbol) for R=100 and L_z=2.007. The numerical solution agrees with the analytical solution for Couette flow.

The second flow state to be computed was that of Taylor-Couette flow. In Moser, et al. (1983), the tangential velocity as a function of r at the axial location where the radial velocity is zero is presented. Their result is plotted in Fig. 2.5 (solid line). The solid circles are the results from the present numerical calculations for R=400, η=0.833 and L_z=1.05. The calculations were performed using 32 Fourier modes in the z and θ directions and Chebyshev polynomials through 22^{nd} order in the r direction.

The resulting flow is axisymmetric and there is an excellent agreement between the calculated azimuthal velocities and the results of Moser, et al. (1983). Shown also in Figs. 2.6, 2.7 and 2.8 are the radial, tangential and axial velocity contours in the r-z plane. Plotted in Fig. 2.9 are the velocity vectors showing the familiar counter-rotating Taylor vortices. The adjacent Taylor vortices are of equal size.

A determination of the critical Reynolds number for the onset of Taylor vortices is performed for four different radius ratios. The axial wavelength selected is the wavelength corresponding to the minimum critical Reynolds number given by the linear stability analysis. To check for the critical Reynolds number, perturbations are introduced in the simulation. If the perturbations decay in time (with the flow eventually reaching a steady state) then the flow is stable. Otherwise the flow is unstable. The results are summarized in Table 2.3. The error margin in R for η=0.95 indicates that the disturbances died down for R=184 and grew into Taylor cells for R=186. A linear stability analysis (DiPrima and Swinney, 1981) shows that the critical Reynolds number for the onset of Taylor vortices for infinite aspect ratio concentric cylinders is approximately 185. Since the simulation run time required to reach a steady state is inversely proportional to (R-R_c), it becomes numerically difficult to simulate the flow with Reynolds number close to the critical Reynolds number. Hence the exact critical Reynolds numbers cannot be determined. Within the uncertainty of ± 1, the critical Reynolds numbers obtained from the numerical simulation agree well with the linear stability analysis.

Calculations of torque were also performed for two different radius ratios. The Reynolds numbers chosen for the wide gap (η=0.5) and the narrow gap (η=0.9) were 78.8 and 195 respectively. Torque per unit length, normalized by ρu_θ^2 is given by:

$$G = 2\pi r R\Big(\frac{d}{dr}(r\overline{u}_\theta) - 2\overline{u}_\theta\Big) \tag{2.28}$$

where $\overline{u}_\theta$ is the z-averaged tangential velocity. Experimental values for the torque are given by Donnelly and Simon (1960). The results are compared in Table 2.4. The results agree quantitatively within 3%. The reason for this discrepancy could be due to the fact that the axial wavelength was not measured in the experimental study. The torque has been shown to be sensitive to the axial wavelength (Meyer, 1967). In the simulations the axial wavelengths (L_z=1.988 for η=0.5 and L_z=2.009 for η=0.95) corresponding to the minimum critical Reynolds number was used. This assumption is appropriate considering the fact that the Reynolds number was slowly increased above the critical value.

The critical Reynolds number for the transition to non-axisymmetric Taylor-Couette flow was also calculated for η=0.875, L_z=2.007 and m=1 (one wave in the azimuthal direction). The flow was computed with 32 Fourier modes in the z and θ directions and with Chebyshev polynomials through the 32^{nd} order. The base flow was taken to be axisymmetric Taylor vortex flow, and then the perturbations were added in the θ direction. The perturbations grew into Wavy Vortex Flow (WVF) for R=131 and settled back to axisymmetric Taylor Vortex Flow (TVF) for R=129. Thus the critical Reynolds number computed for this flow is 130$\pm$1 which is close to the value of 131 reported by Jones (1981). The Reynolds number was slowly increased to 142 and m=2 wavy vortices were formed. The wave speed corresponding to this flow was computed to be 0.454$\pm$0.001. The error margin in this case is based on the time step. The wave speed also agrees well with the value of 0.455 reported by Jones (1981).

For a slightly higher Reynolds number, Fig. 2.10 shows the radial velocity contour in the z-θ plane, midway between the inner and the outer cylinders. The flow is for R=150 , L_z=2.007 and η=0.9 . Three azimuthal traveling waves (m=3) are seen in the figure.

2.11.2 Radially heated Taylor-Couette flow

The first radially heated flow state to be validated was the solution of the axial velocity as a function of r. The axial velocity given by Choi and Korpela (1980) is:

$$
\begin{aligned}
u_z(r) \;=\; & \frac{Gr}{16(1-\eta)^2 R}\left[\left(\frac{(1-\eta^2)(1-3\eta^2)-4\eta^4\ln\eta}{(1-\eta^2)^2+(1-\eta^4)\ln\eta}\right)\right. \\
& \left(\left((1-\eta)^2 r^2 - 1 + (1-\eta^2)\frac{\ln[(1-\eta)r]}{\ln\eta}\right)\right. \\
& \left.\left. -4[r^2(1-\eta)^2-\eta^2]\frac{\ln[(1-\eta)r]}{\ln\eta}\right]\right. \qquad (2.29)
\end{aligned}
$$

where R is the Reynolds number, Gr is the Grashof number and η is the radius ratio. The cases for a heated inner cylinder (Gr=2000) and a heated outer cylinder (Gr=-2000) for R=50, η=0.9 and L_z=2.007 are shown in Fig. 2.11. The solid line is the analytical solution given by Eqn. (2.29) and the symbols are the simulation results. The analytical solution is predicted well by the numerical code for both the Grashof numbers. Figs. 2.12 and 2.13 also show the axial velocity vectors for the above cases in the r-z plane. For Gr=2000, the buoyancy induces an upward flow near the inner cylinder wall and a downward flow near the outer one. The direction of flow reverses for Gr=-2000.

The accuracy of the code was also checked by comparisons with linear stability analysis (Chen, et al., 1990) for η=0.9, L_z=2.007 and Pr=0.71. The results are summarized in Tables 2.5 and 2.6. Table 2.5 refers to constant density simulations ($\beta^* = 0$) and Table 2.6 refers to simulations where the density depends on temperature. The critical Reynolds number (R_c) for the onset of Taylor cells and the computed wave speed (c) agree very well with the linear stability theory.

Machine	Time per step for a 16^3 simulation
Scalar	$1.0s$
Parallel (16 processors)	$0.4s$

Table 2.1: Benchmark for 16^3 parallel speed-up

Machine	Time per step for a 32^3 simulation
Scalar	$13.5s$
Parallel (32 processors)	$1.50s$

Table 2.2: Benchmark for 32^3 parallel speed-up

		Critical Reynolds number	
Radius ratio (η)	Axial wavelength (L_z)	Present simulation	Stability analysis
0.95	2.009	185±1	184.99
0.70	2.001	80±1	79.49
0.60	1.994	72±1	71.72
0.50	1.988	68±1	68.19

Table 2.3: Critical Reynolds number for the onset of Taylor vortices.

		Torque	
Radius ratio (η)	Reynolds number (R)	Present simulation	Experimental
0.95	195	5.418×10^5	5.258×10^5
0.50	78.8	1.486×10^3	1.478×10^3

Table 2.4: Torque calculations.

$\underline{Case\sharp}$ η=0.9 L_z=2.007 Pr=0.71	Stability Analysis of Chen and Kuo (1990)	Simulation
(1) Gr=200 β^*=0 R_c c	 132.39 0.00142	 132.4±0.2 0.00142±0.00001
(2) Gr=-200 β^*=0 R_c c	 132.39 −0.00142	 132.4±0.2 −0.00142±0.00001

Table 2.5: Comparison with linear stability theory for constant density.

$\underline{Case\sharp}$ η=0.9 L_z=2.007 Pr=0.71	Stability Analysis of Chen and Kuo (1990)	Simulation
(1) Gr=200 β^*=0.133 R_c c	 134.91 0.00130	 134.8±0.2 0.00131±0.00001
(2) Gr=-200 β^*=-0.138 R_c c	 129.96 −0.00153	 130.0±0.2 −0.00152±0.00001

Table 2.6: Comparison with linear stability theory for temperature dependent density.

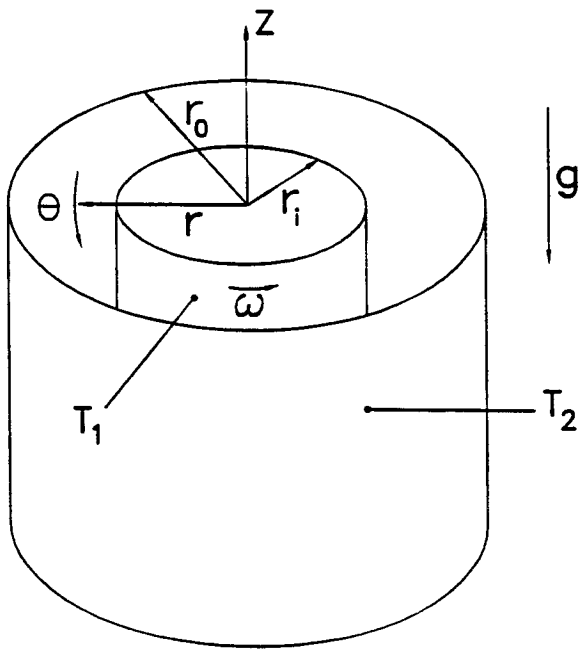

Figure 2.1: Flow geometry and boundary conditions.

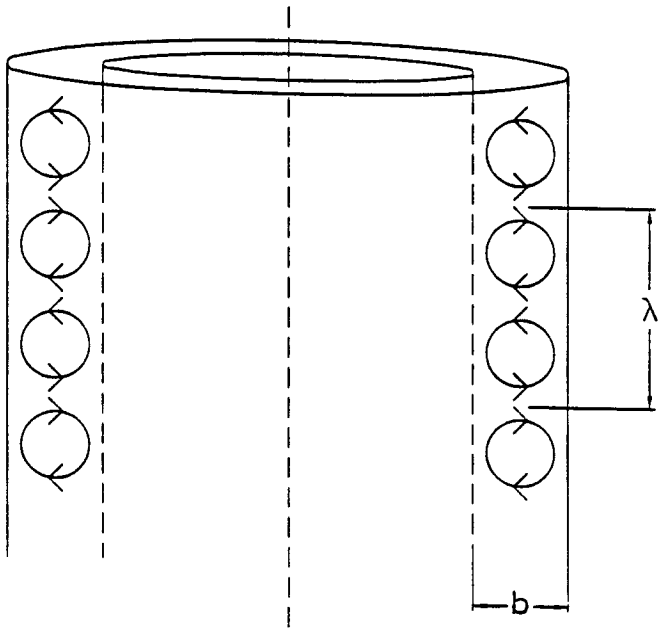

Figure 2.2: Schematic of isothermal Taylor cells.

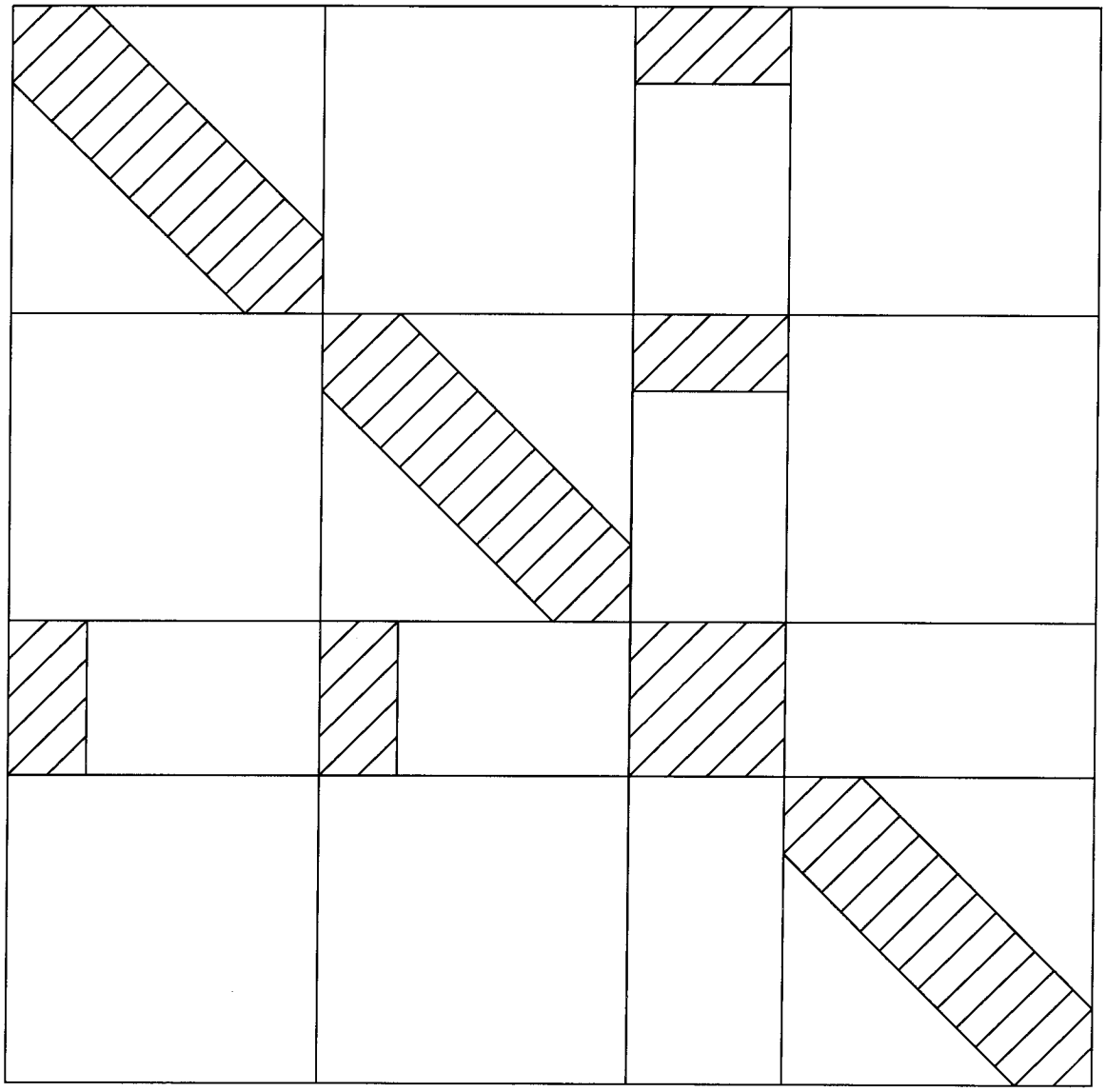

Figure 2.3: Matrix structure.

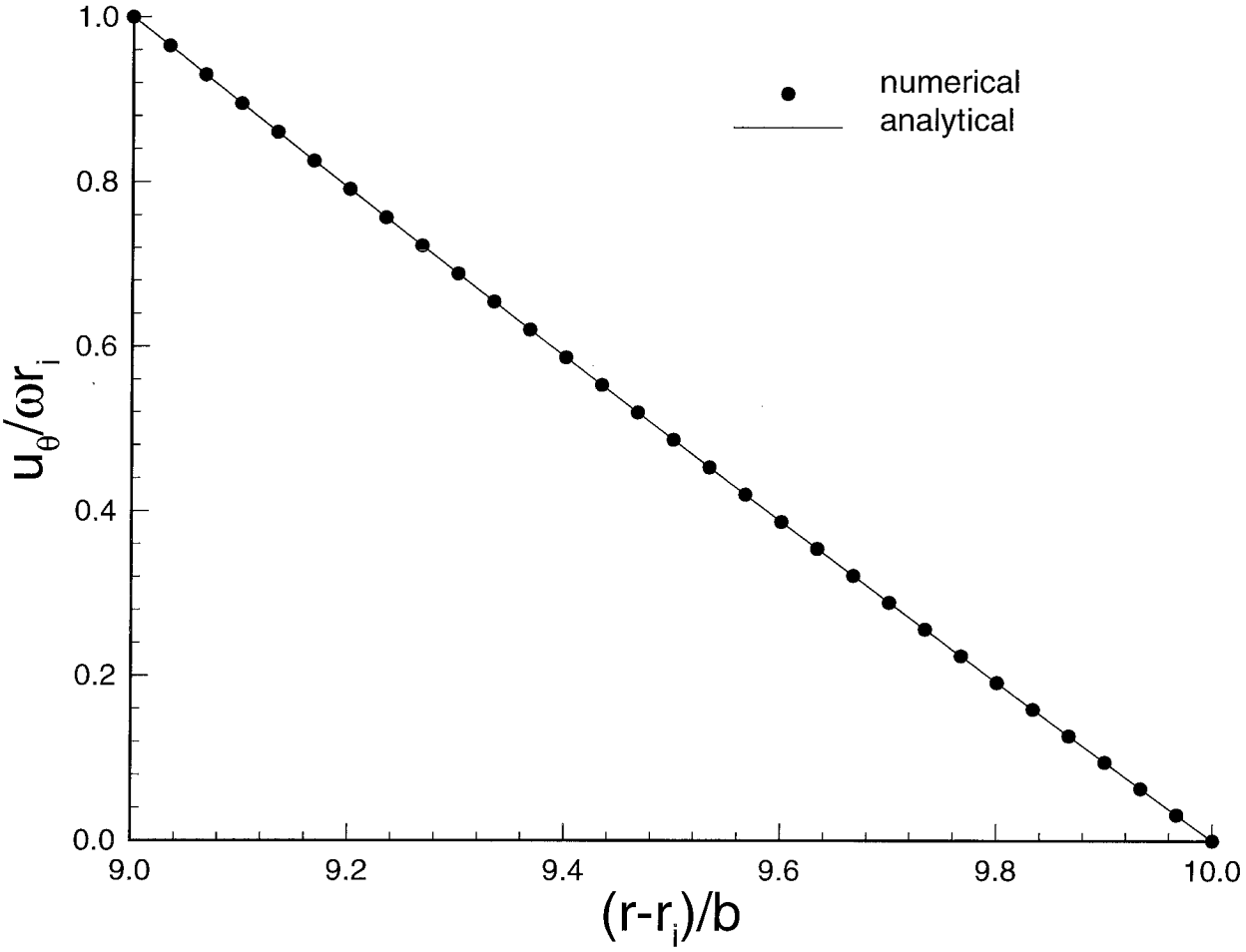

Figure 2.4: Analytical and numerical tangential velocity profile for circular Couette flow.

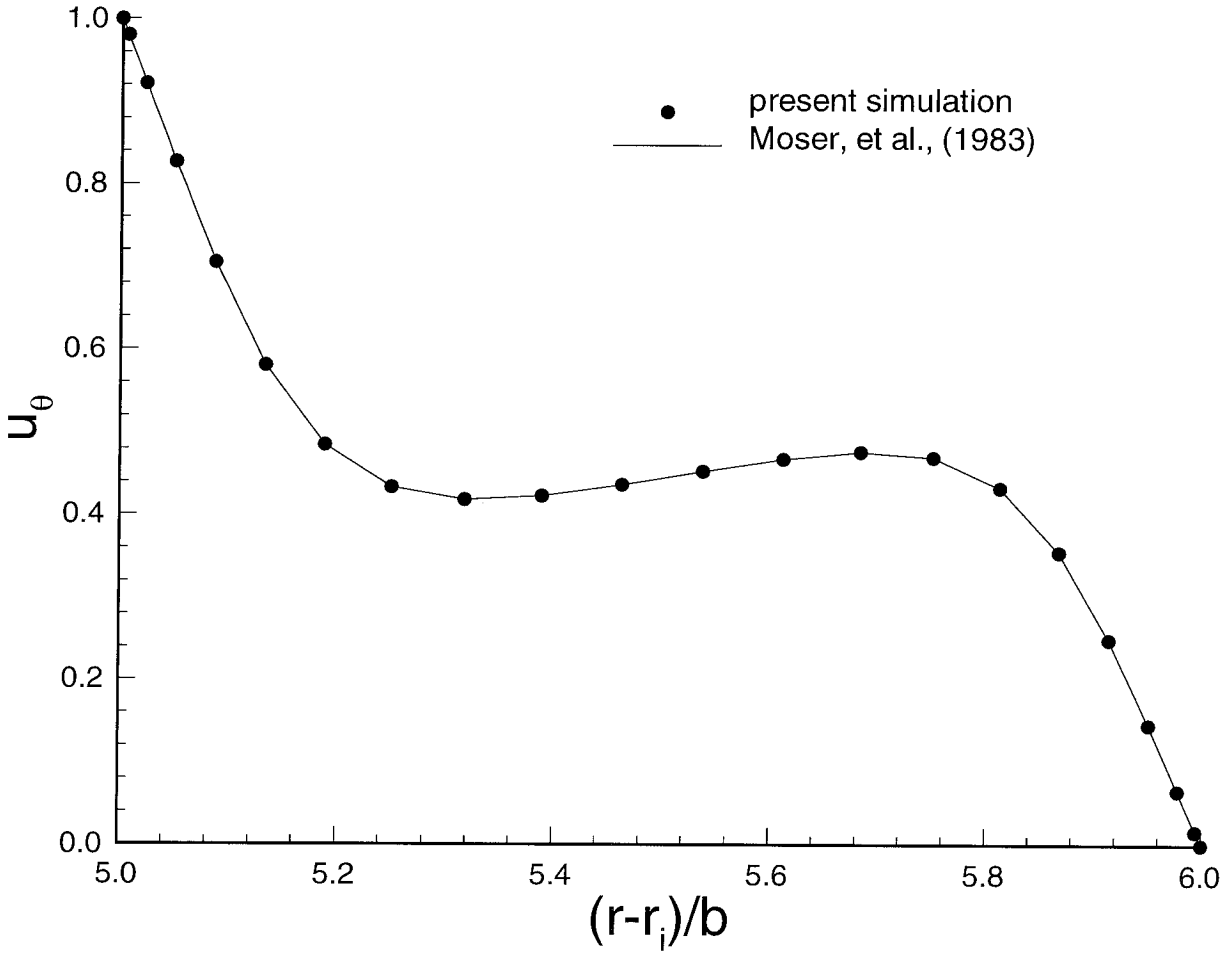

Figure 2.5: Tangential velocity for R=400, η=0.833 and L_z=1.05 at the axial location with zero radial velocity.

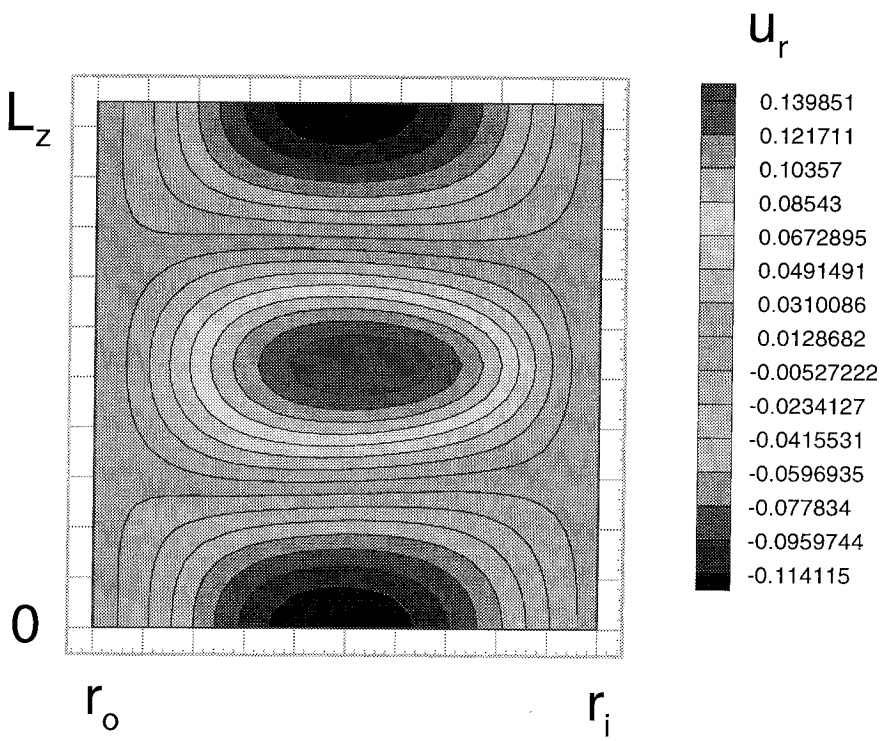

Figure 2.6: Radial velocity contours for R=400, η=0.833 and L_z=1.05 in the r-z plane.

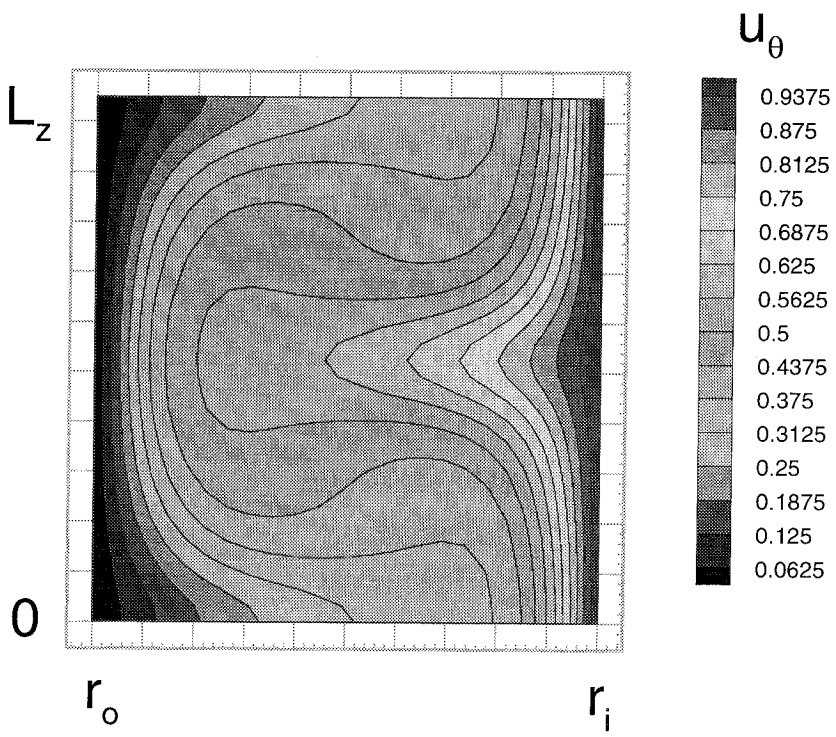

Figure 2.7: Tangential velocity contours for R=400, η=0.833 and L_z=1.05 in the r-z plane.

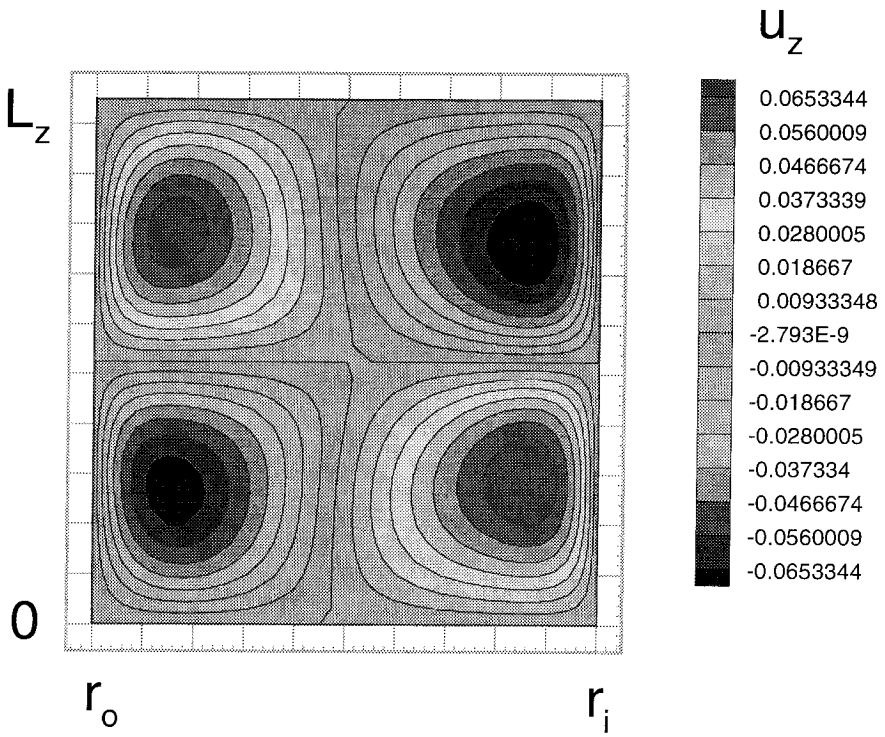

Figure 2.8: Axial velocity contours for R=400, η=0.833 and L_z=1.05 in the r-z plane.

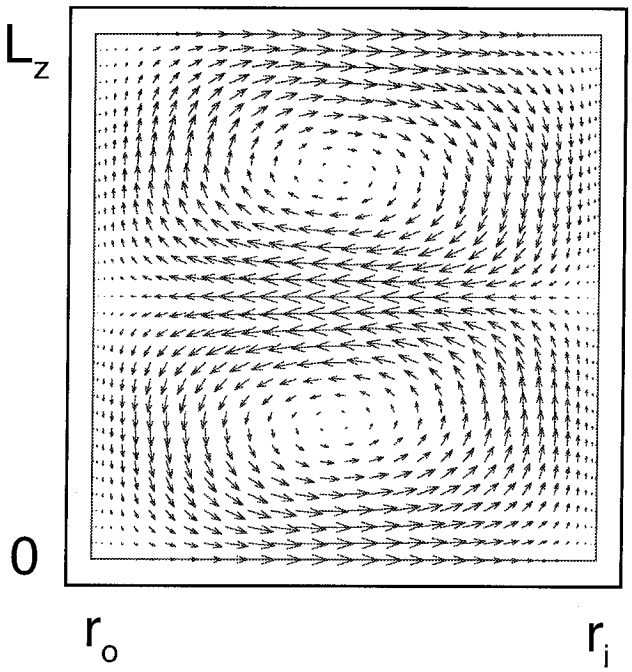

Figure 2.9: Velocity vectors for R=400, η=0.833 and L_z=1.05 in the r-z plane.

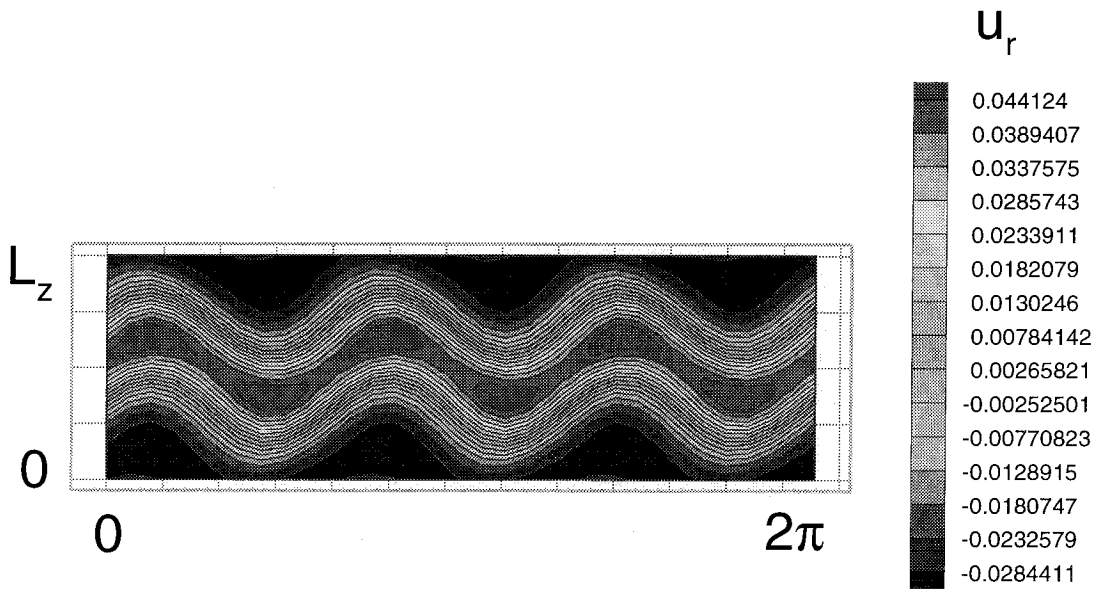

Figure 2.10: Radial velocity contours for R=150, η=0.9 and L_z=2.007 in the z-θ plane.

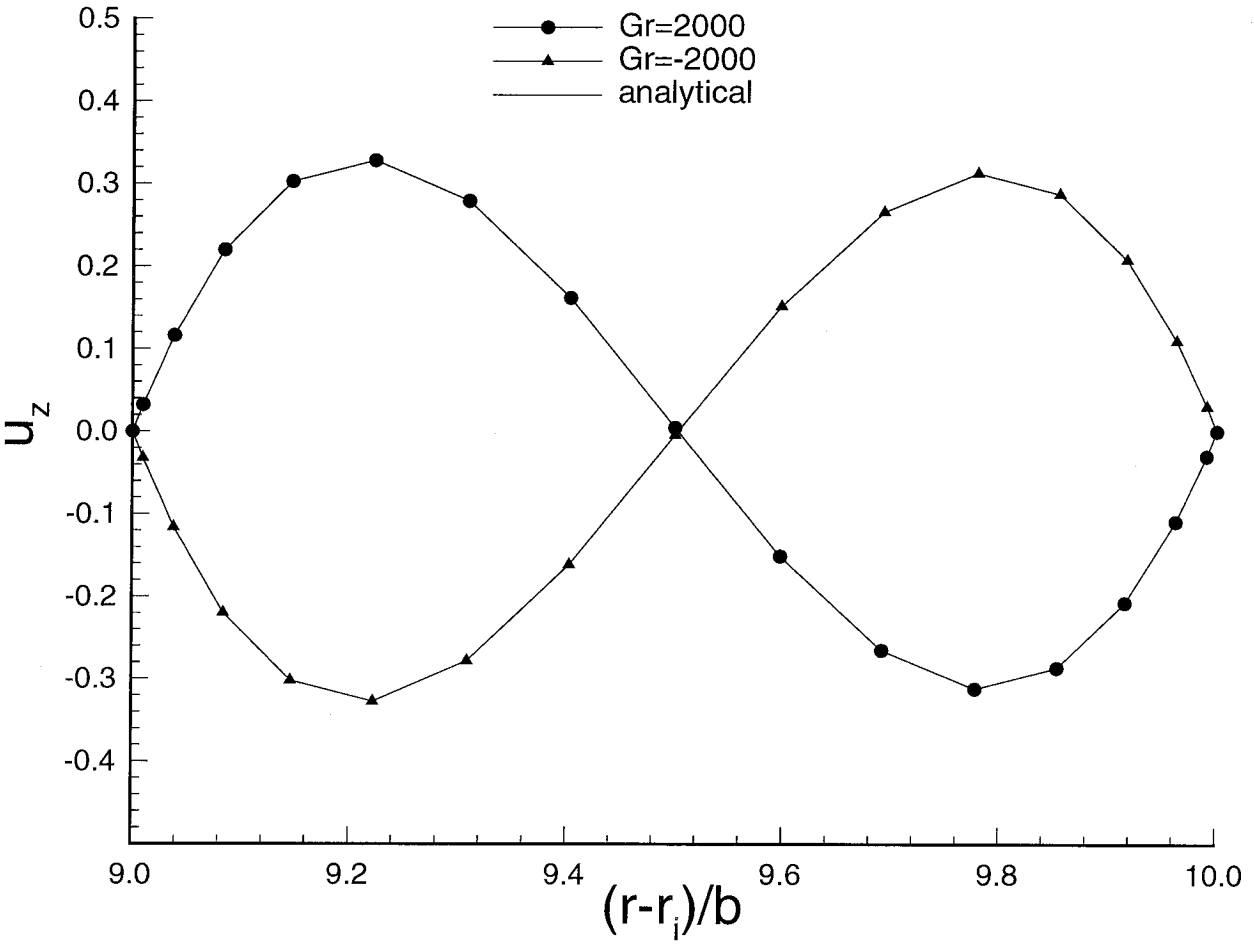

Figure 2.11: Axial velocity as a function of r for R=50, η=0.9 and L_z=2.007 for Gr=2000 and Gr=-2000. The solid lines are the analytical solutions and the symbols are the present simulation results.

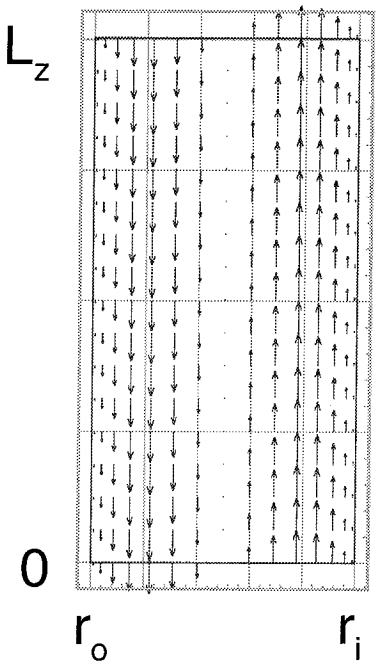

Figure 2.12: Velocity vectors for R=50, η=0.9, L_z=2.007 and Gr=2000 in the r-z plane.

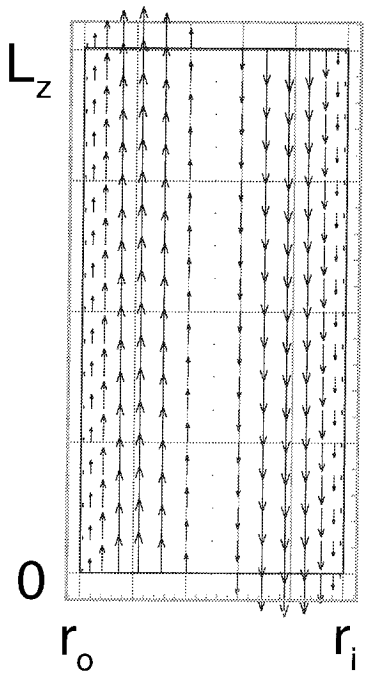

Figure 2.13: Velocity vectors for R=50, η=0.9, L_z=2.007 and Gr=-2000 in the r-z plane.

Chapter 3

Methodology II: Time Delay Method and the Experiment

3.1 Introduction

Typically, a time series would be measured at a single spatial point from an experiment and Fourier analysis would be performed to obtain information on the frequency content of the signal. If the power spectra is broad-banded, then it is possible that the source of the signal is a low dimensional dynamical system. Chaotic time series data are observed routinely in experiments on fluid flow and other physical systems. There are methods in nonlinear time series analysis to extract information from time series measurements. One such method of using time delay coordinates to reconstruct the entire phase space of an observed dynamical system was introduced by Takens (1981). The aim of the experimental part of this thesis is to use the time delay method and to verify whether a chaotic regime is encountered before the Taylor-Couette flow becomes fully turbulent at very high rotation rates of the inner cylinder.

The measured signal is usually contaminated by two different sources. The first

source is the perturbations from the environment and the second source is the data acquisition system. This undesirable contamination is often referred to as 'noise'. The source of the signal could be a linear or a nonlinear dynamical system. The power spectrum of a signal from a linear system has distinct spectral peaks with some broad-band noise. Once the signal of interest is identified, Fourier space is the natural domain to separate it from the noise. This is possible because the signal and the noise reside in different frequency ranges of the power spectrum. On the other hand, the power spectrum of a signal from a chaotic dynamical system is broad-banded. The measured signal contains both the signal of interest and the contamination. Fourier analysis is of little help in separating the two. Usually, though, the noise from the data acquisition system is of high frequency and some kind of low pass filtering is still reasonable and routinely done, as long as one bears in mind the implications of it.

3.1.1 How to reconstruct the attractor ?

To embed the attractor in m-dimensional space, m independent measurements need to be made from a dynamical system. Experimentally it is difficult to measure more than a few signals. Usually a single point measurement of a variable is obtained as a time series. It is possible to reconstruct the entire phase space of a dynamical system from this single point measurement because of the "embedding theorem" of Takens (1981). The theorem states that m-dimensional vectors, $\chi(t,\ \tau)$, can be constructed from the time series, $v(t)$, by choosing a suitable time delay, τ.

The vectors:

$$\chi(t,\ \tau) = [\ v(t),\ v(t+\tau),\ v(t+2\tau) \ldots\ldots v(t+(m-1)\tau)\ ] \tag{3.1}$$

are some unknown nonlinear transformation of the actual variable of the physical sys-

tem. It is not important to know this nonlinear transformation between the physical variable and the signal for the purpose of constructing the phase space. Any smooth nonlinear change of variable will act as a coordinate basis for the dynamics of the system. For m large enough, the attractor dimension will be the same as the dimension of the reconstructed attractor. The embedding theorem (Takens, 1981) states that if the embedding dimension, m, is one more than twice the attractor dimension, then the attractor will certainly be unfolded. This condition is not necessary for unfolding but is sufficient and indicates that the maximum number of components in the time delay vector should be m. In the process of calculating the dimension of an attractor, the embedding dimension is increased in steps until the attractor dimension attains a constant value. Methods of calculating the optimal embedding dimension are also given by Buzug, et al. (1992).

3.1.2 Time delay

The embedding theorem of Takens states that any time delay would work for the construction of m-dimensional vectors. This is true theoretically for a data set which is free of any contamination. But experimentally this is not the case. If τ is too small, then the vectors would be very close to each other and it would be very hard to distinguish them due to the presence of noise. If τ is too large, then $v(t)$ and $v(t+\tau)$ would be statistically independent. This is because the motion on the attractor is ergodic and the projection of an orbit on the attractor onto the two directions would be more or less random.

One way to determine the time delay is to compute the auto-correlation function:

$$C(\tau) = \int v(t)v(t+\tau)dt \tag{3.2}$$

and choose the value of τ for which the auto-correlation function becomes zero. The zero of the auto-correlation function indicates the time lag at which $v(t)$ and $v(t+\tau)$ become linearly independent. However, a chaotic time series arises from a dynamical system which is inherently nonlinear. Therefore a more general independence of the coordinates is required. The mutual information function, $I(\tau)$, is an entropy based concept and is derived from Information theory. It is defined as:

$$I(\tau) = \int\int P(X,Y)\log_2[P(X,Y)/P(X)P(Y)]dXdY \tag{3.3}$$

where $X = v(t)$ and $Y = v(t+\tau)$. $P(X)$ and $P(X,Y)$ are the probability density and the joint probability density. Given the value of $v(t)$, the mutual information function gives the accuracy with which $v(t+\tau)$ can be predicted. Since $v(t)$ and $v(t+\tau)$ denote the coordinates of the reconstructed phase space, they should be independent of each other. Therefore, the time delay corresponding to the first local minimum (Fraser and Swinney, 1986) of the mutual information function is a good choice. A new method for the estimation of the mutual information to experimental time series from different locations in the flow is also given by Buzug, et al. (1994).

3.1.3 Dimension calculations

The attractor dimension is one of the most important invariants of a dynamical system. The dimension is roughly the number of independent variables needed to model the underlying phenomenon in a dynamical system. Investigations by Brandstater, et al. (1987) have shown that the flow undergoes a series of transitions before it becomes fully turbulent. They encountered a "weakly turbulent", low-dimensional chaotic attractor as the inner cylinder Reynolds number was increased. The subject of investigation in the experimental part of this thesis is whether such a low dimen-

sional strange attractor exists in the flow and, if so, what happens to its dimension as the inner cylinder speed is increased.

There are many different kinds of dimension, such as the fractal dimension, the pointwise dimension and the correlation dimension (Farmer, et al., 1983). They can all be derived from the definition of generalized dimensions:

$$D_q = \lim_{\epsilon \to 0} \frac{1}{q-1} \frac{\log \sum_i P_i^q}{\log \epsilon} \tag{3.4}$$

where P_i is the probability of finding a point in the i^{th} box of size ϵ. For the limit as q approaches 0 the fractal dimension results. For the limit as q approaches 1 the pointwise dimension or the dimension of the natural measure is obtained. It is also defined as:

$$D_1 = \lim_{\epsilon \to 0} \frac{< \log N(\epsilon) >_x}{\log \epsilon} \tag{3.5}$$

where $N(\epsilon)$ is the number of points in a ball of radius ϵ. The averaging is done over different referencing points x. For the limit as q approaches 2 the correlation dimension is obtained. It is similar to the pointwise dimension but the averaging is done over the number of points $N(\epsilon)$.

$$D_2 = \lim_{\epsilon \to 0} \frac{\log < N(\epsilon) >_x}{\log \epsilon} \tag{3.6}$$

D_∞ is the lower bound for the dimensions and $D_0 > D_1 > D_2$. As an empirical rule, for an m-dimensional embedding, 2^{m+2} reference points are used, so that the reference points fill up the phase space equally densely.

Fractal dimensions were also calculated by Pfister, et al. (1992) and Buzug, et al. (1992) in a Taylor-Couette experiment. They measured the axial velocity component

of the flow field with Laser-Doppler velocimetry and the phase space was reconstructed by using delay time coordinates. Silicon oil was used as the working fluid. Their system showed all the three well-known routes to chaos: the period doubling cascade, intermittency and the break-up of a torus.

3.1.4 Modeling

The information about the phase space, such as the temporal evolution of the trajectories and the dimension of the attractor, can be used for making models such as predicting the value of the heat transfer coefficient for aperiodic flow. These models can then be used for predicting future behavior of the dynamical system, i.e., extracting the value of $v(t+1)$ given a long time series of $v(t)$. The simplest nonlinear method of local forecasting would be to find the nearest neighbor of $v(t)$, say, $v(p)$, and then predict $v(p+1)$ as the future value for $v(t+1)$. An improvement on this would be to take a collection of near neighbors of the point $v(t)$ and make the averaged value of their images the prediction.

One way of making models is that of local neighborhood to neighborhood maps (Abarbanel, 1996). It is assumed that a local functional form exists for the evolution of the dynamics $x \rightarrow F^{(t)}(x)$ in the neighborhood of the point $v(t)$:

$$F^{(t)}(x) = \sum_{j=1}^{M} a(j,t)\Phi_j(x) \tag{3.7}$$

The functions $\Phi_j(x)$ are a basis set and can be polynomials. The number of basis functions chosen is M. The model is made in the d-dimensional subspace of the embedding m-dimensional space. Hence, $v(t)$ is a d-dimensional vector. The action

of the map $F^{(t)}(x)$ on $v(t)$ gives $v(t+1)$ such that:

$$\begin{aligned} v(t+1) &= F^{(t)}(v(t)) && (3.8) \\ &= \sum_{j=1}^{M} a(j,t)\Phi_j(v(t)) && (3.9) \end{aligned}$$

The coefficients of the model can be determined by minimizing

$$\sum_{i=1}^{N} \left| v(i,t+1) - \sum_{j=1}^{M} a(j,t)\Phi_j(v^{(i)}(t)) \right|^2 \qquad (3.10)$$

over N nearest neighbors of the point $v(t)$, given by $v^{(i)}(t)$; i=1,2,....N. Solving this linear problem gives the coefficients $a(j,t)$ for each observed point $v(t)$ on the attractor. Now, given a point $z(0)$ to predict the evolution of the system, one would search the $v(t)$ to find a point nearest to $z(0)$. Call this $v(p)$. Then the local map $F_p(x)$ is constructed from its N nearest neighbors and $F_p(z(0))$ gives the next point $z(1)$ on the trajectory of the attractor. The process could be iterated far into the future for prediction.

3.2 Time Delay Method Validation

To see how well the time delay method works, it is applied to a model system. The celebrated Lorenz equations are chosen for this purpose. The equations:

$$\begin{aligned} \dot{x} &= \sigma(y-x) \\ \dot{y} &= -y - xz + rx \qquad (3.11) \\ \dot{z} &= xy - bz \end{aligned}$$

exhibit chaos for σ=10, r=28 and b=$\frac{8}{3}$. These equations are solved using a fourth order Runge-Kutta method. The initial conditions are $x(0)$=20, $y(0)$=0 and $z(0)$=10, with a time step of 0.01. Shown in Fig. 3.1 is the projection of the trajectory on the x-z plane. Now only the x-values are kept and, y and z values are discarded. It remains to be seen whether the phase space of the original Lorenz attractor can be reconstructed and the dimension correctly calculated using only the x-values obtained from integration of the Lorenz equations. Before the phase space is plotted, a suitable time delay must be chosen. The mutual information function of the x-values is plotted in Fig. 3.2. As discussed previously, the first local minimum is an optimum choice for the time delay. Therefore, a delay of τ=0.17 (17 time steps) is chosen for the time delay coordinates. Figure 3.3 shows the value of $x(t+\tau)$ plotted against $x(t)$. The celebrated butterfly pattern is again obtained, with remarkable similarity in the structure with Fig. 3.1. If the delay time is too small, for example 2 time steps, then the reconstructed phase plot shows a line at an angle of 45° (Fig. 3.4). In Fig. 3.5, the trajectory is plotted in phase space with a delay of 150 time steps. It is seen that the points on the attractor spread out, if the delay time is too large.

The Lorenz attractor has an estimated fractal dimension of 2.06. From the reconstructed phase space with a delay of 17 time steps, the correlation dimension is calculated. The correlation dimension is based on the idea that the number of points $N(\epsilon)$ in a hyper-sphere of radius ϵ scales with the attractor dimension. Plotted in Fig. 3.6 is a graph of $\log N(\epsilon)$ versus $\log \epsilon$. A constant slope of approximately 2 (Fig. 3.7) is clearly visible, and reflects the fractal dimension of the attractor.

3.3 The Experiment

The details of the experimental setup and the data acquisition system are briefly discussed in the following two sections. A more detailed description is available in

Shih (1994).

3.3.1 Setup

The experimental setup consists of two concentric cylinders. The inner rotating cylinder has an O.D. of 20.96 cm and is made of aluminum. The stationary outer cylinder is made of plexiglass and has an I.D. of 23.50 cm. The inner cylinder is mounted to a hollow shaft which is driven by a Sabina 220 volt, 2 hp d.c. motor with a maximum rotation rate of 1750 RPM. The height of the annulus is 50.80 cm and the gap width is 1.27 cm. This results in an aspect ratio, h/b of 40, and a radius ratio, r_i/r_o of 0.89. The Reynolds number is defined as $R = \omega r_i b/\nu$ where r_i is the radius of the inner cylinder, ω is the angular velocity of the inner cylinder, b is the gap width and ν is the kinematic viscosity. The critical Reynolds number for the onset of Taylor vortices in a very large aspect ratio apparatus for a radius ratio of 0.89 is 125.67. The working fluid is air. The rotation speed of the inner cylinder is measured by an optical encoder. One revolution of the inner cylinder produces 1000 pulses from the encoder. These pulses are sampled at a frequency of 100kHz using one of the channels of the data acquisition system.

3.3.2 Data acquisition

The hot-wire data is collected using a personal computer. A Das-20 data acquisition board manufactured by MetraByte Corp., with a maximum sampling rate of 100kHz is used for this purpose. The board has a resolution of 12-bits and there are 16 single-ended input channels. The SSH-4 simultaneous sample and hold board is used for acquiring two time series at the same time. The SSH-4 board can sample up to a maximum of 4 channels with less than 40 nanoseconds of channel to channel sample time uncertainty. It was necessary to acquire data from two spatial locations

simultaneously for the purpose of performing cross correlations.

3.3.3 Time series measurement

Four 0.635cm diameter holes are drilled in the circumferential direction at the mid-height location for velocity measurements. A hot-wire anemometer manufactured by Dantec Electronic, Inc., is used to measure the velocity at a point midway in the gap between the inner and the outer cylinders. The 55P11 type hot wire measures both the radial and the azimuthal components of the velocity. The hot wire is placed on a probe stand and the probe holder can traverse in the radial direction with a high degree of precision. The hot-wire probe can measure velocity in the range of 0.15 m/s $\sim$ 500 m/s. But for the present experiment, it was calibrated in the range 0.15 m/s $\sim$ 3 m/s. It has a maximum frequency response of 100kHz. The output of the hot-wire is a voltage. If the actual velocity is desired, then it has to be converted using King's law. But for time delay analysis, the voltage signal itself was used because there is a smooth transformation between the voltage and the velocity.

3.4 Taylor-Couette Flow Validation

3.4.1 Couette flow

It is imperative to confirm that features of a Taylor-Couette flow found in the literature can be repeated in the experimental facility. A number of experiments were done to validate the experimental system, such as the existence of the Couette flow velocity profile. As the rotation of the inner cylinder is slowly increased, Taylor cells are formed at a particular Reynolds number. Any Reynolds number lower than the critical value should give rise to a featureless Couette flow. Figure 3.8 shows the analytical and the experimental tangential velocity profile at the mid-axial position

of the annulus for R=106.5. There is close agreement between the two values.

3.4.2 Taylor vortex flow

For the radius ratio, η=0.89, the critical Reynolds number for the onset of Taylor cells in an infinite system is approximately 125.67 (Edwards, et al., 1991). To find the critical Reynolds number in the experiment, the inner cylinder rotation speed is slowly increased in steps and air is blown axially in the annulus. The hot-wire signal is closely monitored. With the formation of the Taylor cells, sharp dominant peaks also start to appear on the hot-wire signal. These peaks are the result of toroidal Taylor vortices drifting past the hot-wire probe with the mean velocity of the axial flow. The vortices appear at the inner cylinder RPM of 14, which translates into a Reynolds number of 125±3. This value is close to the value of 125.67.

Similarly, the axial wavelength corresponding to the critical Reynolds number is also measured. The mean velocity of the air blown axially is known *a priori* from a previous calibration. The time lag between two peaks is obtained from the hot-wire velocity trace. Knowledge of the velocity and the time lag enables the determination of axial wavelength of a pair of Taylor vortices. The axial wavelength normalized by the gap width obtained in this fashion is found to be 2.006±0.004 which is very close to the theoretically obtained value of 2.007.

3.4.3 Wavy vortex flow

The next transition is to a wavy vortex flow regime where traveling waves are formed in the azimuthal direction. The critical Reynolds number for the onset of wavy vortex flow is determined by means of a cross-correlation technique. Two hot-wire probes are placed at an azimuthal angle of 90°. The signals from both the wires are simultaneously recorded using a SSH-4 data acquisition board. Before the waves are

formed, the signals are identical because the flow is axisymmetric and there is no axial blowing. With the formation of the azimuthal waves, a time lag is observed between the two signals. The formation of the azimuthal waves occurred at R/R_c=1.09±0.05. This value is very close to a numerical value of R/R_c=1.089 reported by Edwards, et al. (1991). At this Reynolds number, it is also determined that the number of azimuthal waves formed is 2. From the time lag and the distance between the two probes, the wave velocity can also be calculated. The wave velocity normalized by the velocity of the inner rotating cylinder is evaluated to be 0.495. As reported by Coles (1965), the angular velocity of the waves is close to half the angular velocity of the inner rotating cylinder. The value reported by Coles agrees with the value of 0.495 obtained in the present experiment.

3.4.4 Measurements of axial wavelengths

The axial wavelengths are determined as a function of the Reynolds number. The rotation of the inner cylinder is increased steadily. Since the experiment is designed to study very high Reynolds number flows, it is very difficult to increase the rotation very slowly. The highest RPM studied here for the wavelength measurements is 125. The process is called a 'steady acceleration' in the sense that the RPM of the inner cylinder is increased in steps of not more than 4. After every step increase of the inner cylinder speed, the system is given 15 minutes for relaxation. The measurements of the axial wavelength is then made from the hot-wire trace of the velocity time series. The wavelengths normalized by the gap width versus R/R_c are plotted in Fig. 3.9. Also plotted on the same graph are the measurements made by Koschmieder (1979) for a radius ratio of 0.896. Both the results show that the wavelengths increase with the increase of the Reynolds number. The present results agree quantitatively within 7% of those obtained by Koschmieder.

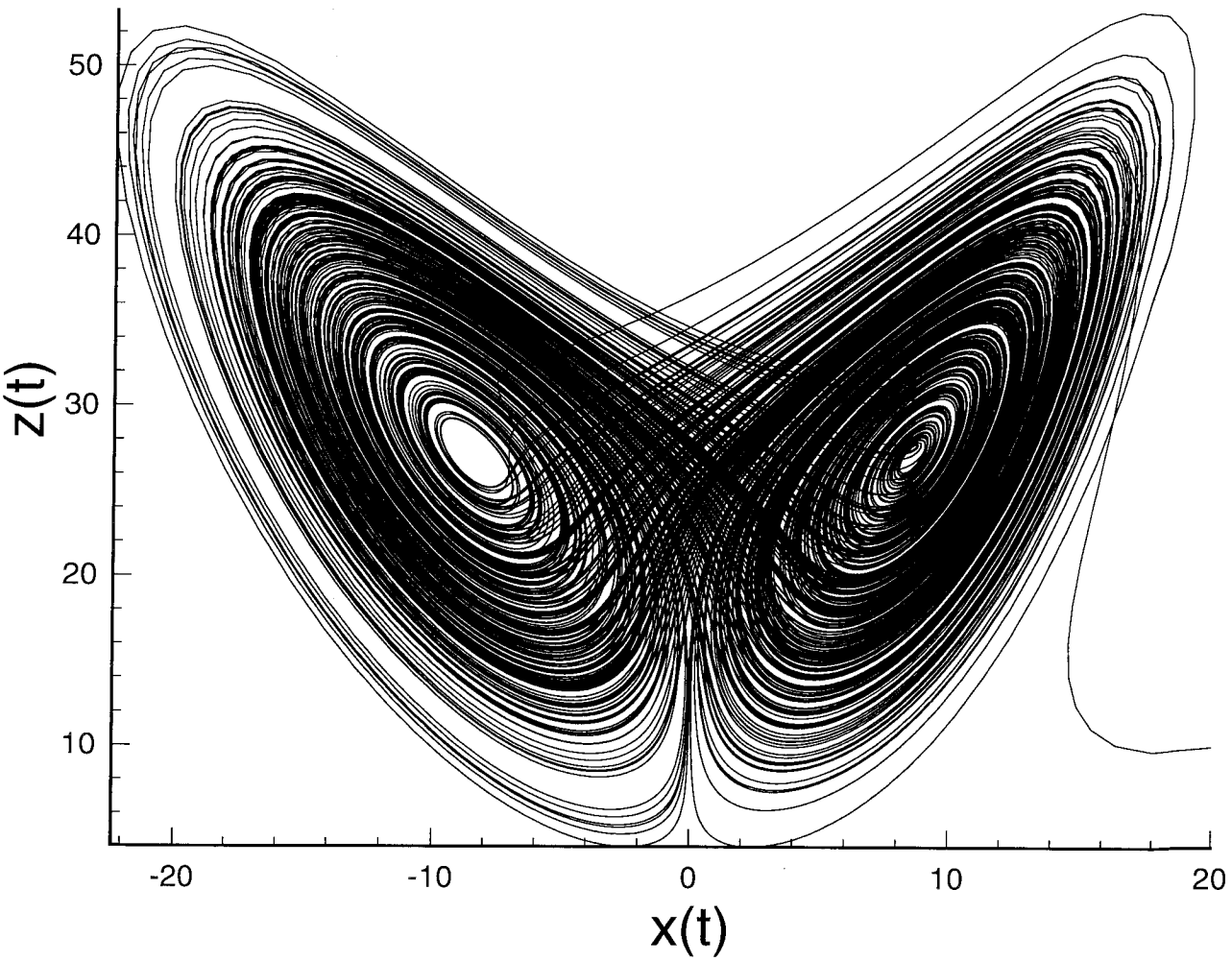

Figure 3.1: Projection of the Lorenz attractor on the x-z plane.

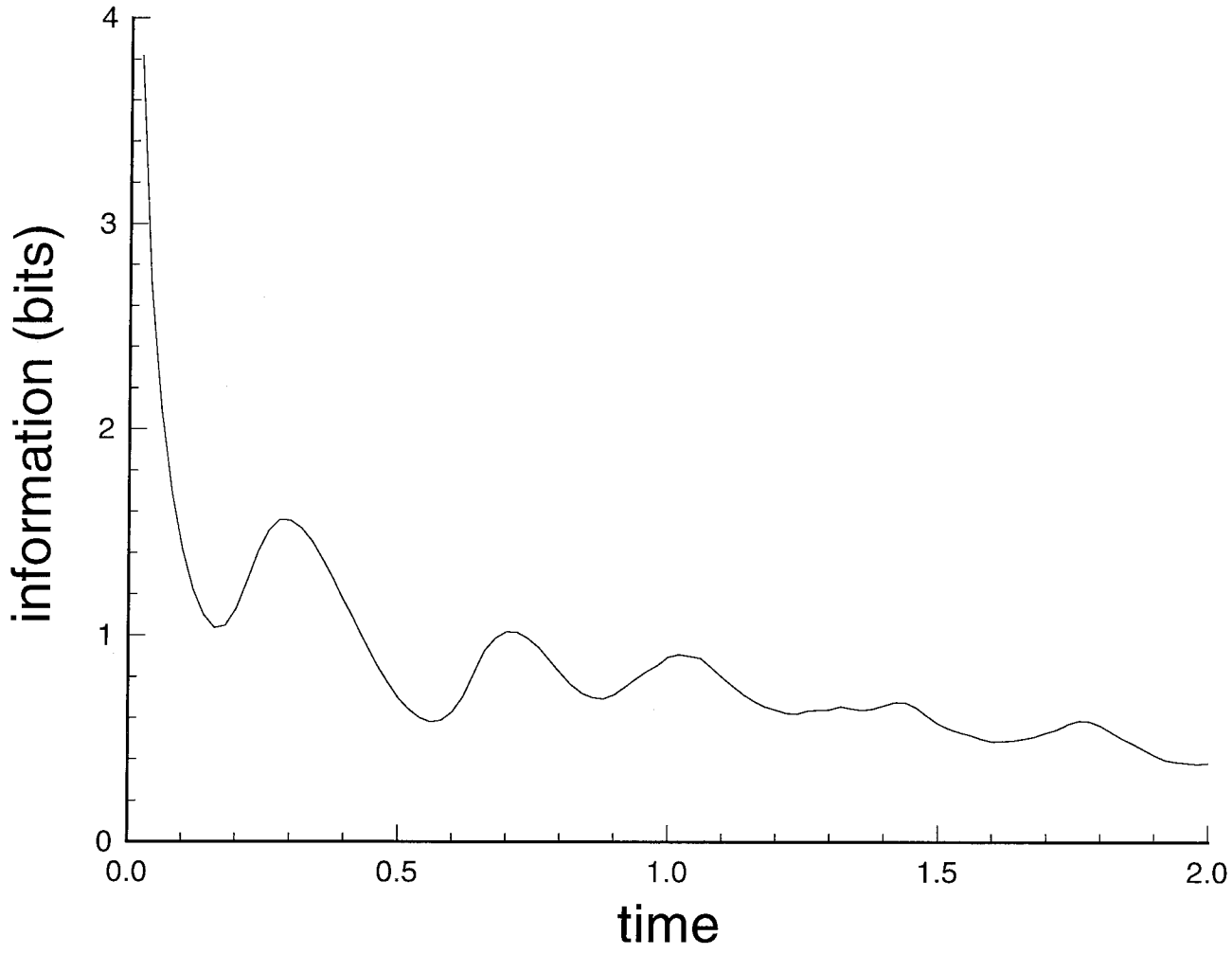

Figure 3.2: Mutual information for Lorenz equations using only the x-values.

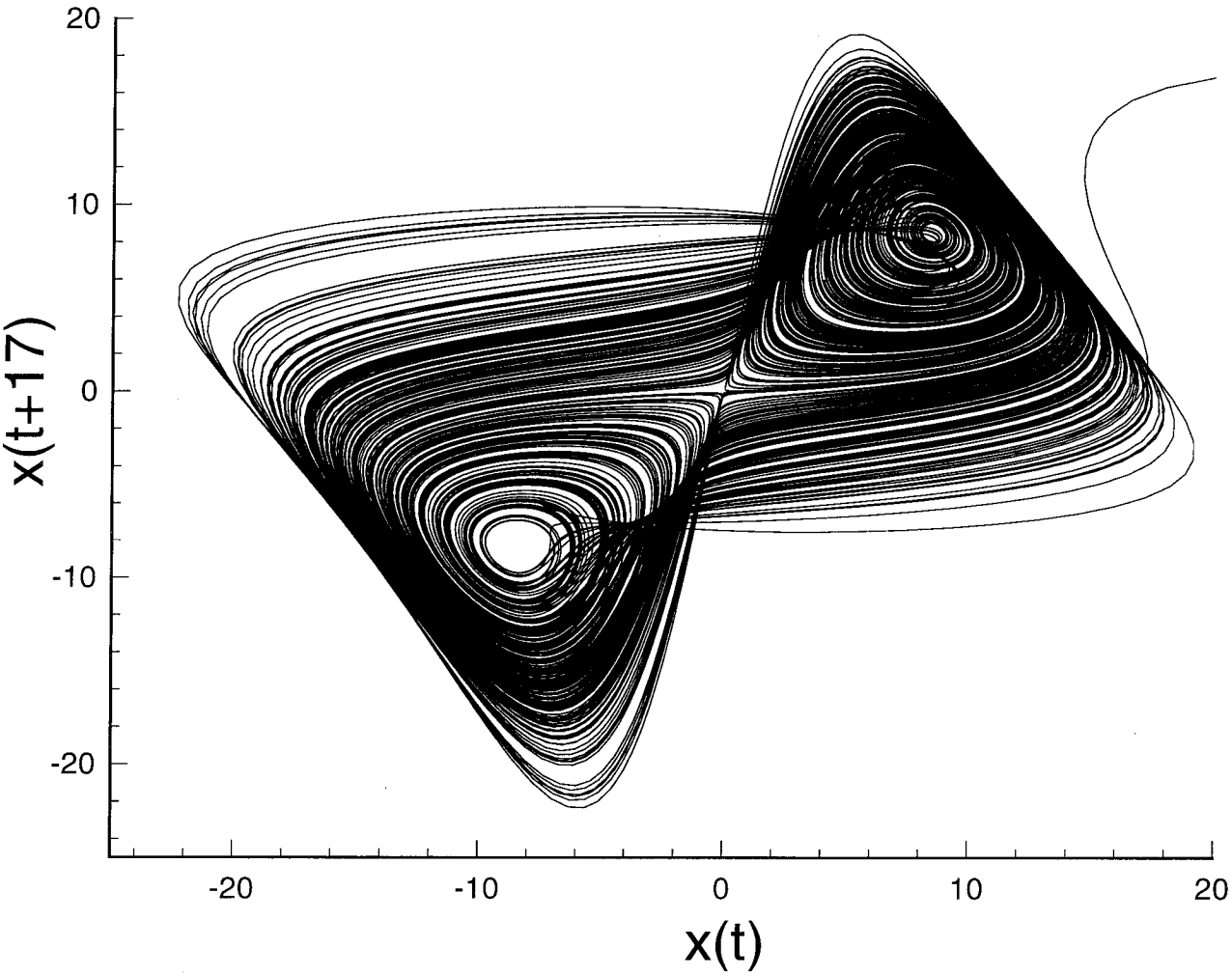

Figure 3.3: Reconstruction of the Lorenz attractor using a time delay of 17 time steps.

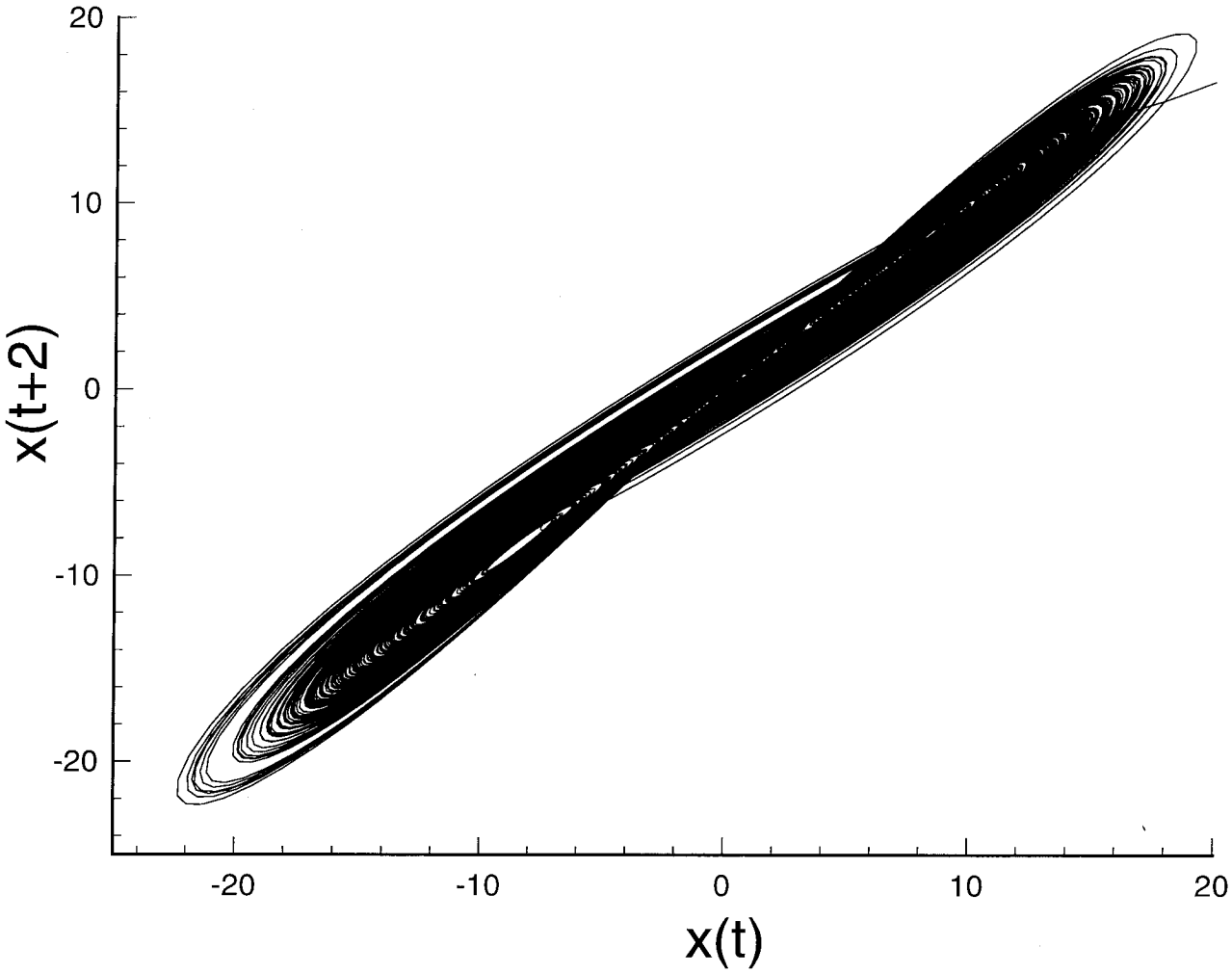

Figure 3.4: Reconstruction of the Lorenz attractor using a time delay of 2 time steps.

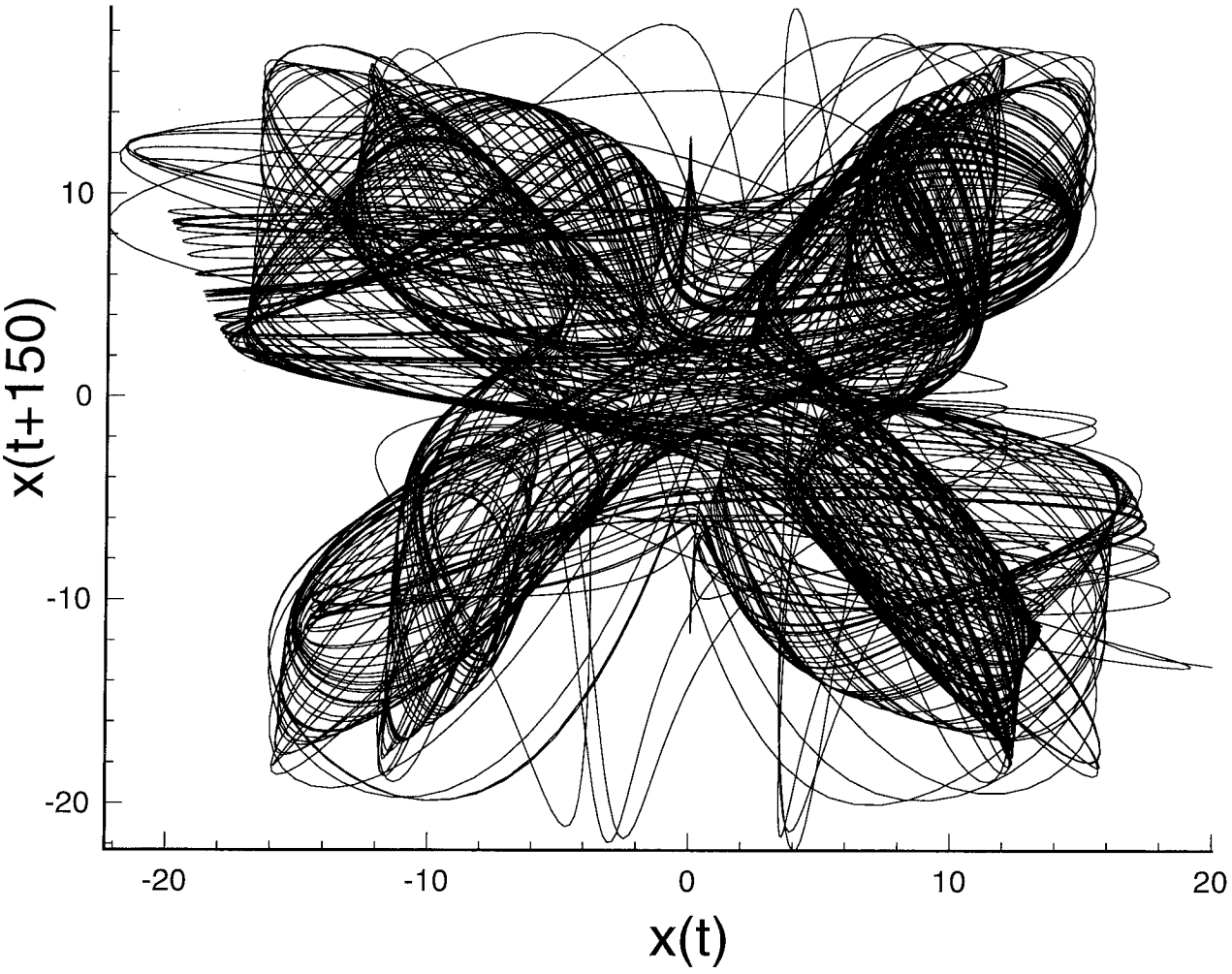

Figure 3.5: Reconstruction of the Lorenz attractor using a time delay of 150 time steps.

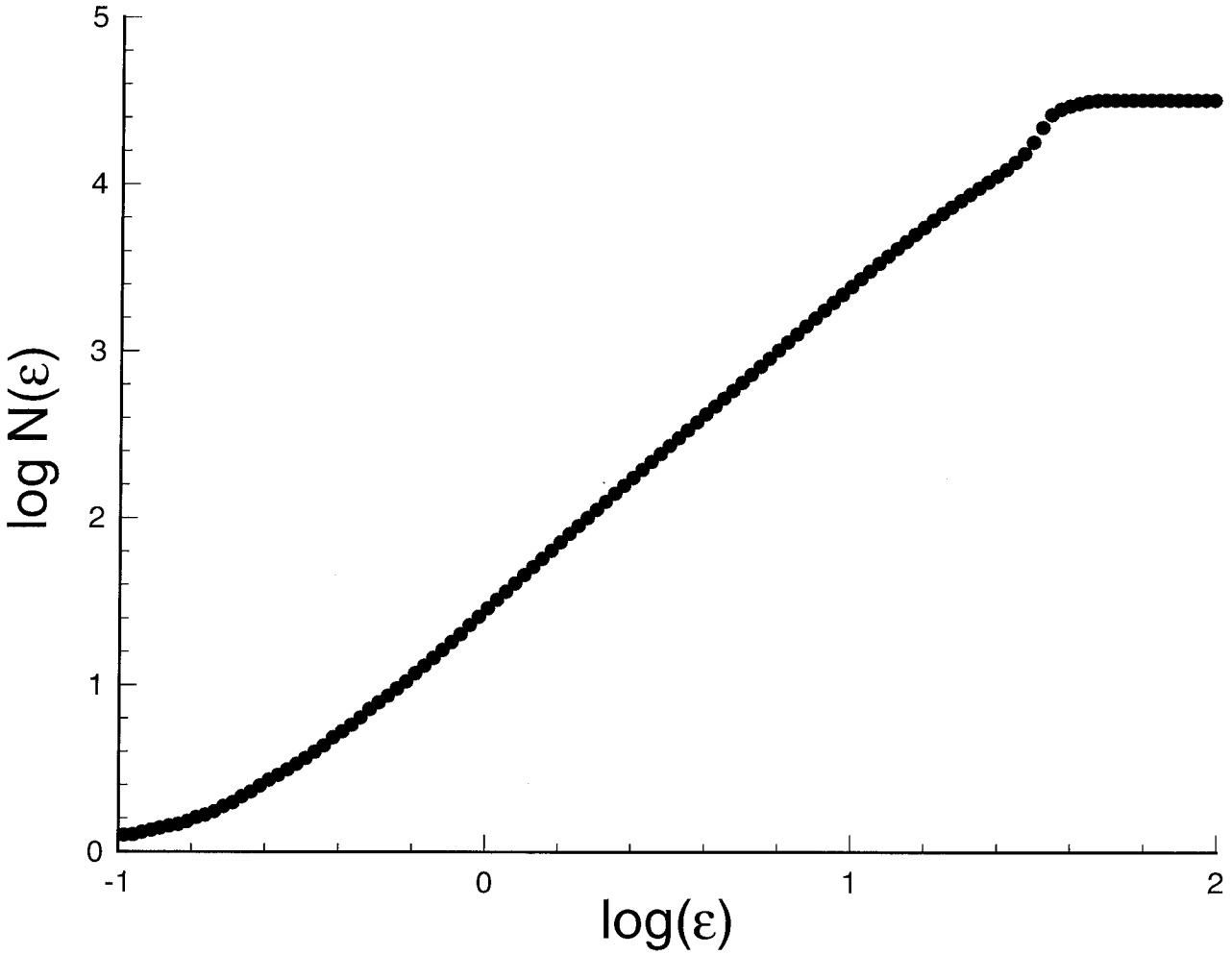

Figure 3.6: Plot of $\log N(\epsilon)$ versus $\log(\epsilon)$ for the Lorenz attractor

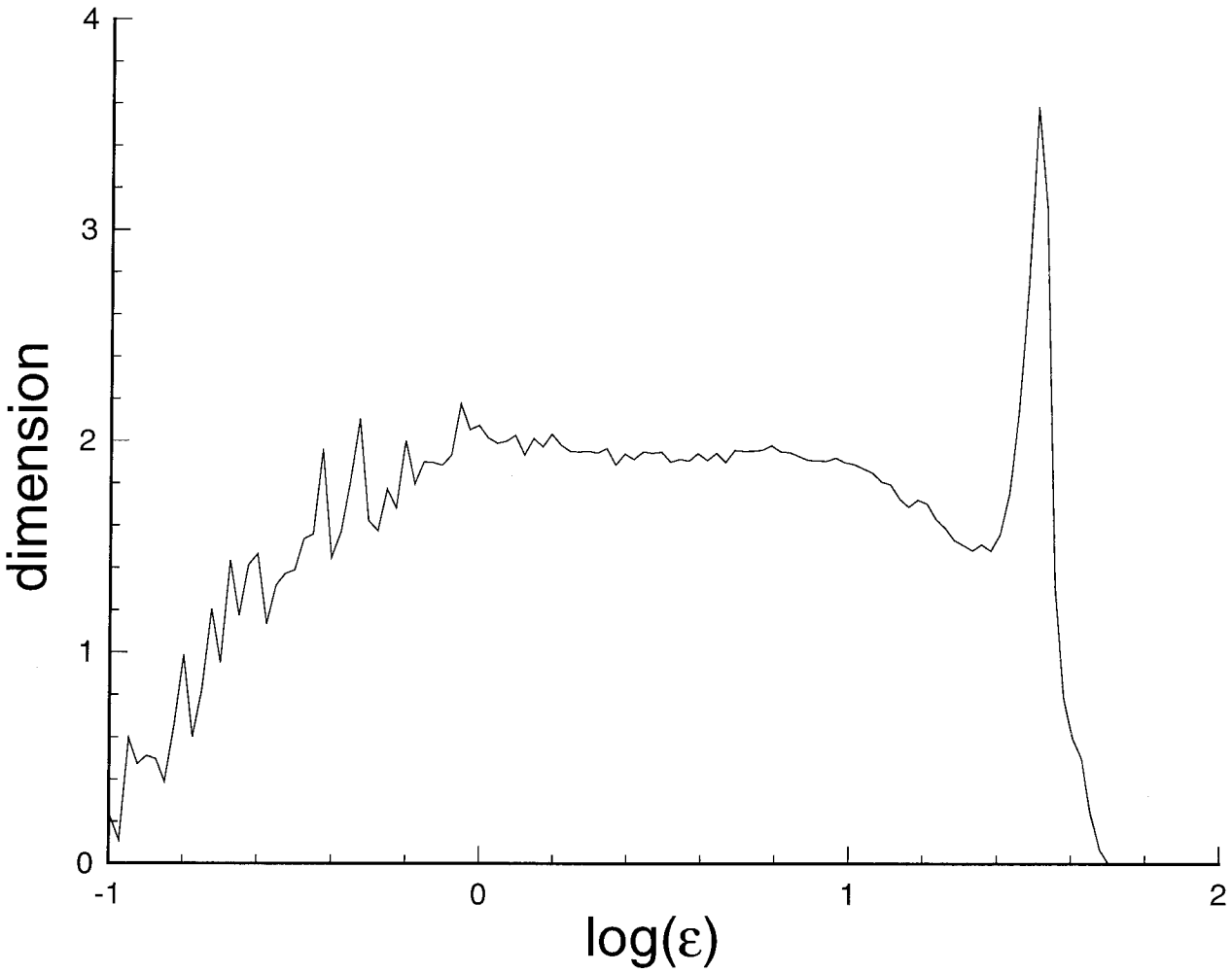

Figure 3.7: Plot of the slope from Fig. 3.6 showing the dimension of the Lorenz attractor

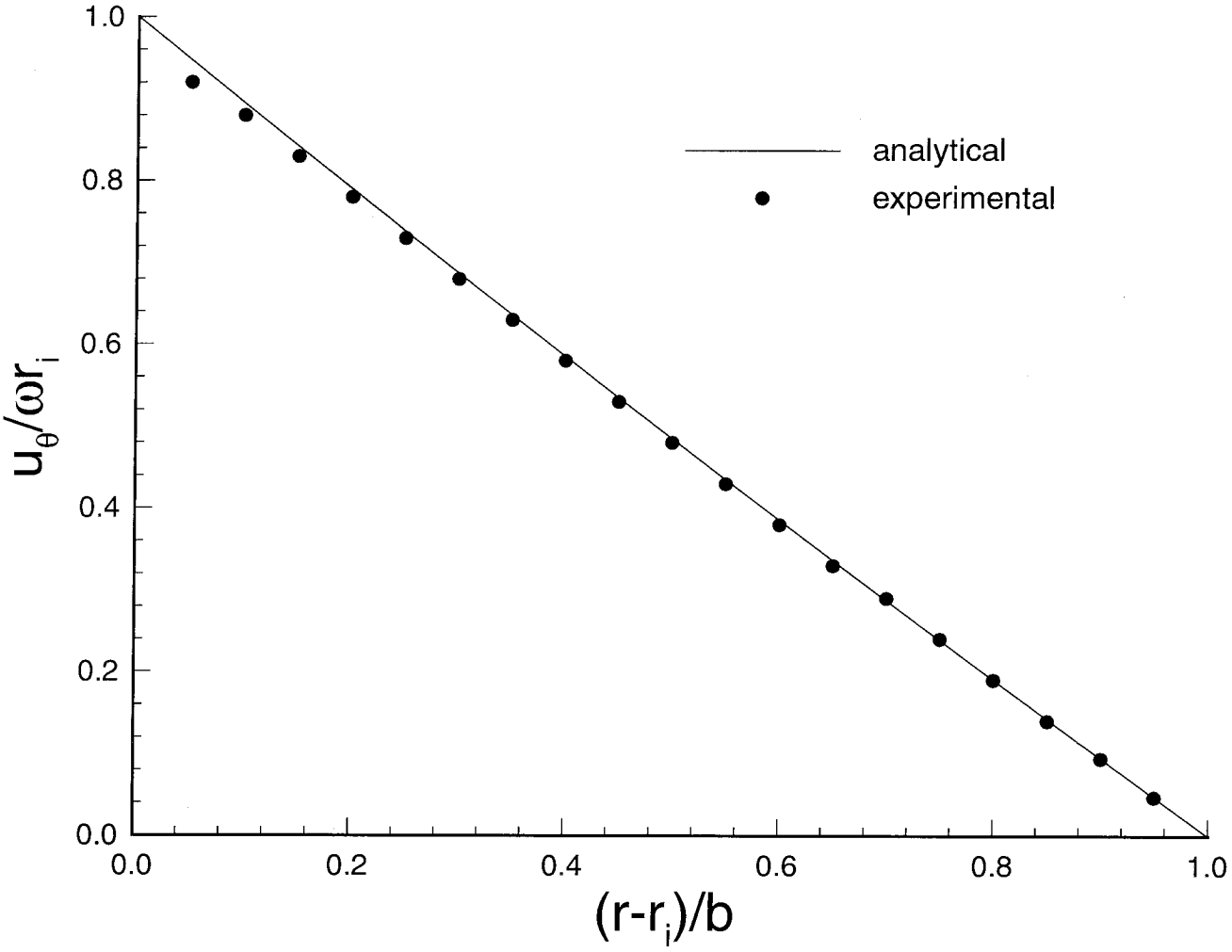

Figure 3.8: Analytical and experimental tangential velocity profile for circular Couette flow.

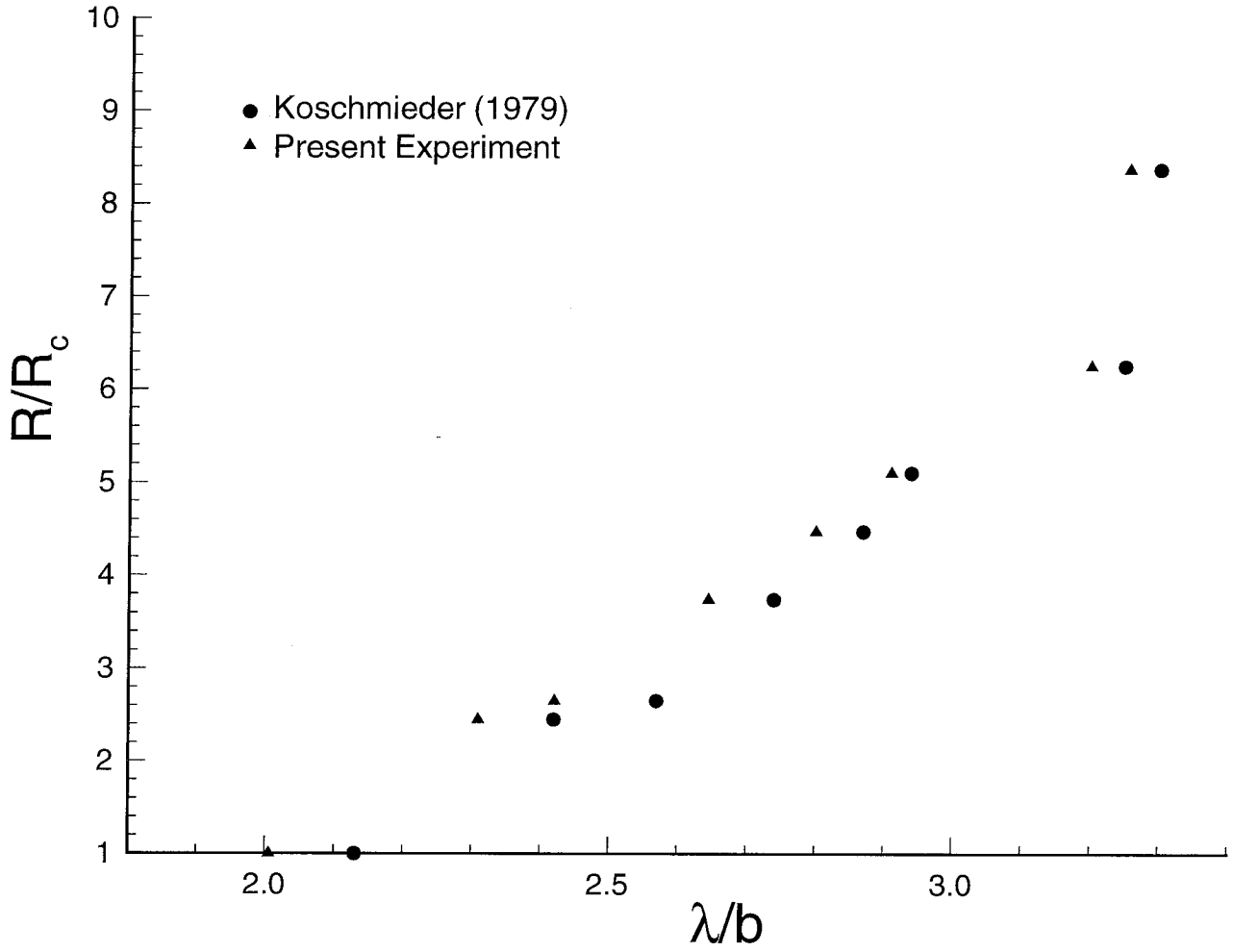

Figure 3.9: Variation of axial wavelength with Reynolds number for steady acceleration of the inner cylinder.

Chapter 4

Results

4.1 Heat Transfer Results

The code is compared with experimental results. One of the results from Kataoka, et al. (1977) is re-plotted in Fig. 4.1 (symbols). In their experiment, they measured the local coefficient of mass transfer on the outer cylinder. The Schmidt and Grashof numbers are not given in the paper, but are estimated to be of order 10^5 and 100, respectively. The figure also shows (solid lines) the numerical results for the local Nusselt numbers obtained for the numerical simulation for the same η and L_z but for a Pr=0.71. For $Gr\approx$100, the effect of natural convection is small and the flow state remains axisymmetric; hence in the heat transfer calculations, the Grashof number is taken to be zero. The local heat transfer coefficient is based on the temperature difference between the bulk of the fluid and the outer cylinder. The comparison between the mass transfer experiments and the heat transfer calculations show reasonable agreement. The simulations show that the adjacent Taylor cells are of equal size for Gr=0. However, the relative size of the Taylor cells varies with the increase in the differential heating of the two concentric cylinders. The slight difference in the relative size of the Taylor cells is also seen in Fig. 4.1 from the experimental values

of Kataoka, et al. (1977). This difference is probably due to a small Grashof number (based on mass transfer) effects. Note that the exponent for the Prandtl number has a value of 0.375, which was chosen to bring the results closer together. If the exponent is 0.333 (as used in the experiments), the values from the simulations are found to be smaller than the experimental values. The present simulation, when performed with a higher Prandtl number, give slightly higher Nusselt numbers. The case for R=110, L_z=1.88, η=0.617 and Gr=0 for different Pr is shown in Fig. 4.2. The simulation cannot be run for a very high Pr because the energy equation becomes stiff.

The second set of experiments used to validate the code is from the heat transfer experiments of Ball, et al. (1989). In this experiment, the walls were maintained at uniform temperatures. The inner cylinder was heated by a cartridge heater and the outer cylinder was cooled by passing an ethylene glycol-water mixture through a flexible plastic hose coiled around it. The mean equivalent conductivity, K_{eq}, is defined as the ratio of the average convective heat transfer coefficient ($h_{\bar{\theta},\bar{z},\bar{t}}$) to the heat transfer coefficient for pure conduction. The average convective heat transfer coefficient is based on the temperature difference between the inner and the outer cylinders. In Fig. 4.3 (symbols), K_{eq} is plotted versus R^2 for η=0.565, L_z=1.991, Gr=1900 and β^*=0.053. The normalized wavelength of approximately 1.991 is the critical wavelength corresponding to the critical Reynolds number for a radius ratio of 0.565 as given by the linear stability analysis. It is assumed that the axial wavelength remains fairly constant for the range of Reynolds numbers studied here, and that this critical wavelength is chosen as the axial period of the flow. The result shows a power law behavior (solid line), which has a lower coefficient and a higher exponent than the result presented by Ball, et al. (dashed line). This discrepancy arises because of the variation of axial wavelength with axial distance, which results from the thermal conditions at the ends of the experimental apparatus (Ball, personal communication).

The simplifying assumption of no axial temperature gradient could be another source of discrepancy between the experiment and the numerics. The simulations also show that for Gr=1900, as the Reynolds number is varied, the relative size of the adjacent counter-rotating Taylor cells change. This agrees qualitatively with the flow visualization studies of Ball, et al. (1989).

Figure 4.4 shows that the heat transfer results are very sensitive to the imposed axial wavelength. Plotted is the variation of the calculated K_{eq} with L_z. The same average heat transfer coefficient can be achieved by two different wavelengths: one below the isothermal critical value (L_z=1.988) and the other above it. A similar result was shown by Meyer (1967) in numerical calculations of torque (Fig. 4.5). The author concluded that the experimentally observed torque is somewhat lower than the numerical torque; it is speculated that the same is true for the heat transfer as well. Hence, if an axial wavelength was chosen for the numerical simulation that differed from the critical wavelength (either larger or smaller), the predicted equivalent conductivity would decrease and the predicted results would probably be closer to the experimental values from Ball, et al. (1989)

Apart from calculating the local and the average heat transfer coefficient, it is important to know how the flow evolves from one state to another as Gr is varied. Figure 4.6 presents a map of different stable states in the flow for a fixed Reynolds number and different Gr. For each different value of Gr in the plot, the flow was computed by imposing the temperature difference at t=0 and allowing the flow to evolve to its asymptotic state. For low $|Gr|$, axisymmetric Taylor Vortex Flow (TVF) is the stable state. Outside this range, n=1 stripes are formed. With the formation of spiral flow, the Taylor vortices become inclined. The angle of inclination of the Taylor cells from the horizontal (Ψ) increases as higher order spirals are formed. Figure 4.7 shows a schematic of spiral flows for n=1 and n=2. These spirals move an axial distance

of nL_z for one rotation around the inner cylinder. The flow becomes aperiodic for higher Gr.

Similar stripes were also seen in the flow visualization experiments of Snyder and Karlsson (1964) and Ball, et al. (1989). Stripes of larger inclination angle, up to n=6, were observed by Snyder and co-workers for higher heating in a small annulus ($\eta = 0.957$). Higher spiral modes are formed for narrower gaps (Ali, et al., 1990).

Increasing Gr decreases the heat transfer coefficient (K_{eq}) within the axisymmetric TVF regime. The increase in the axial velocity as a result of increasing Gr not only delays the onset of Taylor vortices but also causes a damping effect on the heat transfer. A similar effect of decreasing of the average Sherwood number by an added axial flow was also observed by Kataoka, et al. (1977). The mean equivalent conductivity, K_{eq}, increases significantly with the formation of n=1 spiral flow and it continues to increase with Gr until the flow becomes aperiodic with a subsequent decrease in K_{eq} near Gr=$\pm$2400. The map is nearly symmetric about the Gr=0 axis.

For η=0.6, the map is shown in Fig. 4.8. The map is similar to the one shown in Fig. 4.6 for η=0.5 except for the point Gr=-2000. For this value of Gr, n=2 spiral flow is formed and is not seen for positive Gr. The heat transfer characteristics are the same as that for η=0.5.

A similar map is shown for η=0.7 in Fig. 4.9. Again, axisymmetric Taylor vortex flow is seen for low $|Gr|$, but the n=1 spiral flow is formed for a broader negative range of Gr and for a narrower positive Gr. The n=2 spiral flow is formed for higher negative Gr and is not formed for positive Gr. The flow becomes aperiodic outside this range. The heat transfer has similar effects as for η=0.5 (Fig. 4.6) in the TVF regime. However, instead of K_{eq} increasing monotonically in the n=1 spiral flow regime, a plateau is formed for both positive and negative Grashof numbers. A significant increase in K_{eq} is observed with the formation of n=2 spiral flow, and

K_{eq} increases with further increase in Gr in this regime of flow. This map is not symmetrical about the Gr=0 axis. The asymmetry grows with the increase in the value of A.

The variation of the size of the Taylor cells with the increase in the value of Gr is shown in Fig. 4.10. The axial velocity contours are plotted in the r-z plane for η=0.7, L_z=2.001, R=100 and Pr=0.7. The figure illustrates two important phenomena. The first is the change in the size of Taylor cells and the second is the formation of n=1 spiral flow. For Gr=0, there is no effect of natural convection, and both the Taylor cells are of equal size. As Gr is increased, a natural convection current is set up. For a positive Gr, the direction of the convection current is upwards near the inner cylinder and downwards near the outer cylinder. As a result of this, the Taylor cell that has the same direction of circulation as the natural convection current increases in size. The counter-rotating cell, on the other hand, becomes smaller. The counter-rotating cell becomes very small for Gr=900. The flow remains axisymmetric. As Gr is increased to 1000, the cell cannot become any smaller and n=1 spiral flow is formed. The transition marks an increase in the Nusselt number, which is the result of an increase in the radial velocity component of the fluid.

The variation of heat transfer as a function of z and θ is shown in Fig. 4.11 (Gr=0), Fig. 4.13 (Gr=-1200), Fig. 4.15 (Gr=-1700) and Fig. 4.17 (Gr=-2100). All the four cases are for η=0.7, L_z=2.001, R=100 and Pr=0.7, which corresponds with map of Fig. 4.9 for the equivalent thermal conductivity. For Gr=0, the flow is axisymmetric and the Nusselt number is only a function of z. For Gr=-1200 and -1700 the variation is sinusoidal in both z and θ because the flow contains n=1 and n=2 spirals. The surface has more foldings for Gr=-1700 (n=2 spiral flow). For Gr=-2100 the Nusselt number varies with z and θ in a more complicated way because the flow is within the aperiodic regime. The radial velocity contours corresponding to Figs.

4.11, 4.13, 4.15 and 4.17 are plotted in Figs. 4.12, 4.14. 4.16 and 4.18, respectively. For Gr=-1200 and -1700, n=1 spiral flow and n=2 spiral flow are clearly evident. The radial velocity contours for Gr=-2100 show that the flow is wavy and there is no single dominant frequency.

Finally, the frequencies and the amplitudes of local fluctuations of the heat transfer coefficient (h) present in the flow are shown in Figs. 4.19, 4.20 and 4.21. The three plots are for three different radius ratios of η=0.5, 0.6 and 0.7. The frequency is normalized by the cylinder frequency and the amplitude is normalized by the spatially and temporally averaged heat transfer coefficient. For Gr=0, both the frequency and the amplitude of local fluctuations of the heat transfer coefficient are zero. Figure 4.19 shows that for both Gr=1200 and -1200, the frequency normalized by the cylinder frequency is small ($\simeq$0.01) but the normalized amplitude is high ($\simeq$0.9). In the spiral flow regime (n=1), the normalized frequency increases monotonically and the normalized amplitude is fairly constant. Also, note a small dip in the normalized amplitude with the formation of n=1 spiral flow. Figure 4.20 shows the case for η=0.6. As for η=0.5, the normalized frequency increases monotonically. For n=2 spiral flow, f/f_c=0.66. A similar dip, as for η=0.5, in the normalized amplitude is observed with the formation of spiral flow. Figure 4.21 shows that $f/f_c\simeq$0.35 for n=1 and the amplitude of local fluctuations of heat transfer is about 95% of $h_{\bar{\theta},\bar{z},\bar{t}}$. In contrast to the cases for η=0.5 and 0.6, the normalized frequency decreases monotonically in n=1 spiral flow regime. For n=2 spiral flow, f/f_c remains practically constant at 0.74. The normalized amplitude on the other hand increases monotonically with the increase in the magnitude of Gr. The above information on the frequency and the amplitude of local fluctuations of heat transfer is required as boundary conditions for a thermal stress analysis of the shaft and cover of BWR pumps. With the assumption that the frequency fluctuation is about 10% to 100% of the rotating speeds, the predictive

models (Gopalakrishnan, et al., 1992) revealed crack depths that were comparable to field observations for the shaft and cover.

4.2 Hysteresis

Coles (1965) observed as many as 25 different stable states at a given speed for isothermal Taylor-Couette flow. The speed was reached by varying the acceleration rates of the rotating cylinder. The final state in Taylor-Couette flow is thus widely believed to be dependent on its previous history. Figure 4.22 shows the different stable states present in the flow as Gr is slowly varied. The case is for η=0.7, L_z=2.001, Pr=0.7 and a fixed Reynolds number (R=100). The different states are marked from 1 to 7 in the symbol table in the order in which Gr is slowly increased and then decreased. As Gr is slowly increased from 0 to 900, axisymmetric TVF is formed. From Gr=1000 to 1700, n=1 spiral flow is formed; n=2 spiral flow is formed from Gr=1800 to 2200. As Gr is decreased from 2200, n=2 spiral flow exists until Gr=500. There exist two different stable states (axisymmetric TVF and n=2 spiral flow) for Gr=600, but with same heat transfer coefficient. Axisymmetric TVF is achieved by slowly increasing Gr; then n=2 spiral flow is achieved by slowly decreasing Gr. For Gr=400 to -1700, n=1 spiral flow is formed. With a further decrease in Gr, n=2 spiral flow is formed for Gr=-1800 to -2300. The figure shows the property of non-uniqueness by the existence of a hysteresis loop.

4.3 Colburn's Analogy

Most turbulent flows satisfy the famous empirical formula suggested by Colburn:

$$St.f(Pr) = C_f/2 \tag{4.1}$$

where St is the Stanton number and C_f is the friction factor as defined below.

$$St = \frac{h_{\bar{\theta},\bar{z},\bar{t}}}{\rho(\omega r_i)C_p}$$
$$C_f = \frac{\tau_w|_{\bar{\theta},\bar{z},\bar{t}}}{\frac{1}{2}\rho(\omega r_i)^2}$$

For planar Couette flow, $f(Pr) = Pr$, but it is usually equal to $Pr^{\frac{2}{3}}$ for turbulent boundary layers. For circular Couette flow, there is an additional geometric parameter(η). However, as η approaches 1, $f(Pr) = Pr$ (Appendix B). Figure 4.23 shows the variation of $f(Pr)$ with R for η=0.7, L_z=2.001, Pr=0.7 and Gr=0. The geometric factor has been incorporated into $f(Pr)$ such that for η=0.7, $f(Pr) = Pr$ for circular Couette flow. The dots are the simulation results. The critical Reynolds number for this radius ratio is 79.49. Therefore, for the points R=60 and 70 (circular Couette flow), $f(Pr) = Pr$. As the Reynolds number is increased, $f(Pr)$ increases and reaches a maximum just above $Pr^{\frac{2}{3}}$ and finally becomes constant at $0.76{=}Pr^{0.77}$.

Figure 4.24 shows a similar correlation for η=0.7, L_z=2.001, Pr=0.7 and R=100. Here $f(Pr, Gr)$ is plotted with Gr for a fixed Reynolds number (R=100). The results are similar to the stable states map shown in Fig. 4.9 for η=0.7.

4.4 Time Delay Analysis

4.4.1 Experiment

Time series

The time series were collected using a hot-wire anemometer. The axis of the hot-wire was kept parallel to the axis of the cylinders. In this position, the hot-wire measured both the tangential and the radial velocity components. The wire was placed halfway between the inner and the outer cylinders at the mid-axial position. Voltage time series are shown in Figs. 4.25 and 4.26 for R/R_c=1.6 and 11.1. The voltage signals were sampled at 20Hz and 40Hz respectively. The mean voltage is subtracted and hence, only the fluctuating component is shown in the figures. The time trace for R/R_c=1.6 (Fig. 4.25) show that the flow is in the periodic regime. For R/R_c=11.1, the flow has become vastly irregular.

Power spectra

The state of the fluid can be better understood from the power spectra. The power spectra were obtained from the time series by Fast Fourier transform methods. Shown in Figs. 4.27 and 4.28 are the corresponding power spectra for the time series in Figs. 4.25 and 4.26. In the first spectrum, for R/R_c=1.6, there is only one fundamental frequency and its harmonics. The fundamental and the harmonics are all above a flat, experimental background noise. As the Reynolds number is increased (R/R_c=11.1), the system seems to be making the transition to turbulence. The background noise rises well above the instrumental noise. The instrumental noise level was ascertained by taking the power spectrum of a time series obtained in a quiescent medium. For R/R_c=11.1, the flow should be quasi-periodic. Quasi-periodicity is not clearly evident from its power spectrum. It is conjectured that the second fundamental frequency is

buried under the background fluid noise. The spectra for higher Reynolds numbers are of a broad-band nature.

Reconstruction of the attractor

The attractor may be reconstructed from a time series by following the procedure outlined in chapter 3 (section 1.1). Time delay vectors were created from the time series, with each vector element chosen by a time delay. This carefully chosen set of vectors spans the space in which the attractor was reconstructed. A suitable time delay was needed to reconstruct the attractor. This time delay was estimated by calculating the mutual information function, $I(\tau)$, as explained in chapter 3 (section 1.2).

The mutual information functions calculated for the time series in Figs. 4.25 and 4.26 are shown in Figs. 4.29 and 4.30. For R/R_c=1.6 (Fig. 4.29), there are more than one minimum. Practically, the first minimum must be chosen over the latter minima because the attractor gets folded upon itself, and it becomes extremely difficult to extract the dimension and other information. For R/R_c=11.1, the mutual information reaches a minimum and then practically becomes a constant. The delay time was found to be a function of the Reynolds number. Thus a delay time of 8 time steps was chosen for R/R_c=1.6 and 11.1. This translated into a non-dimensional delay time of 0.14 and 0.49 for the two cases respectively. The time was non-dimensionalized using the time period of the inner rotating cylinder.

After calculating the time delay one may proceed with the reconstruction of the attractor. The projections of phase plots in two dimensions for the time series are shown in Figs. 4.31 and 4.32. For R/R_c=1.6, the flow is periodic (WVF) and the attractor should be a limit cycle, which is clearly seen in the figure. The thickness of the limit cycle is due to the experimental noise. For R/R_c=11.1, the flow should

be quasi-periodic (MWVF) and the associated attractor should be a torus. The reconstructed attractor is very fuzzy with very little features of a torus. The fuzziness is probably due to background noise.

Dimension determination

As discussed in chapter 3 (section 1.3), the pointwise dimension D_1 and the correlation dimension D_2 were computed. Both the dimensions were calculated using the same algorithms, once by averaging the logarithm of the number of points and again by taking the logarithm of the averaged points. There was no appreciable change in these two calculated dimensions. Therefore only the pointwise dimension D_1 is reported here. Embedding was done in six-dimensional phase space. Higher dimensional embedding was also done with no change in the attractor dimension. For a six-dimensional embedding, 256 reference points were chosen. These reference points were selected using uniformly generated random numbers, so that the reference points are spread out through the entire attractor equally.

Plots of $\log N(\epsilon)$ versus $\log(\epsilon)$ for R/R_c=1.6 and R/R_c=11.1 are shown in Figs. 4.33 and 4.34. According to equations (3.5) and (3.6), the slopes of the graphs in Figs. 4.33 and 4.34, in the limit $\epsilon \to 0$, should give the dimension of the reconstructed attractor. Graphs of the local slope, $d[\log N(\epsilon)]/d[\log(\epsilon)]$ are shown in Figs. 4.35 and 4.36. For very small ϵ, the number of points $N(\epsilon)$ and the slope both approach zero because of the finite number of data points. Instrumental noise is dominant for a slightly larger ϵ. The m-dimensional hyper-sphere is smaller than the smallest scales that can be resolved in the experiment. Since random noise resides in a higher dimension than the actual dimension of the attractor, the slope is seen to be higher. For higher ϵ (if the embedding dimension is sufficiently large), a constant slope reflects the actual dimension of the attractor, which is of primary interest. For very large ϵ, the

hyper-sphere approaches the size of the attractor. The number of points, $N(\epsilon)$, saturates to a value corresponding to the total number of data points and subsequently the slope approaches zero. For R/R_c=1.6, a slope of 1 is visible, which is the right value for a limit cycle. For R/R_c=11.1, there is no distinct region of constant slope. Although the dimension is seen to be continuously decreasing from 4 to 0.

4.4.2 Computation

In the previous section, a time delay analysis of a velocity time series obtained from a Taylor-Couette experiment is performed using the dynamical systems method. The same method is used to analyze the time trace obtained from the numerical simulation.

Time series

The radial velocity halfway between the inner and the outer cylinders at the mid-axial position is recorded at every time step. Figure 4.37 shows the fluctuating component of the radial velocity (the mean velocity has been subtracted) for η=0.7, L_z=2.001, R=100, Pr=0.7 and Gr=-1700. The flow is in the n=2 spiral flow regime. The time trace looks regular and periodic. Shown in Fig. 4.38 is a similar velocity trace for Gr=-2100. The time trace has become irregular and the flow is in the aperiodic regime. Both the time traces are shown after the initial transients have died down.

Power spectra

The power spectra of the radial velocity time series were obtained by performing a Fast Fourier Transform. Shown in Figs. 4.39 and 4.40 are the respective power spectra for Gr=-1700 and Gr=-2100. The radial velocity contours at the mid radial section are shown in Figs. 4.16 and 4.18. Figure 4.39 shows a fundamental frequency at f/f_c=0.74 and its harmonics. The flow is clearly periodic in nature. For the case of

Gr=-2100 (Fig. 4.40), the peaks for Gr=-1700 are still present but their amplitudes have slightly decreased. Also, other frequencies have appeared in the flow that are of comparable power density.

Reconstruction of the attractor

The radial velocity vectors can be used for the reconstruction of the attractor by following the method described in chapter 3 (section 1.1). Before the attractor can be constructed, a suitable time delay must be determined. For this purpose, the mutual information function is calculated from the time series for η=0.7, L_z=2.001, R=100 and Pr=0.7. The two cases for Gr=-1700 and Gr=-2100 are shown in Figs. 4.41 and 4.42. The mutual information for Gr=-1700 is periodic, as is expected for a periodic signal. On the other hand, the mutual information for Gr=-2100 (Fig. 4.42) reaches a minimum and then fluctuates above a constant value. From the figures, a delay time steps of 60 and 30 were chosen for Gr=-1700 and -2100. The corresponding non-dimensional times are 6 and 3 respectively.

The phase plots for Gr=-1700 and Gr=-2100 are shown in Figs. 4.43 and 4.44. For Gr=-1700, a clean limit cycle is seen for n=2 spiral flow (periodic). The limit cycle is triangular due to the presence of harmonic frequencies of the fundamental. For Gr=-2100, the reconstructed attractor has become vastly irregular and the limit cycle has disappeared.

Dimension determination

The pointwise dimension D_1 is calculated for the two different flows (n=2 spiral flow and aperiodic flow). Plots of $\log N(\epsilon)$ versus $\log(\epsilon)$ for Gr=-1700 and Gr=-2100 are shown in Figs. 4.45 and 4.46. The slopes of the graphs give the dimension of the reconstructed attractor. The slopes for the above cases are shown in Figs. 4.47 and

4.48. For Gr=-1700, a constant slope of approximately 1 is seen which reflects the periodic nature of the reconstructed attractor. For Gr=-2100 (Fig. 4.48), the slope continuously increases to a value of about 3.2. The constant slope region is small and hence the dimension cannot be determined precisely. If there were three irrationally related frequencies present in the flow, then the dimension of the flow would be 3.

4.4.3 Local heat transfer coefficient

The same process of time delay analysis is repeated for the local heat transfer coefficient. The time series for Gr=-1700 and -2100 is shown in Figs. 4.49 and 4.50, respectively. The time series for the local heat transfer coefficient and the radial velocity (Figs. 4.37 and 4.38) look very similar. The power spectra for the two Grashof numbers are given in Figs. 4.51 and 4.52. The magnitude of the power is two orders of magnitude higher than the corresponding power spectra for the radial velocity. However, the peaks occur at virtually the same frequencies. The mutual information calculations are shown in Figs. 4.53 and 4.54. Time delays of 6 and 3 were chosen for Gr=-1700 and -2100 for the phase plots shown in Figs. 4.55 and 4.56. As for the radial velocity case, a limit cycle is observed for Gr=-1700, which disappears for Gr=-2100. Shown in Figs. 4.57, 4.58, 4.59 and 4.60 are the dimension calculations for the local coefficients of heat transfer. The dimension for Gr=-2100 is approximately 3.2, which agrees remarkably well with the dimension obtained from the radial velocity time trace. Therefore, it is concluded that the local heat transfer coefficient follow the radial velocity pattern, with the reason being the active role of the radial velocity component in transferring heat between the two cylinders.

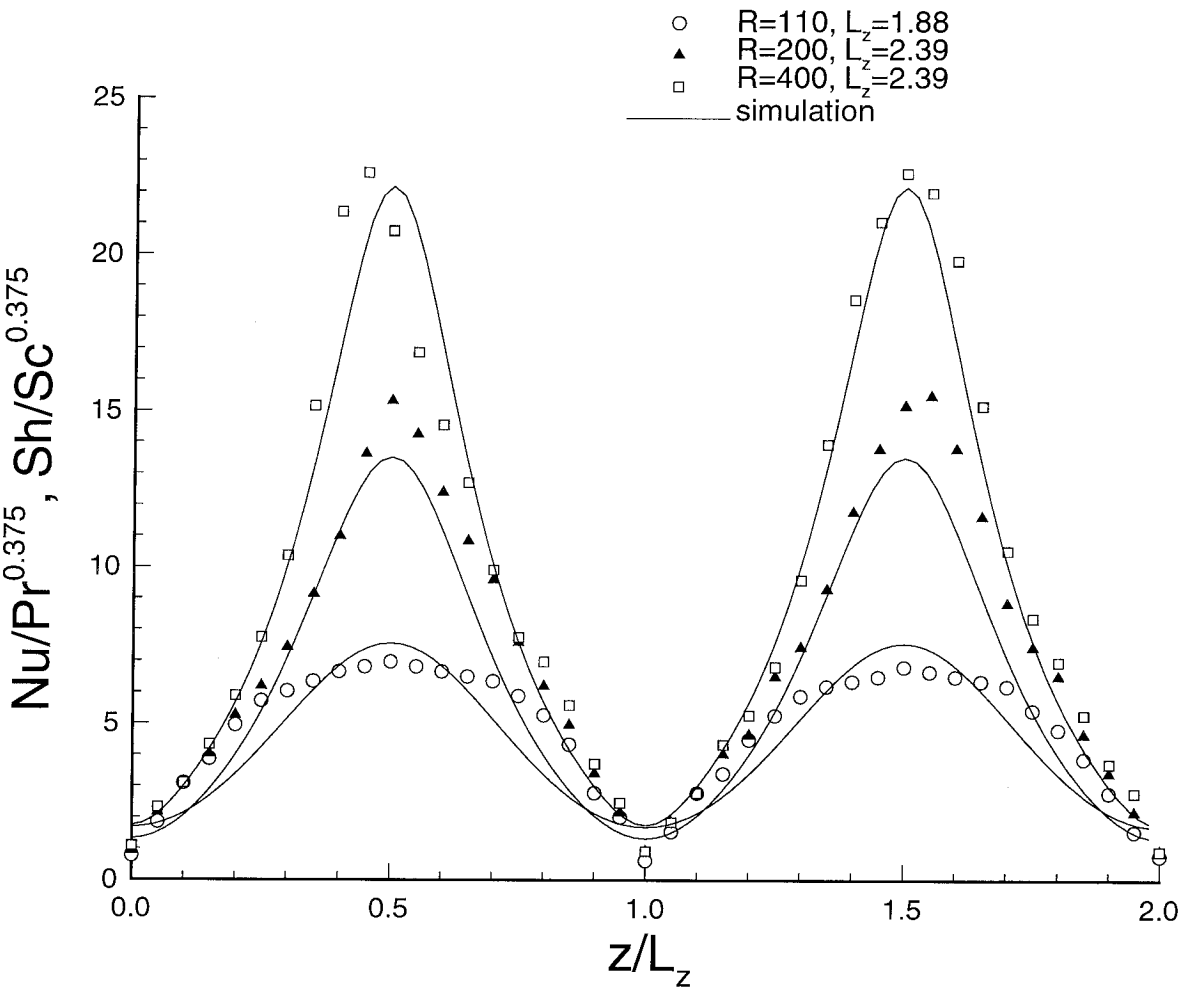

Figure 4.1: Variation of heat (present simulation) and mass transfer (Kataoka, et al., 1977) on the outer cylinder for η=0.617.

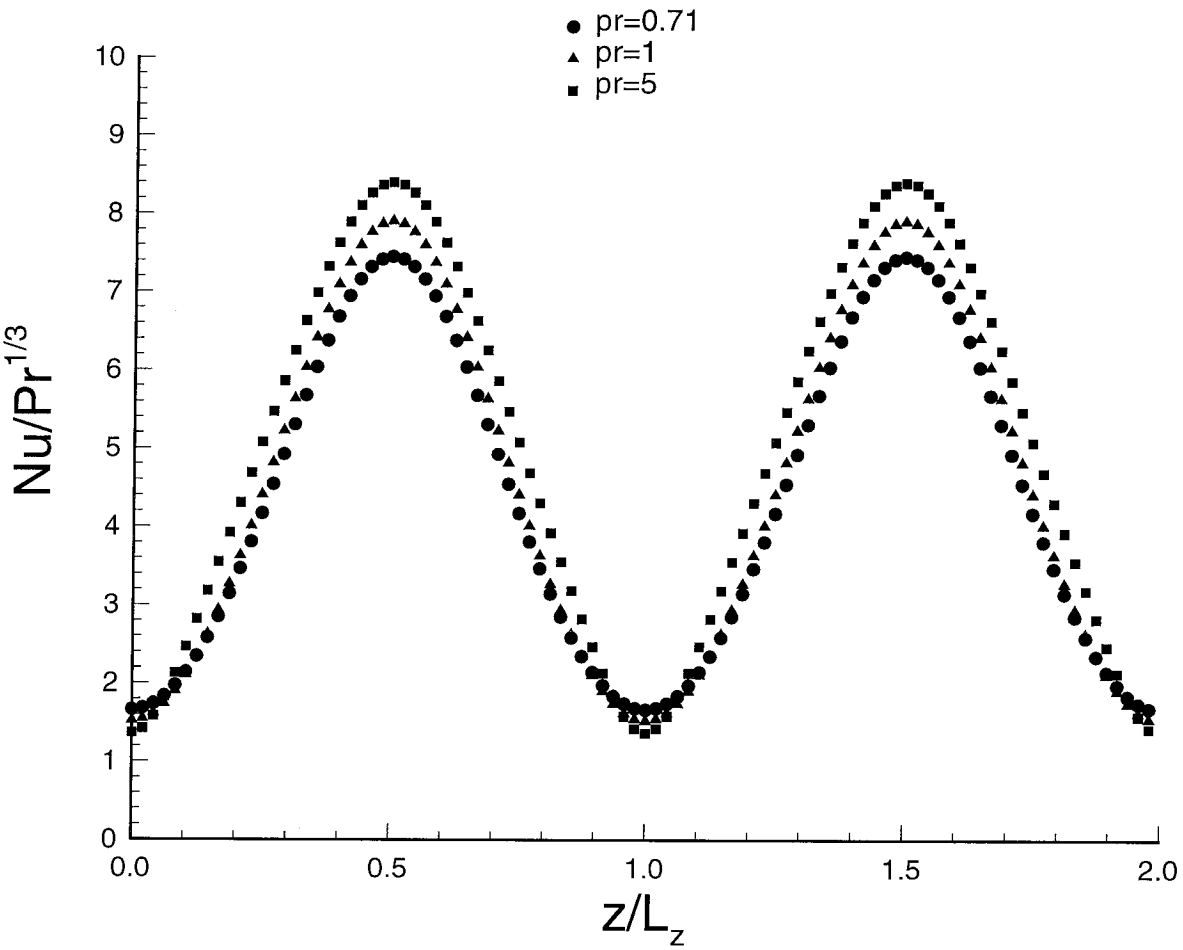

Figure 4.2: Variation of heat transfer with Pr on the outer cylinder for R=110, L_z=1.88, η=0.617 and Gr=0.

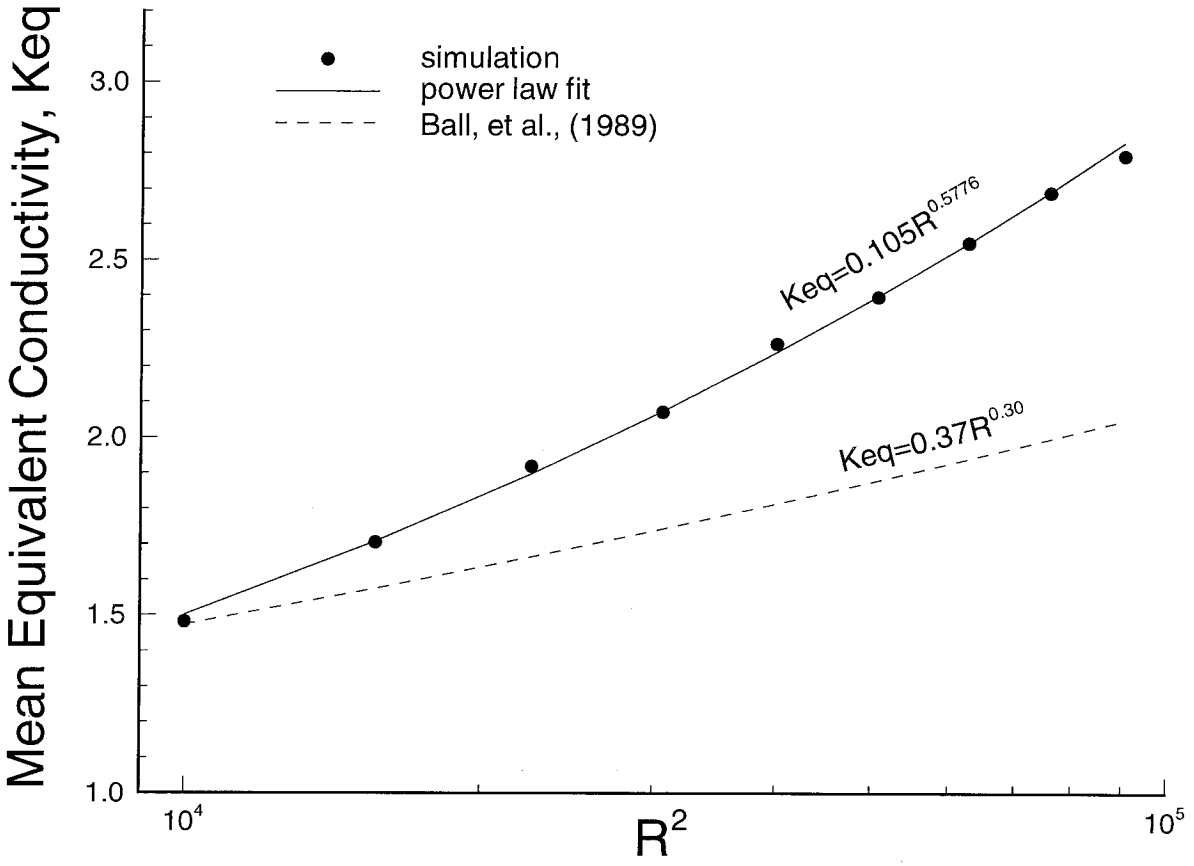

Figure 4.3: Variation of heat transfer rate with R^2 for η=0.565, L_z=1.991, Gr=1900 and β^*=0.053.

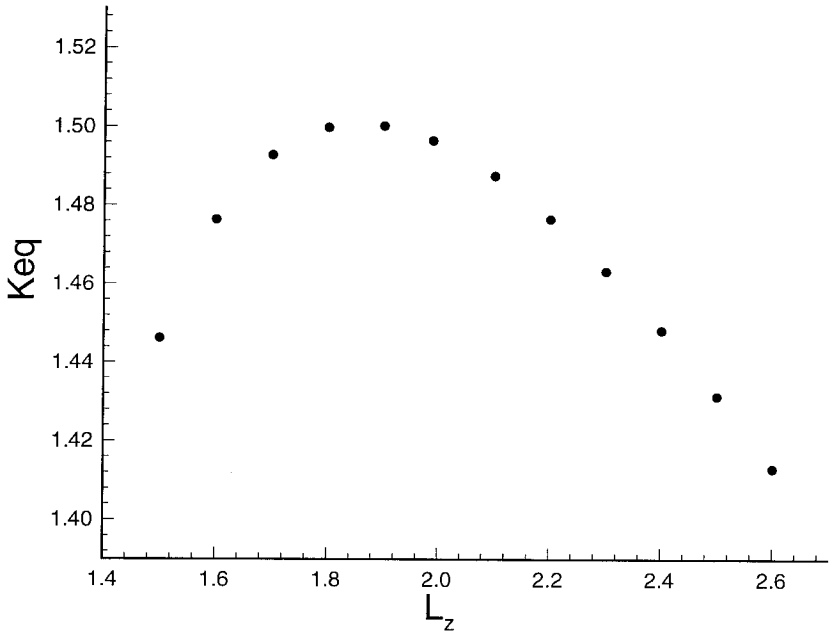

Figure 4.4: Variation of mean equivalent conductivity with L_z for η=0.5, R=100, Gr=1700 and β^*=0.0128.

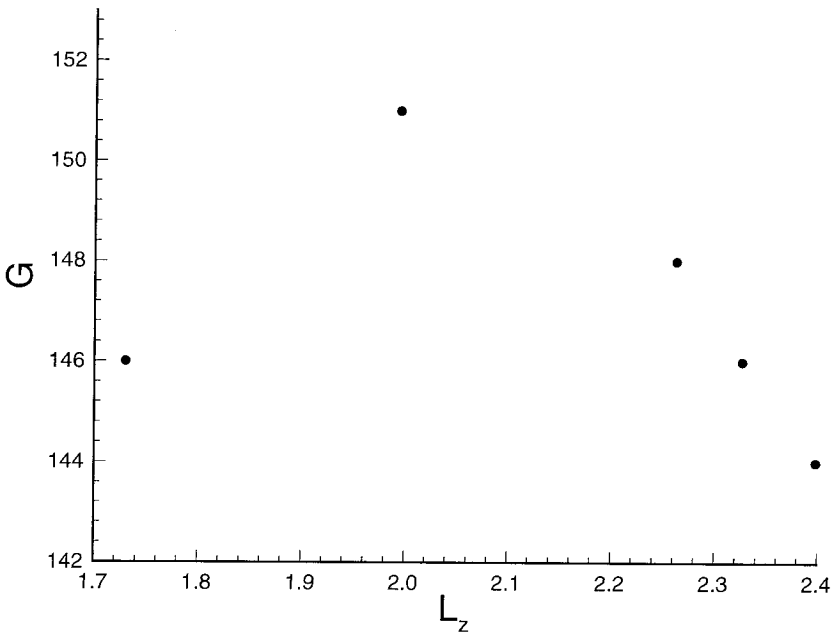

Figure 4.5: Variation of torque with L_z from Meyer (1967)

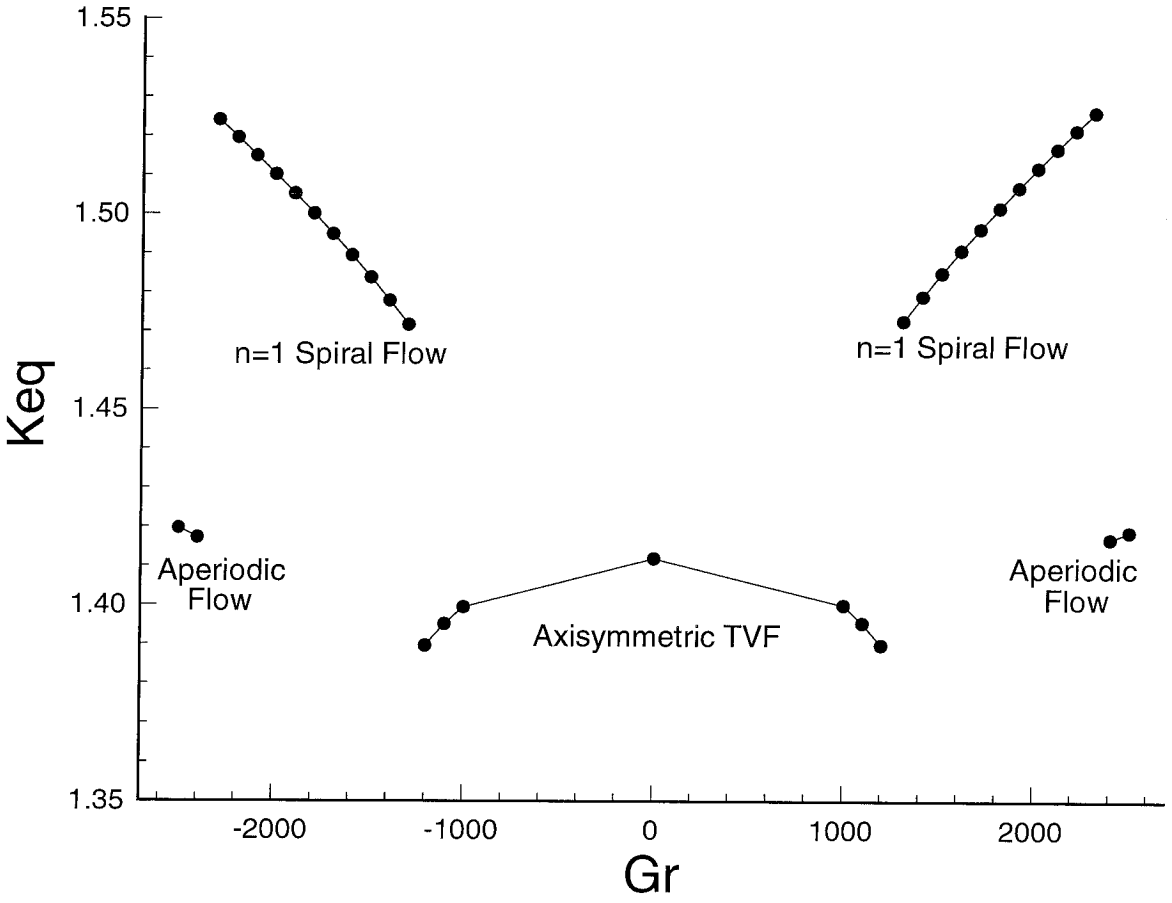

Figure 4.6: Map showing different stable states present in the flow for η=0.5, L_z=1.988, R=100, Pr=0.7 and A=0.1285.

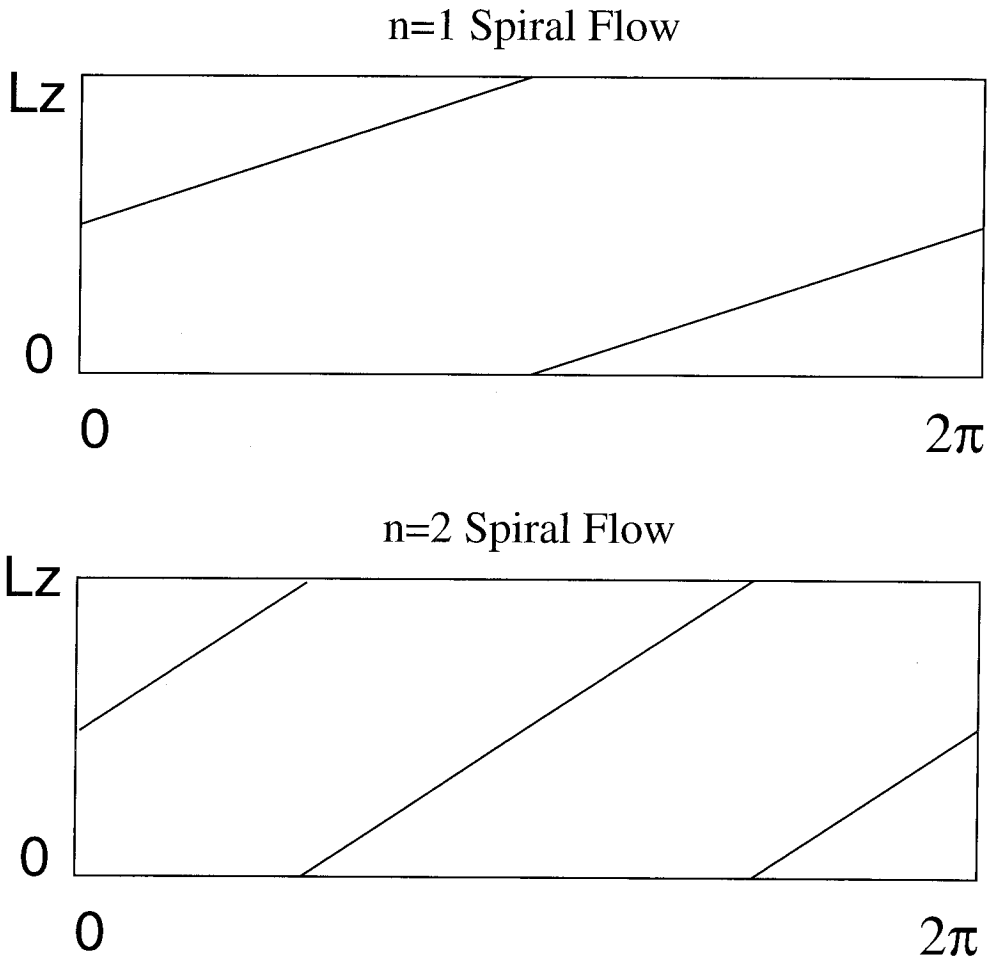

Figure 4.7: Schematic of spiral flows.

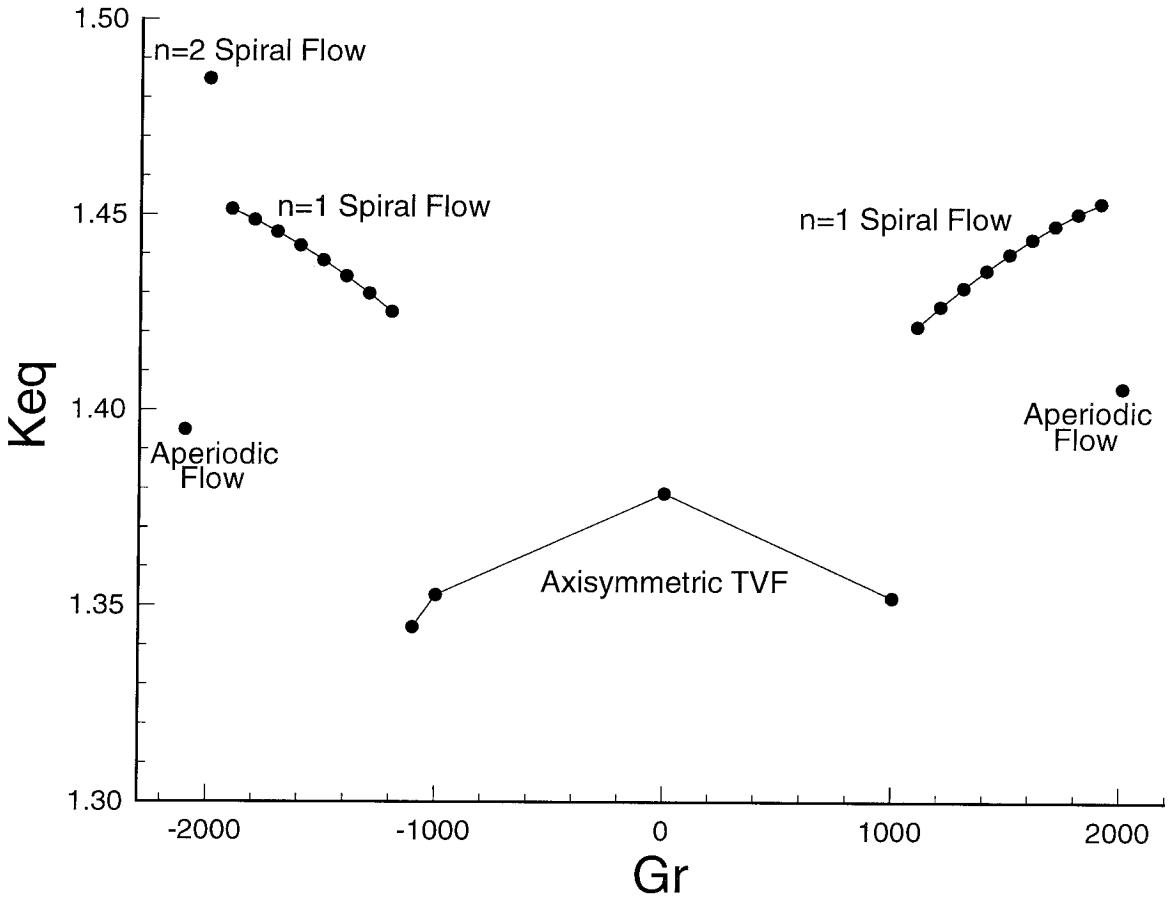

Figure 4.8: Map showing different stable states present in the flow for η=0.6, L_z=1.994, R=100, Pr=0.7 and A=0.2888.

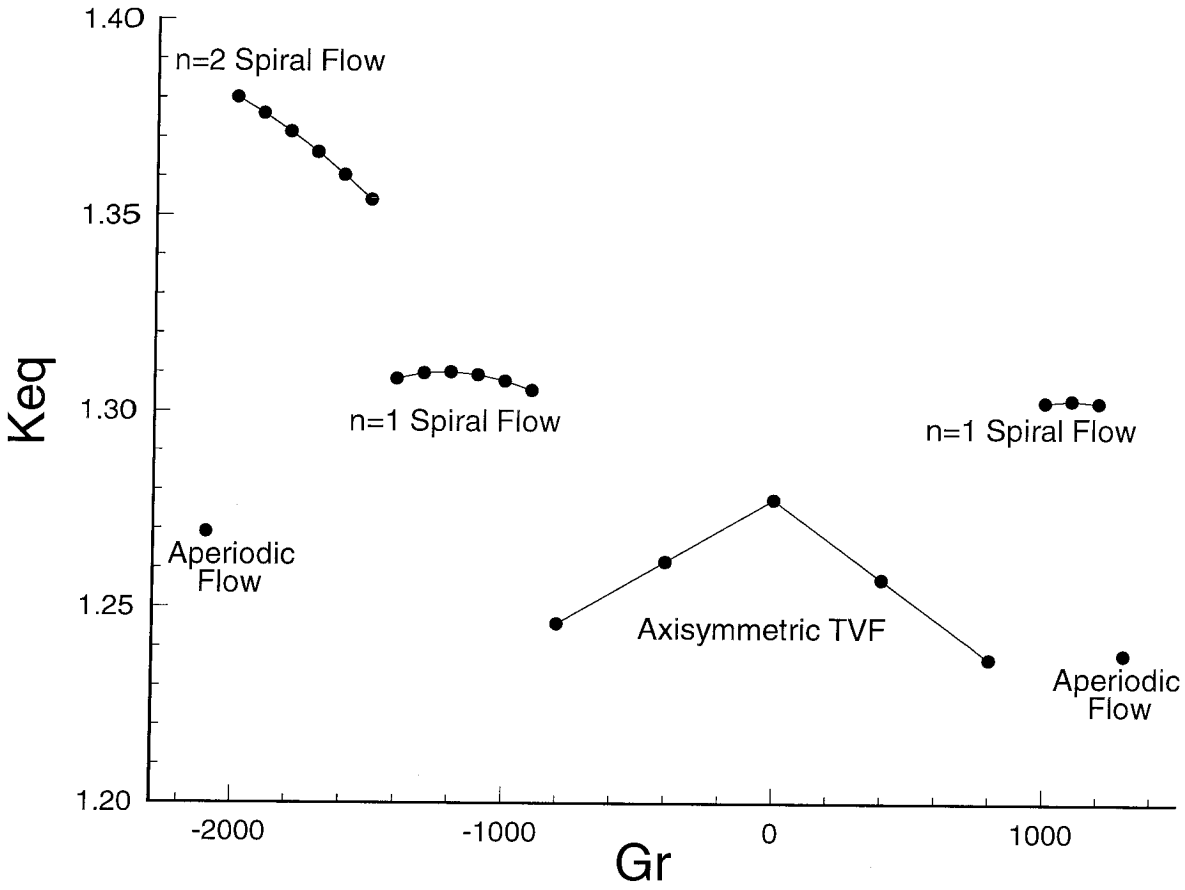

Figure 4.9: Map showing different stable states present in the flow for η=0.7, L_z=2.001, R=100, Pr=0.7 and A=0.67.

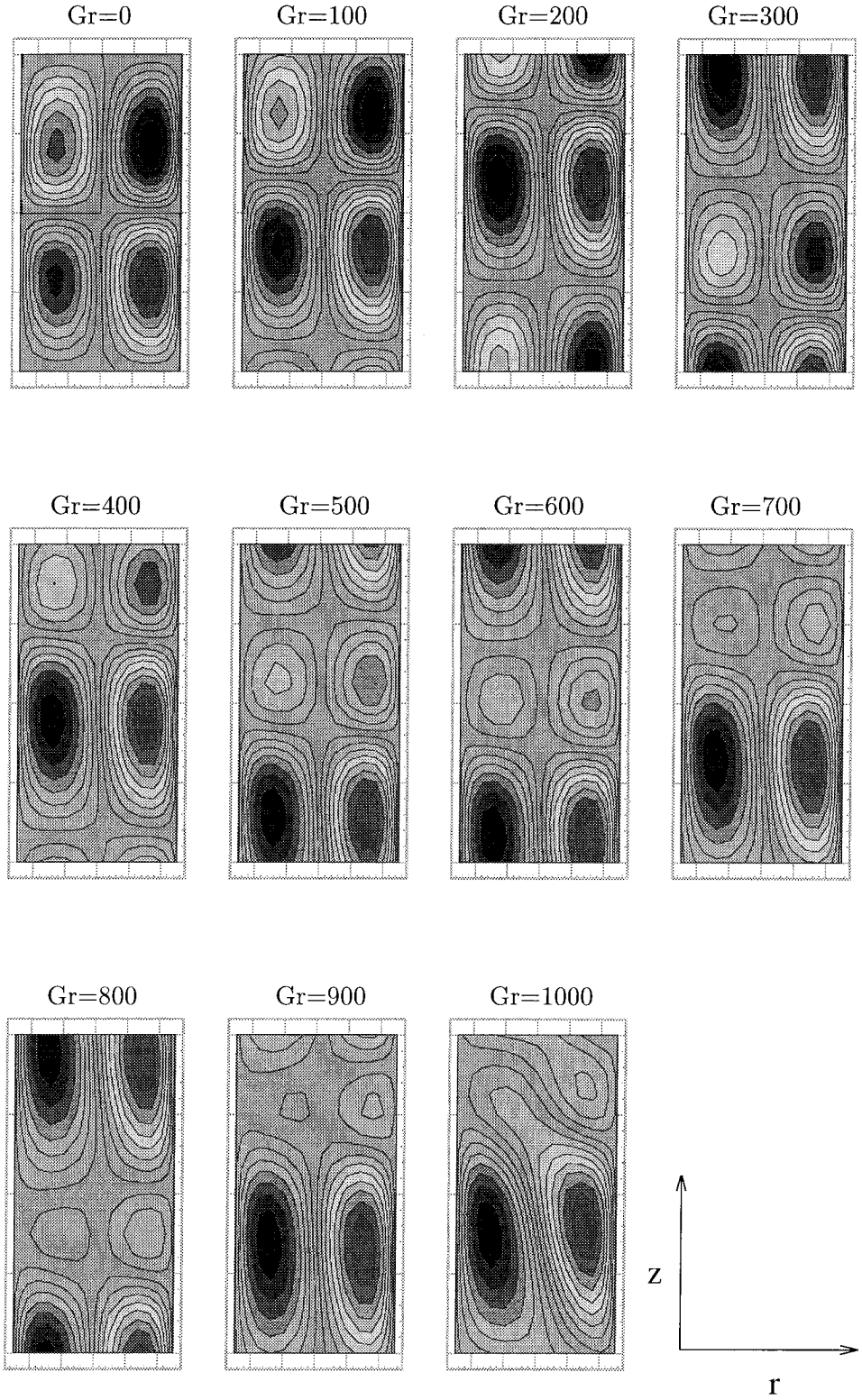

Figure 4.10: Change in the size of Taylor vortices with Grashof number for η=0.7, L_z=2.001, R=100 and Pr=0.7.

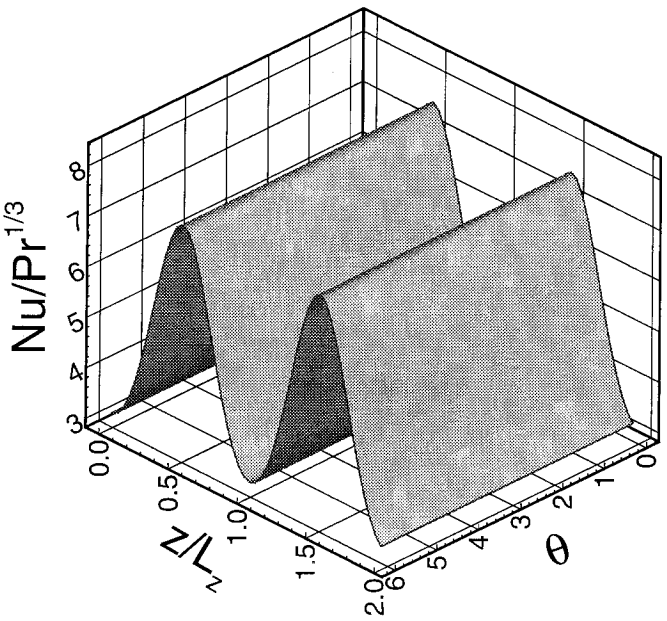

Figure 4.11: Variation of heat transfer on the outer cylinder for η=0.7, L_z=2.001, R=100, Pr=0.7 and Gr=0.

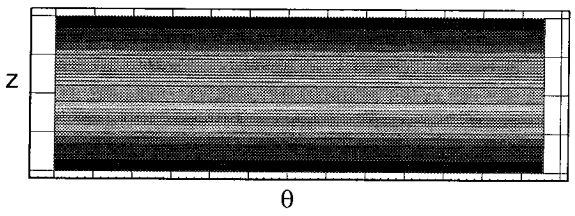

Figure 4.12: Radial velocity contours at the mid radial section of the two cylinders for η=0.7, L_z=2.001, R=100, Pr=0.7 and Gr=0.

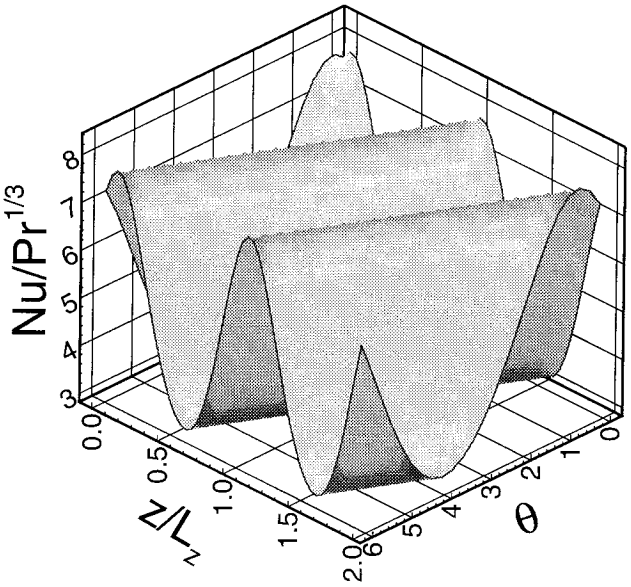

Figure 4.13: Variation of heat transfer on the outer cylinder for η=0.7, L_z=2.001, R=100, Pr=0.7 and Gr=-1200.

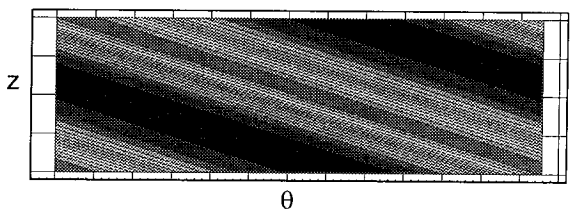

Figure 4.14: Radial velocity contours at the mid radial section of the two cylinders for η=0.7, L_z=2.001, R=100, Pr=0.7 and Gr=-1200.

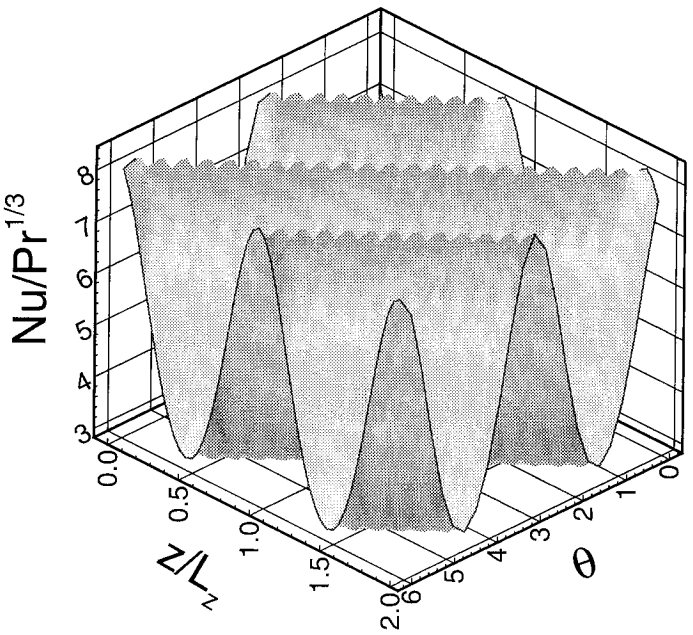

Figure 4.15: Variation of heat transfer on the outer cylinder for η=0.7, L_z=2.001, R=100, Pr=0.7 and Gr=-1700.

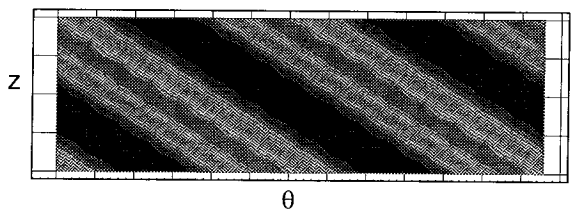

Figure 4.16: Radial velocity contours at the mid radial section of the two cylinders for η=0.7, L_z=2.001, R=100, Pr=0.7 and Gr=-1700.

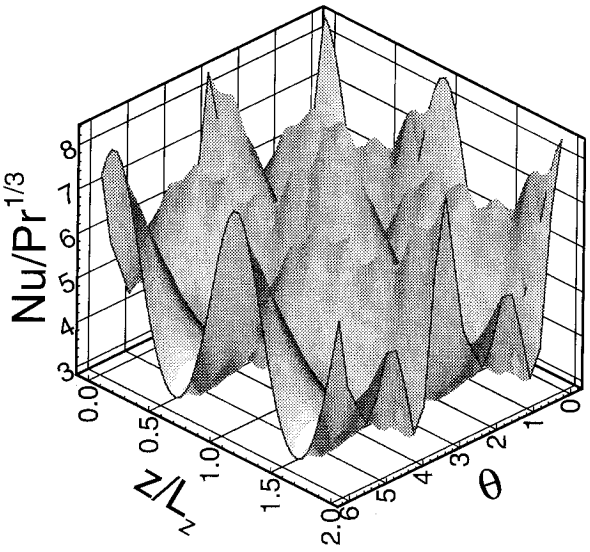

Figure 4.17: Variation of heat transfer on the outer cylinder for η=0.7, L_z=2.001, R=100, Pr=0.7 and Gr=-2100.

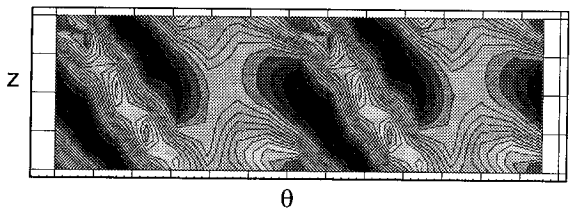

Figure 4.18: Radial velocity contours at the mid radial section of the two cylinders for η=0.7, L_z=2.001, R=100, Pr=0.7 and Gr=-2100.

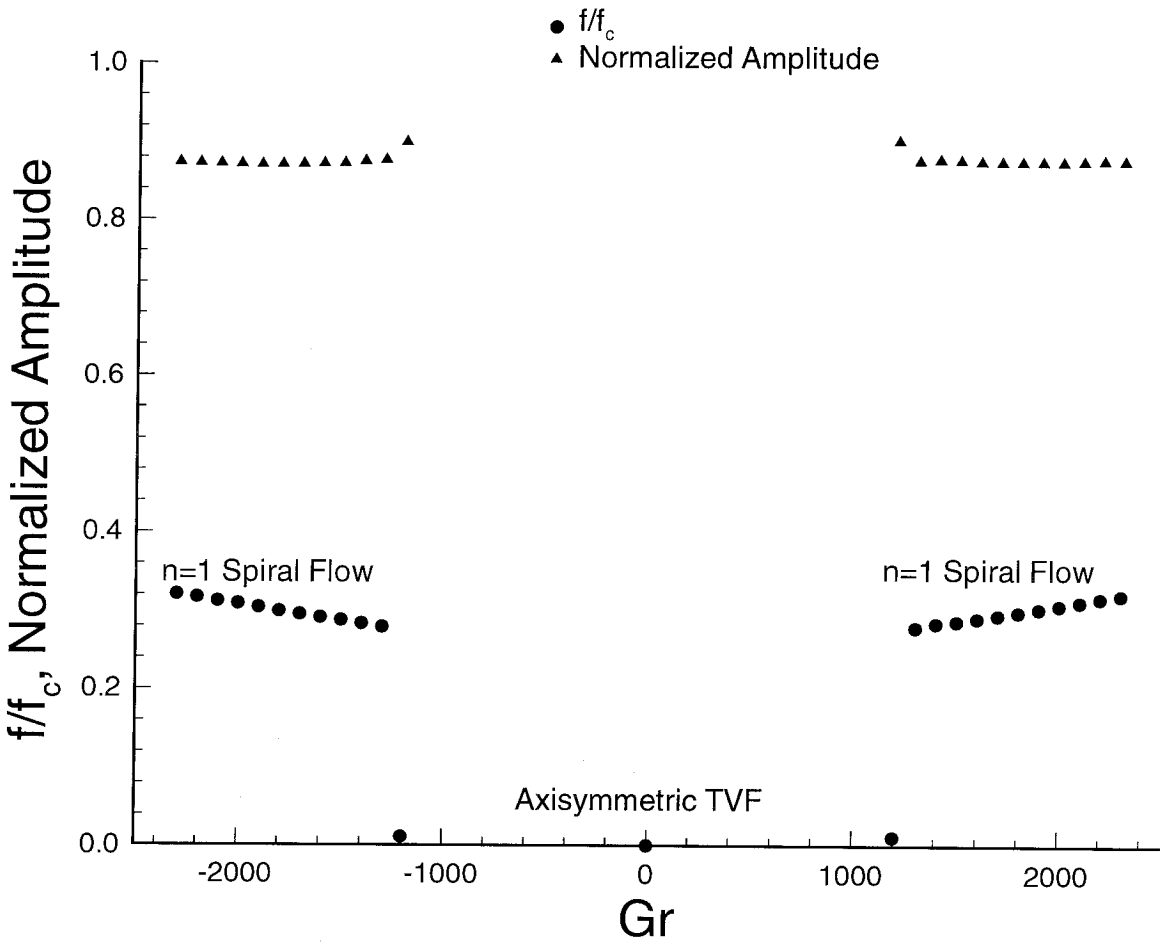

Figure 4.19: Variation of frequency and amplitude with Grashof number for η=0.5, L_z=1.988, R=100, Pr=0.7 and A=0.1285.

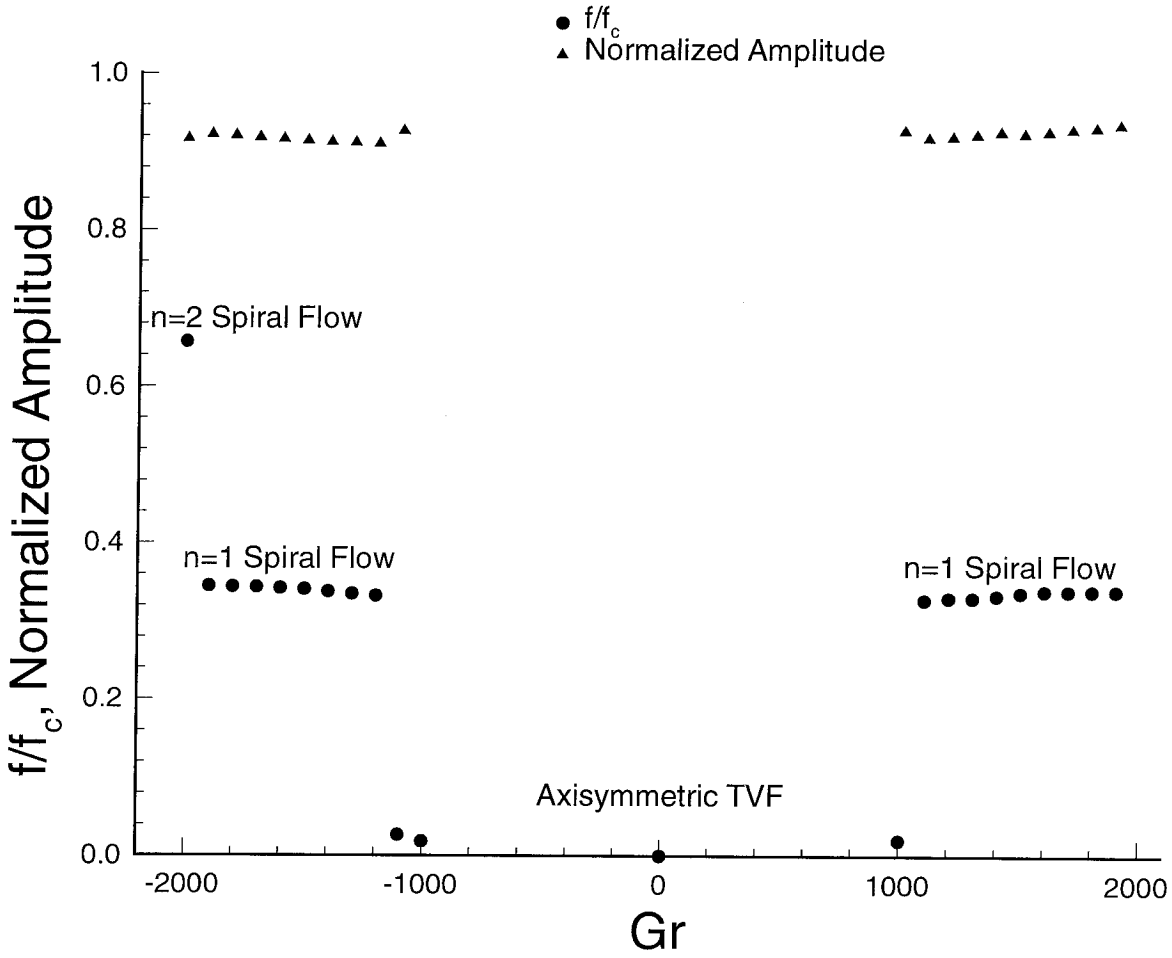

Figure 4.20: Variation of frequency and amplitude with Grashof number for η=0.6, L_z=1.994, R=100, Pr=0.7 and A=0.2888.

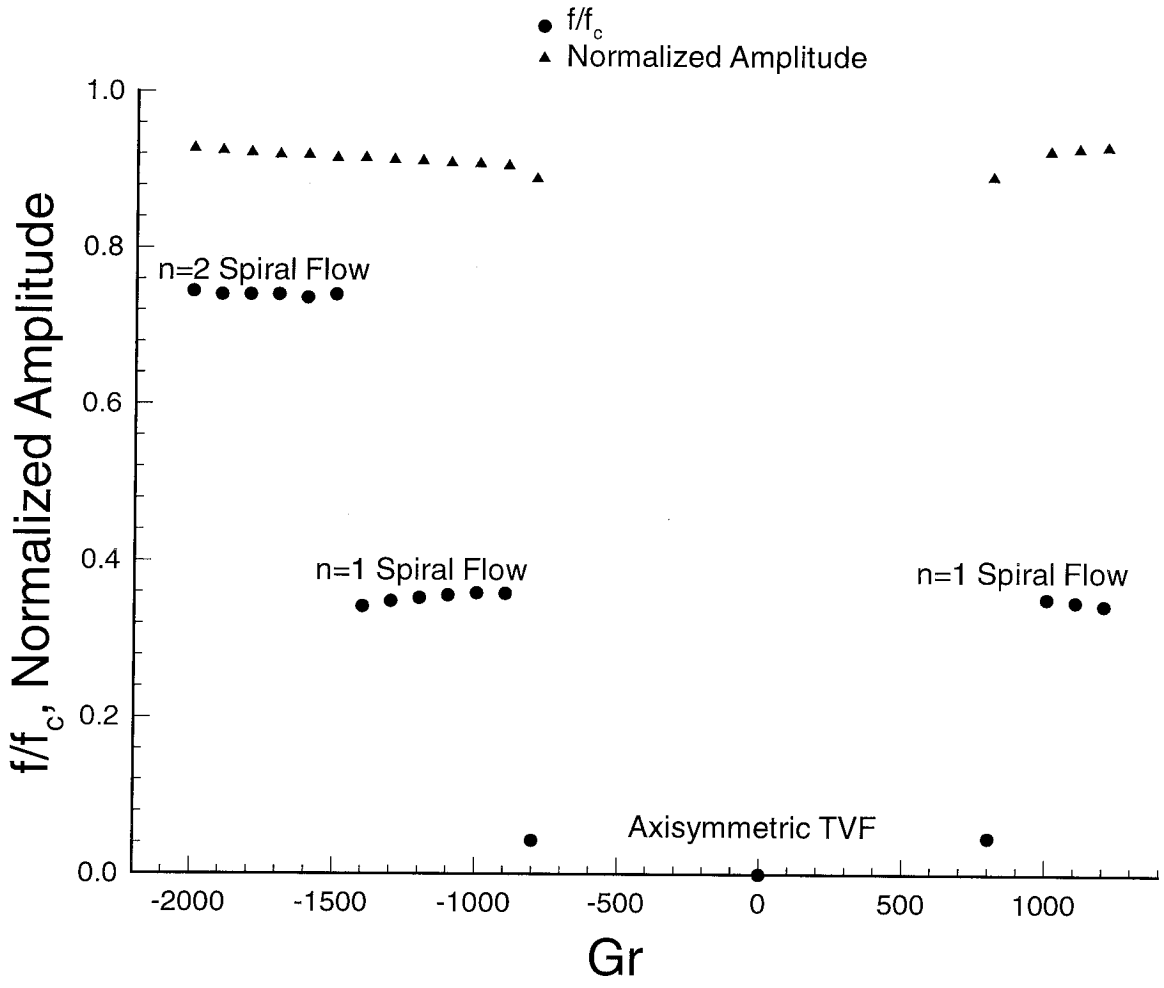

Figure 4.21: Variation of frequency and amplitude with Grashof number for η=0.7, L_z=2.001, R=100, Pr=0.7 and A=0.67.

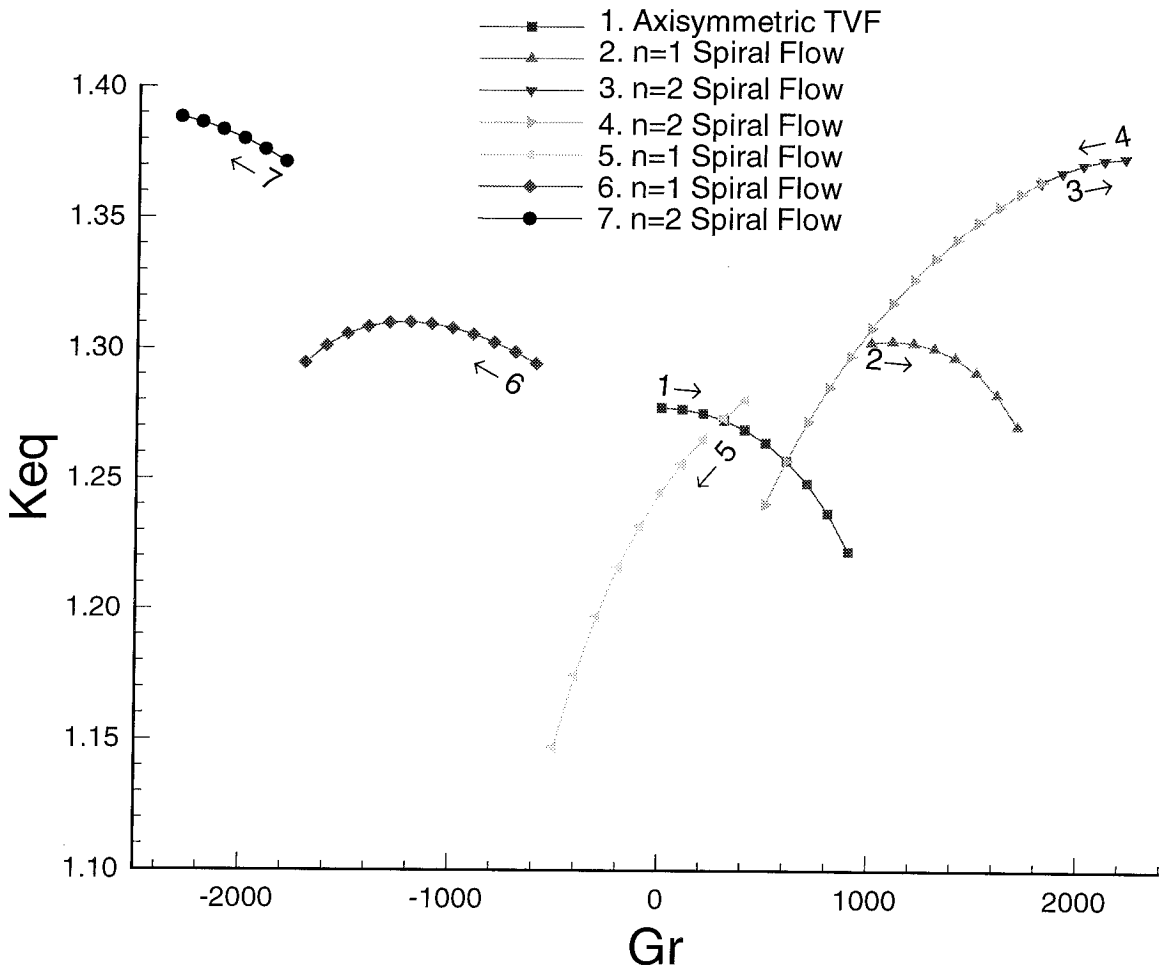

Figure 4.22: Map showing different stable states present in the flow by slowly varying the Grashof number for η=0.7, L_z=2.001, R=100 and Pr=0.7.

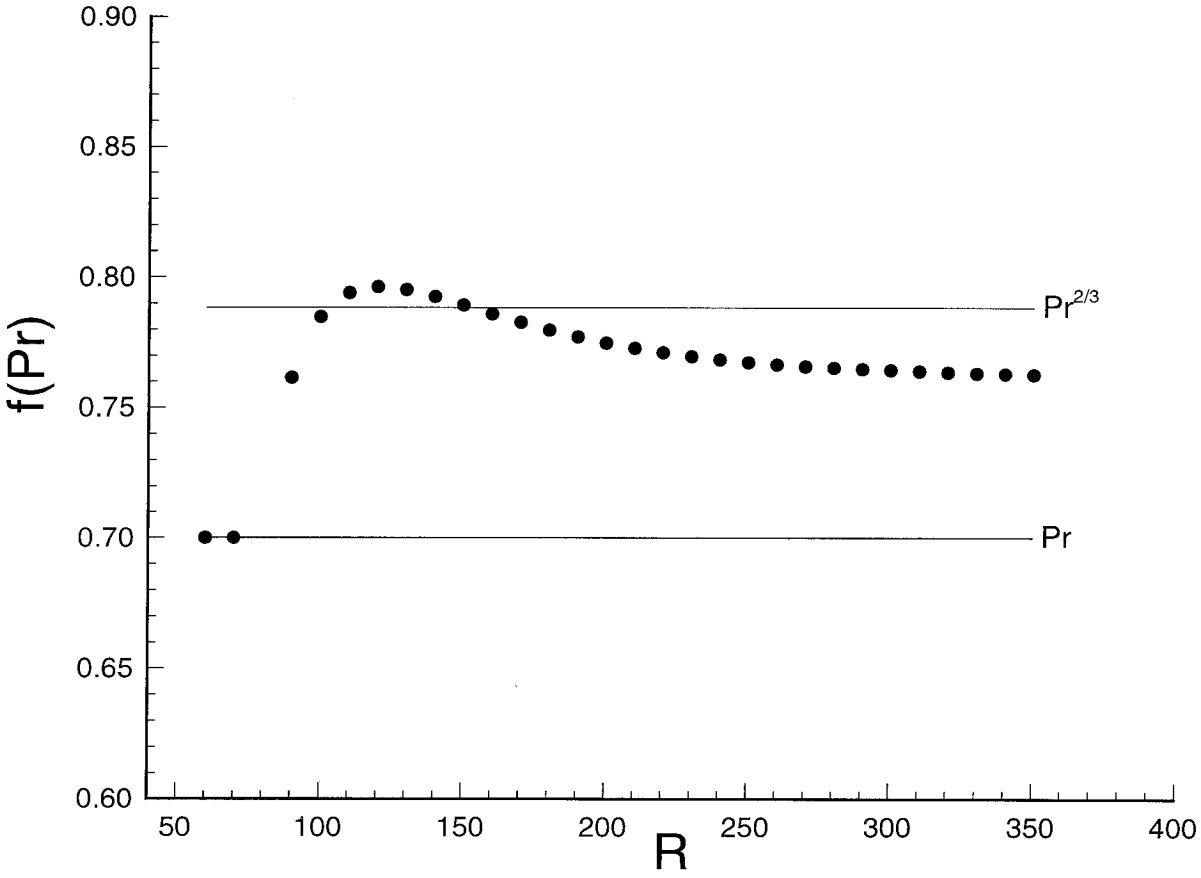

Figure 4.23: Variation of $f(Pr)$ with Reynolds number for η=0.7, L_z=2.001, Pr=0.7 and Gr=0.

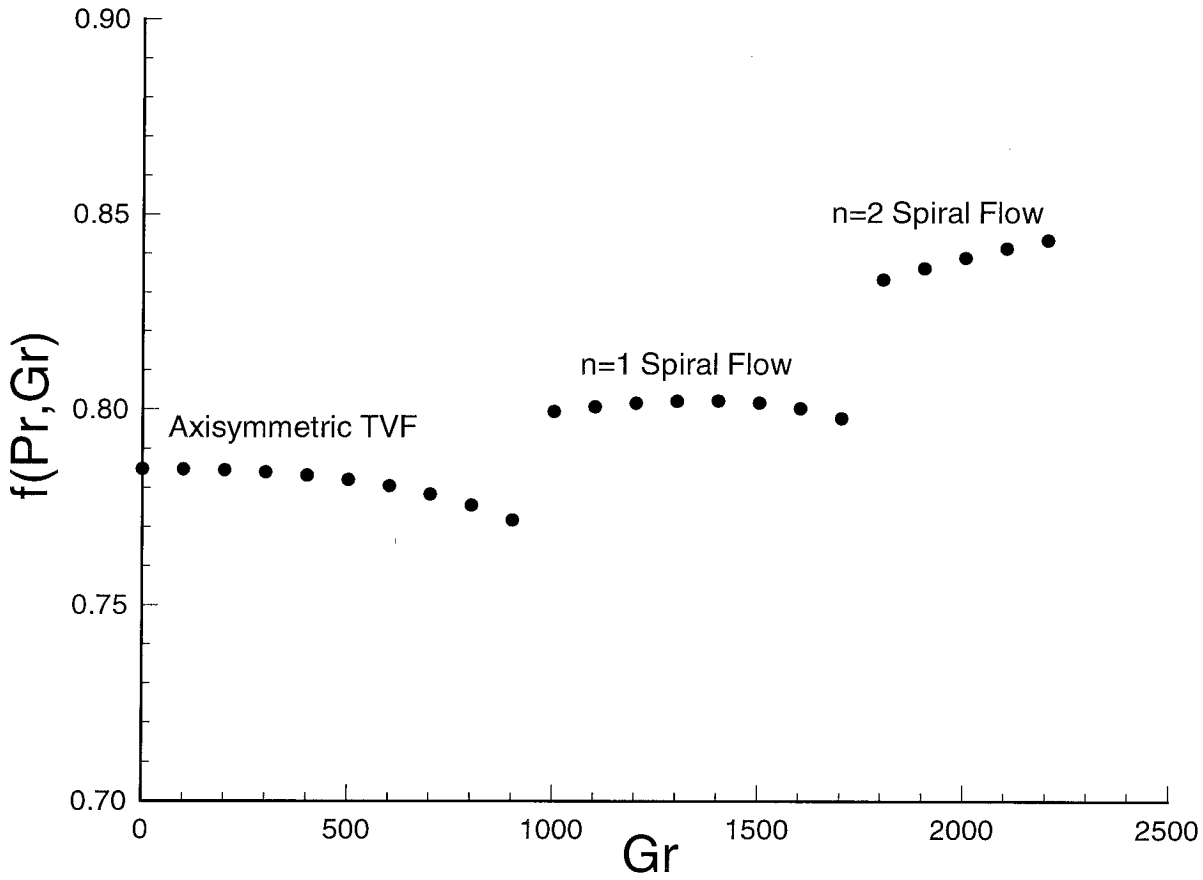

Figure 4.24: Variation of $f(Pr, Gr)$ with Grashof number for η=0.7, L_z=2.001, Pr=0.7 and R=100.

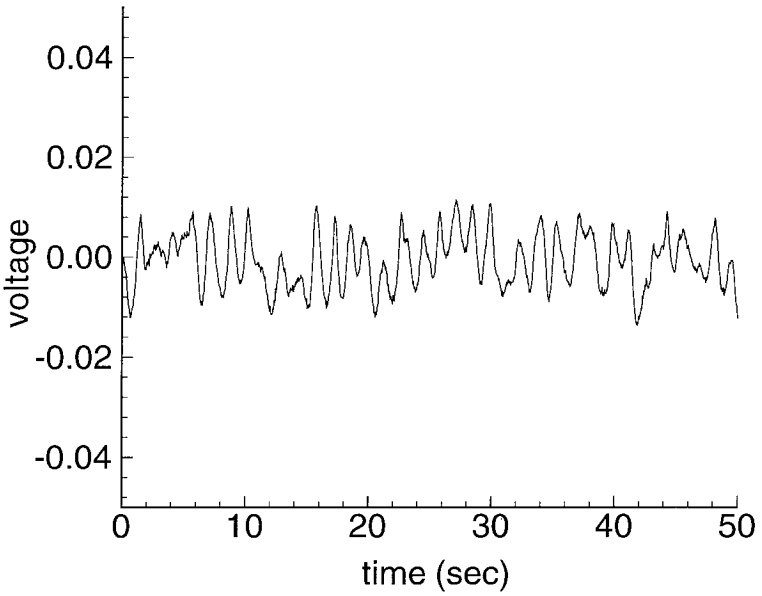

Figure 4.25: Voltage signal for R/R_c=1.6.

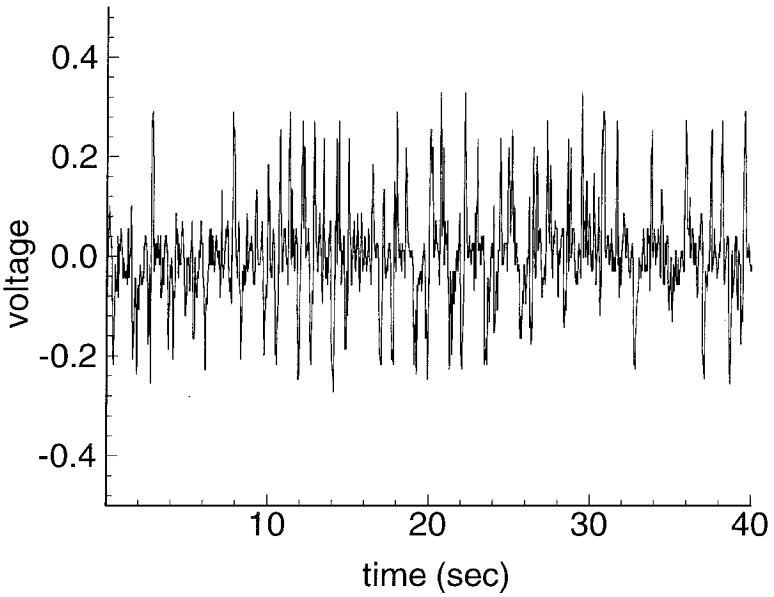

Figure 4.26: Voltage signal for R/R_c=11.1.

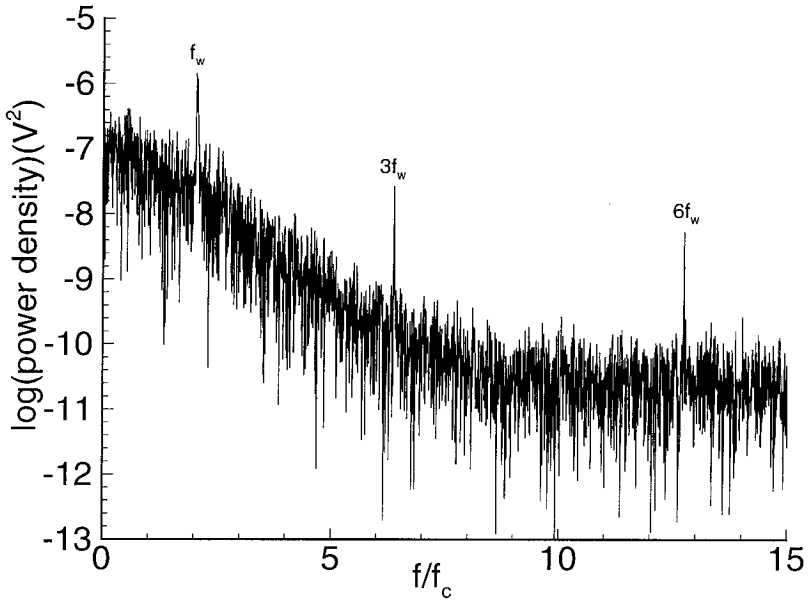

Figure 4.27: Power spectrum for R/R_c=1.6.

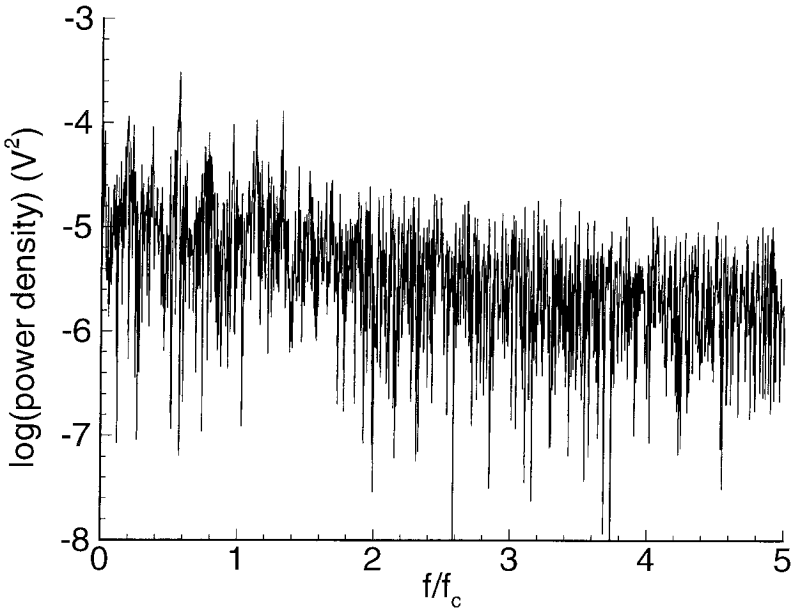

Figure 4.28: Power spectrum for R/R_c=11.1.

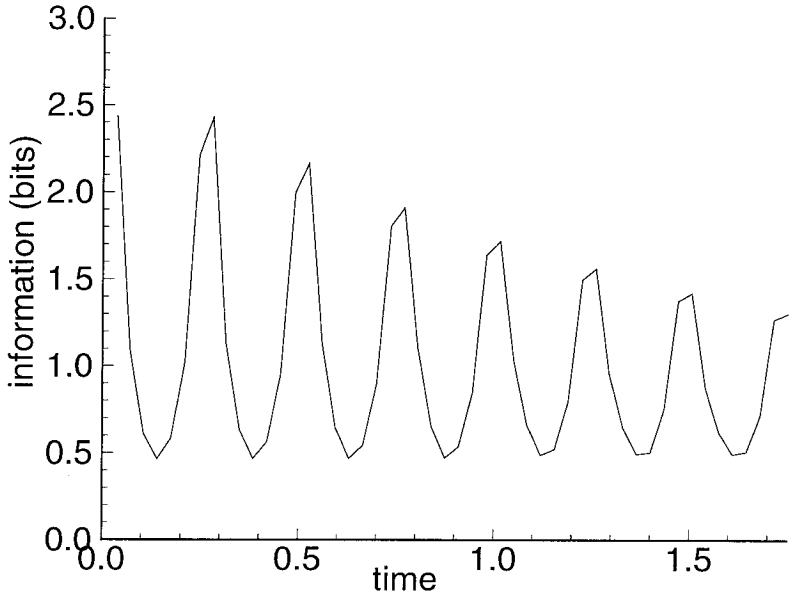

Figure 4.29: Mutual information for R/R_c=1.6.

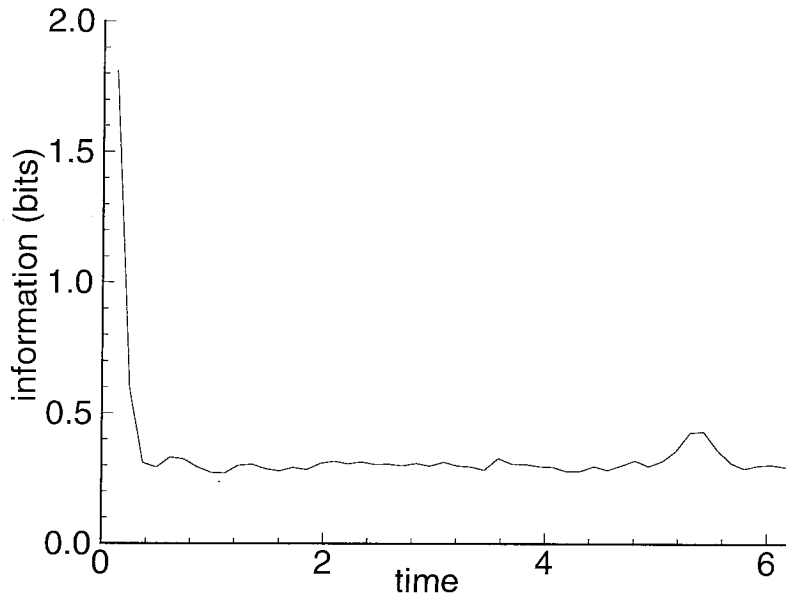

Figure 4.30: Mutual information for R/R_c=11.1.

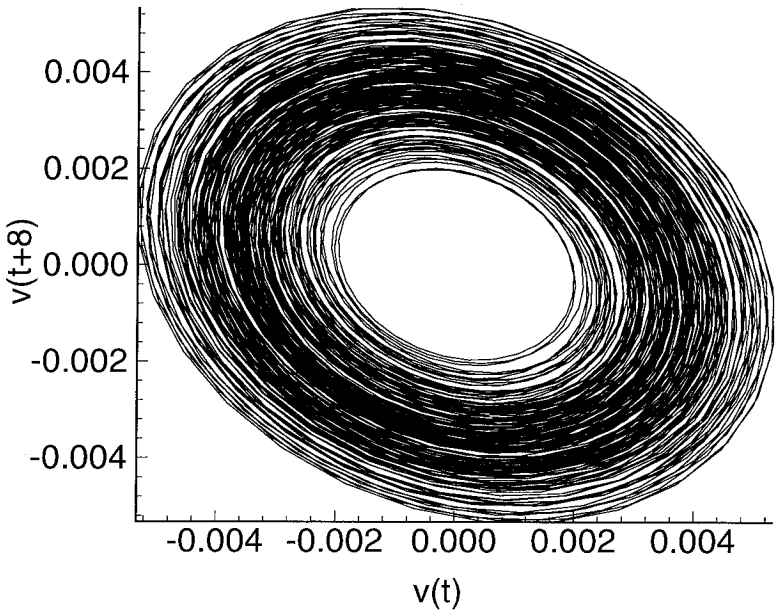

Figure 4.31: Phase plot for R/R_c=1.6.

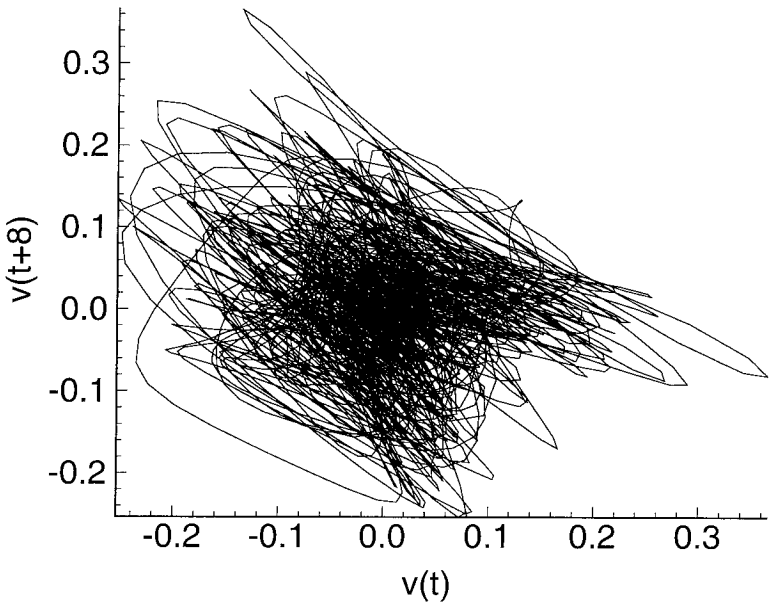

Figure 4.32: Phase plot for R/R_c=11.1.

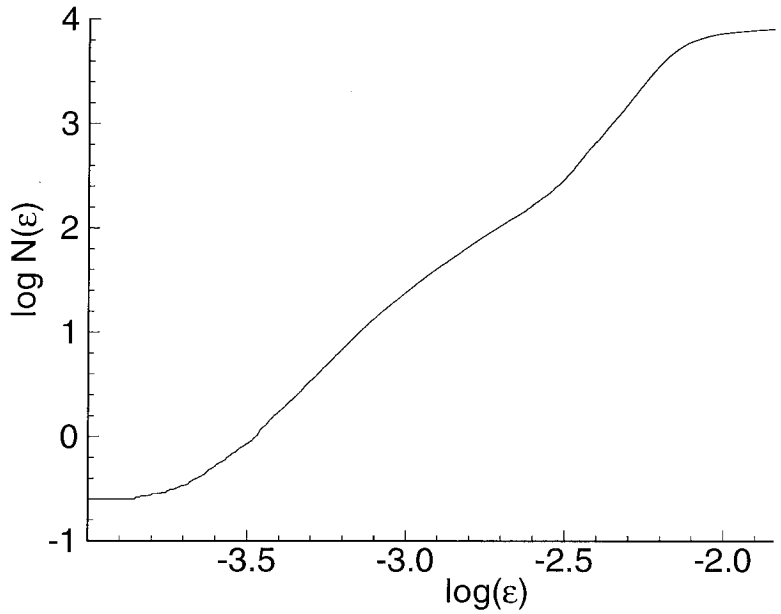

Figure 4.33: Plot of $\log N(\epsilon)$ versus $\log(\epsilon)$ for R/R_c=1.6

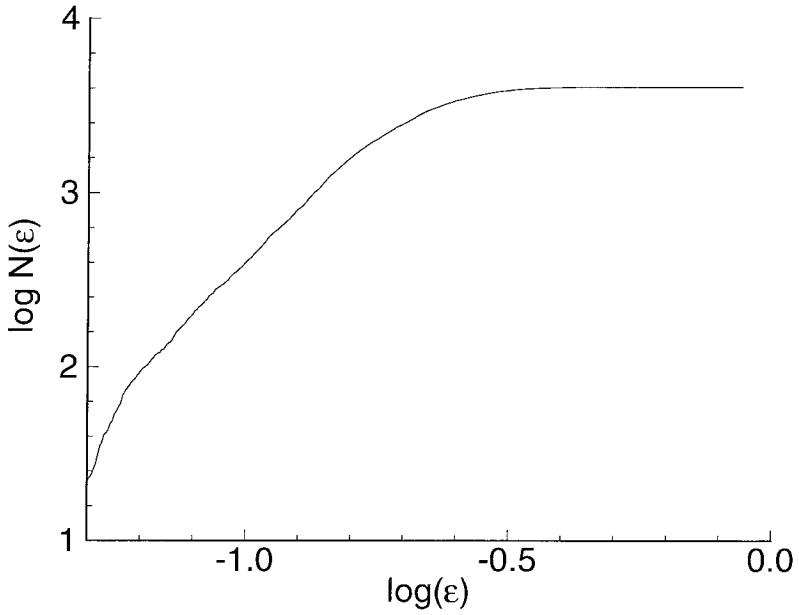

Figure 4.34: Plot of $\log N(\epsilon)$ versus $\log(\epsilon)$ for R/R_c=11.1

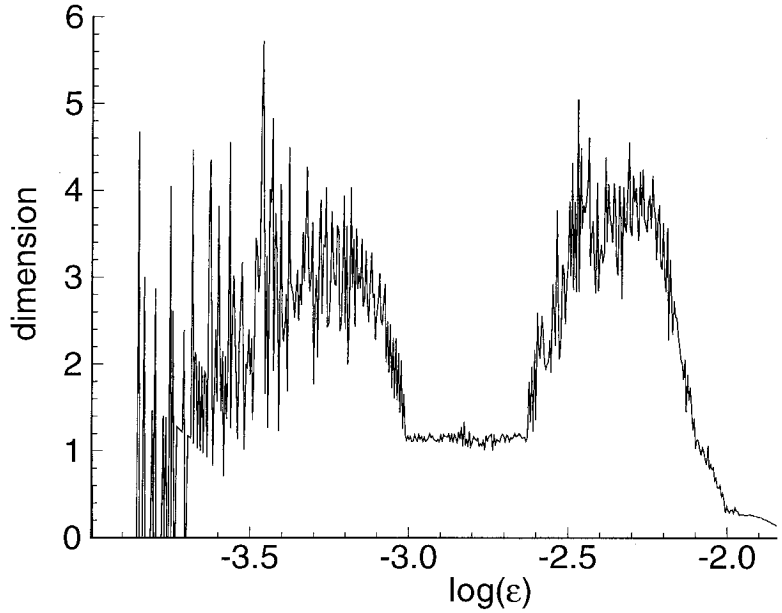

Figure 4.35: Plot of the slope for R/R_c=1.6.

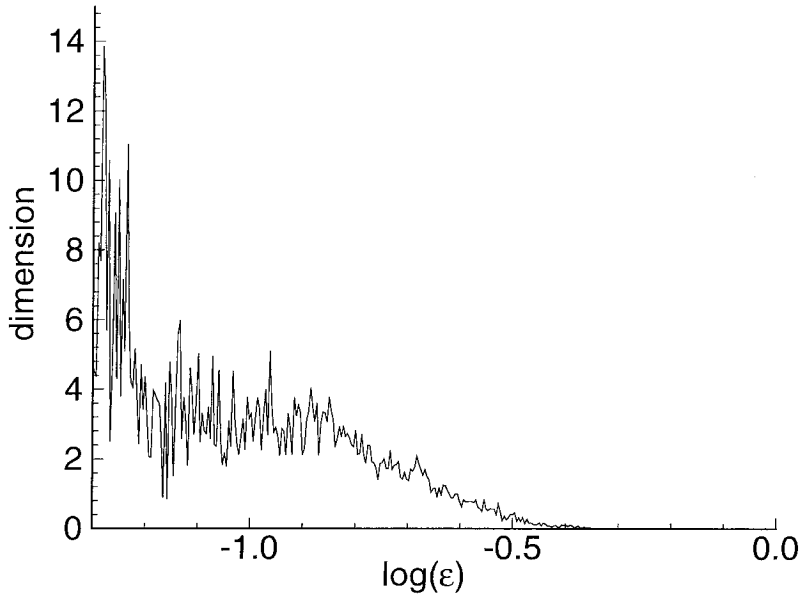

Figure 4.36: Plot of the slope for R/R_c=11.1.

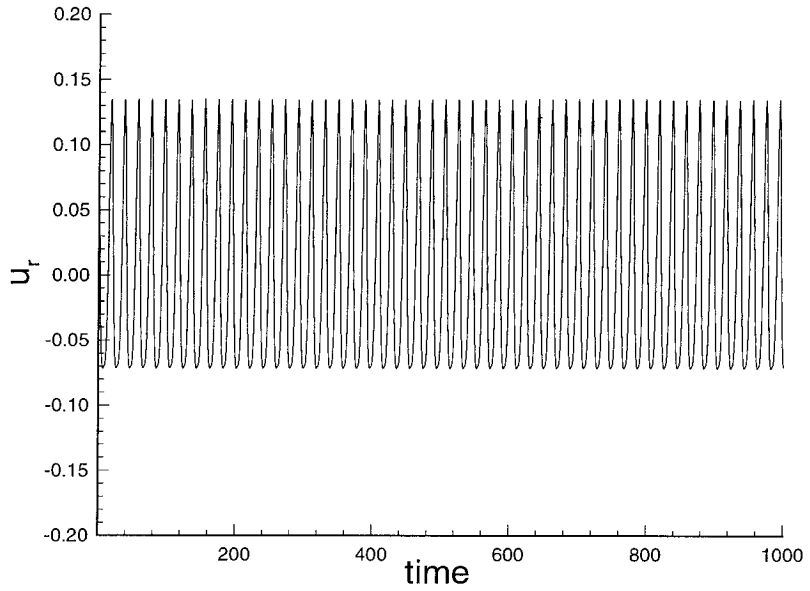

Figure 4.37: Radial velocity signal for η=0.7, L_z=2.001, R=100, Pr=0.7 and Gr=-1700.

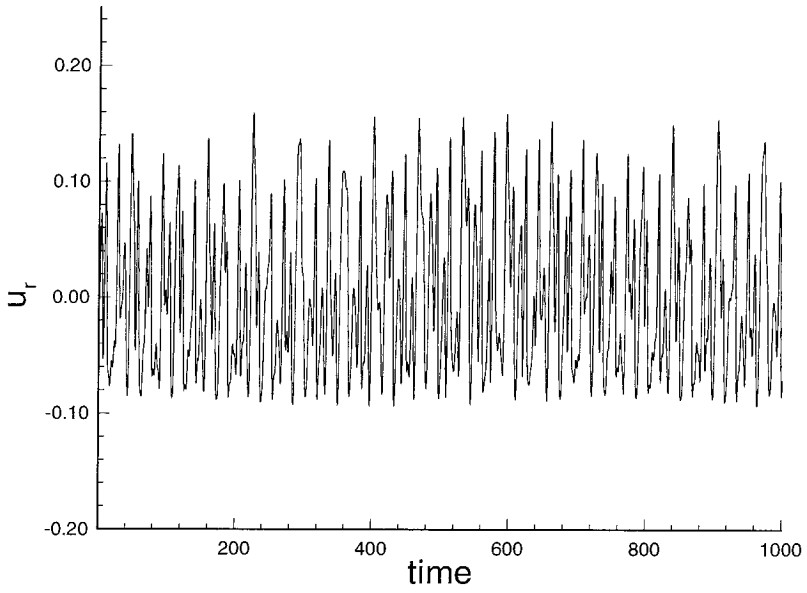

Figure 4.38: Radial velocity signal for η=0.7, L_z=2.001, R=100, Pr=0.7 and Gr=-2100.

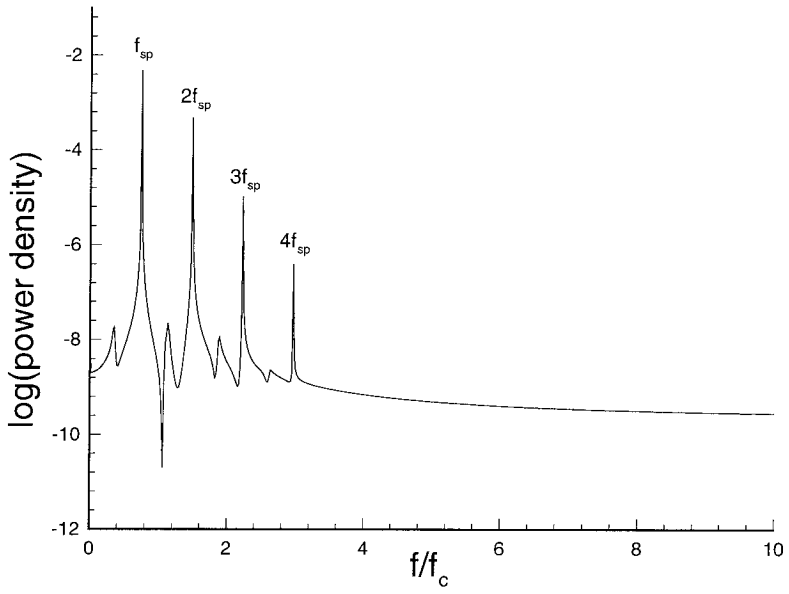

Figure 4.39: Power spectrum of the radial velocity for η=0.7, L_z=2.001, R=100, Pr=0.7 and Gr=-1700.

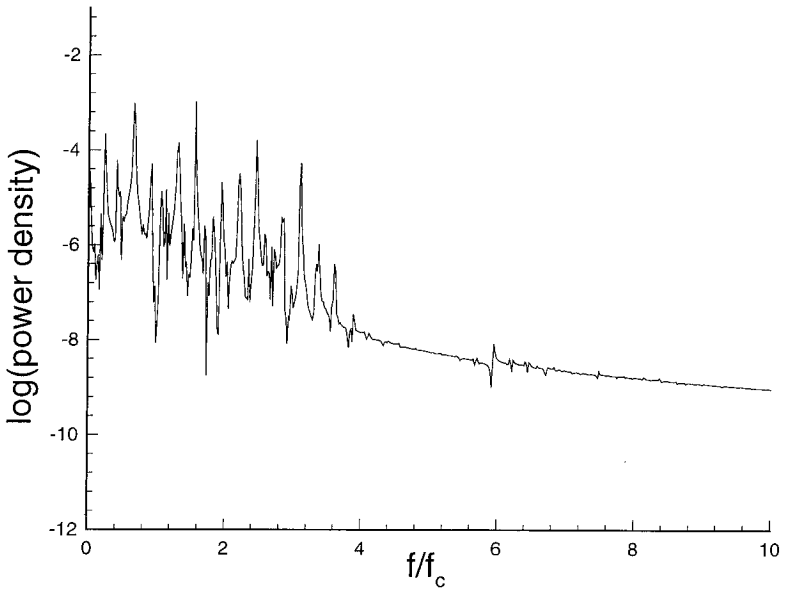

Figure 4.40: Power spectrum of the radial velocity for η=0.7, L_z=2.001, R=100, Pr=0.7 and Gr=-2100.

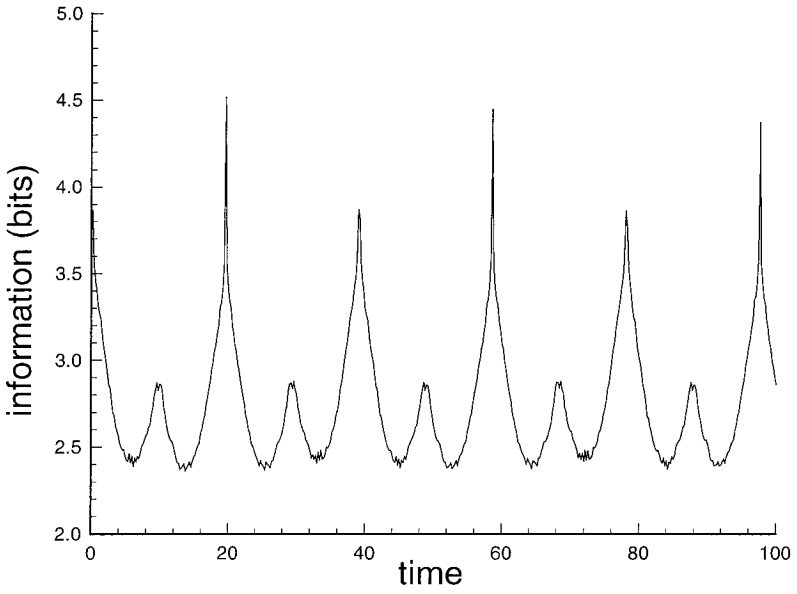

Figure 4.41: Mutual information of the radial velocity for η=0.7, L_z=2.001, R=100, Pr=0.7 and Gr=-1700.

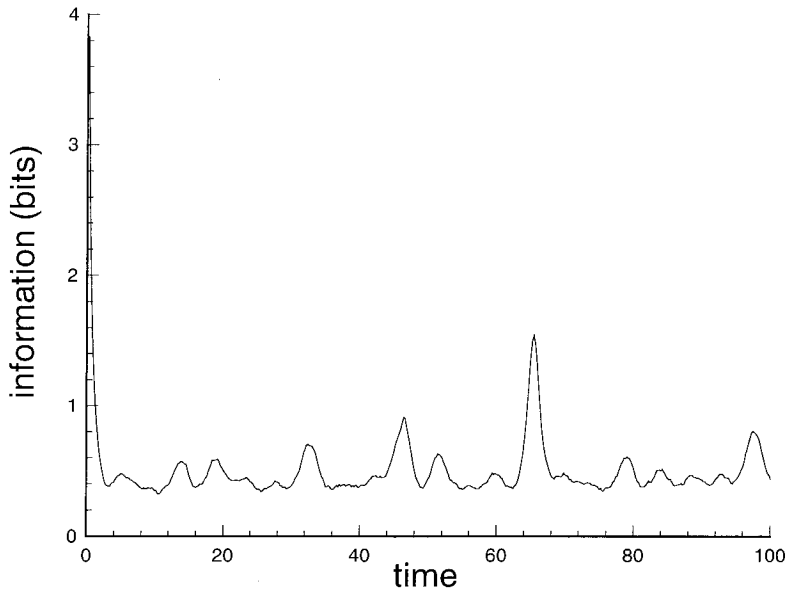

Figure 4.42: Mutual information of the radial velocity for η=0.7, L_z=2.001, R=100, Pr=0.7 and Gr=-2100.

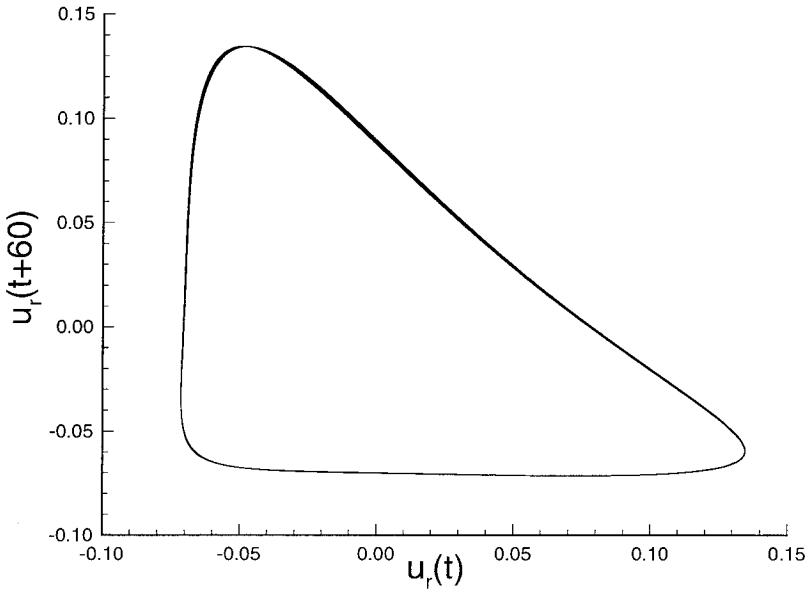

Figure 4.43: Phase plot of the radial velocity for η=0.7, L_z=2.001, R=100, Pr=0.7 and Gr=-1700.

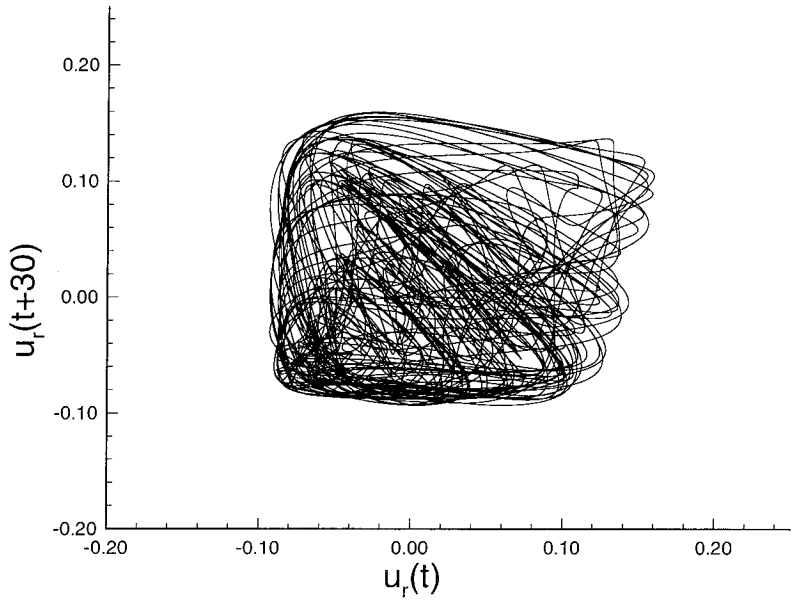

Figure 4.44: Phase plot of the radial velocity for η=0.7, L_z=2.001, R=100, Pr=0.7 and Gr=-2100.

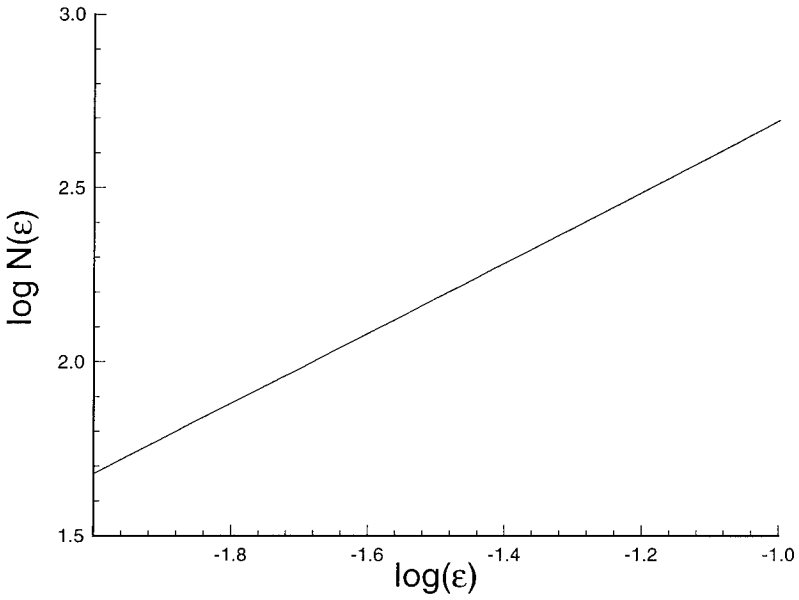

Figure 4.45: Plot of $\log N(\epsilon)$ versus $\log(\epsilon)$ from the radial velocity for η=0.7, L_z=2.001, R=100, Pr=0.7 and Gr=-1700.

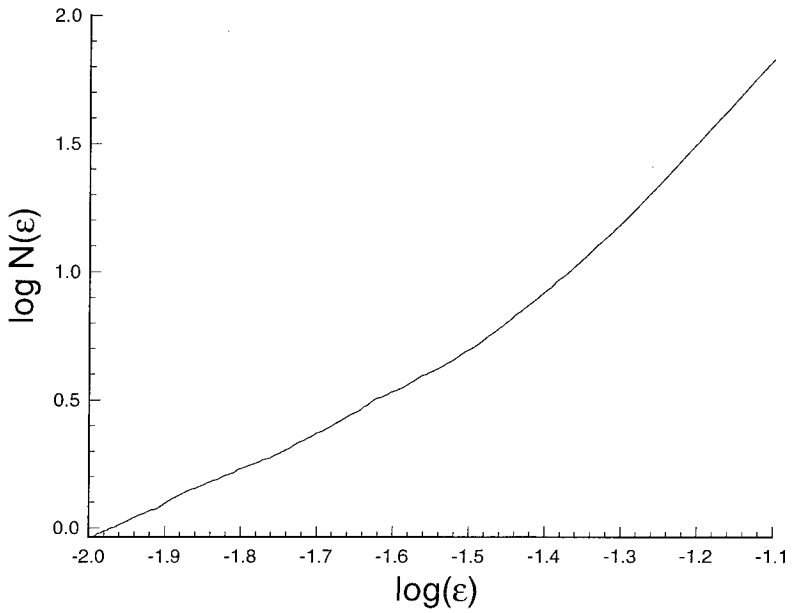

Figure 4.46: Plot of $\log N(\epsilon)$ versus $\log(\epsilon)$ from the radial velocity for η=0.7, L_z=2.001, R=100, Pr=0.7 and Gr=-2100.

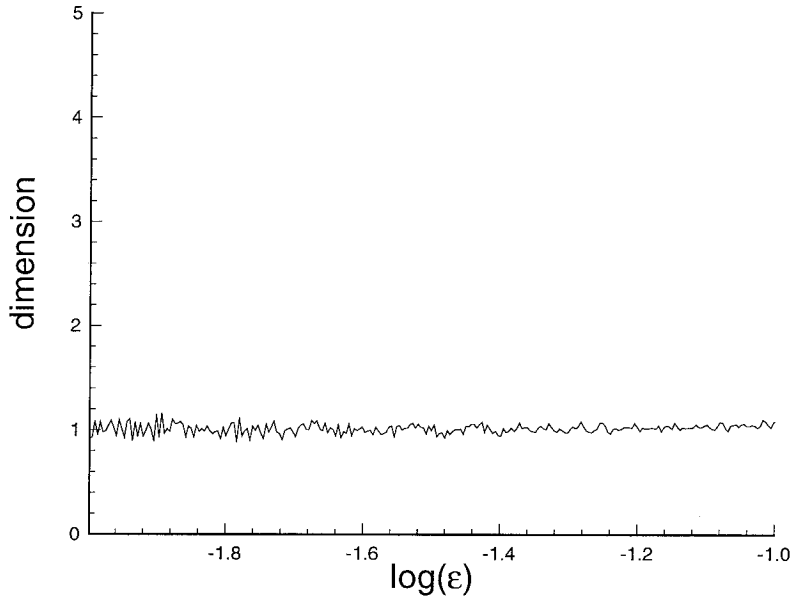

Figure 4.47: Plot of the slope from Fig. 4.45 for η=0.7, L_z=2.001, R=100, Pr=0.7 and Gr=-1700.

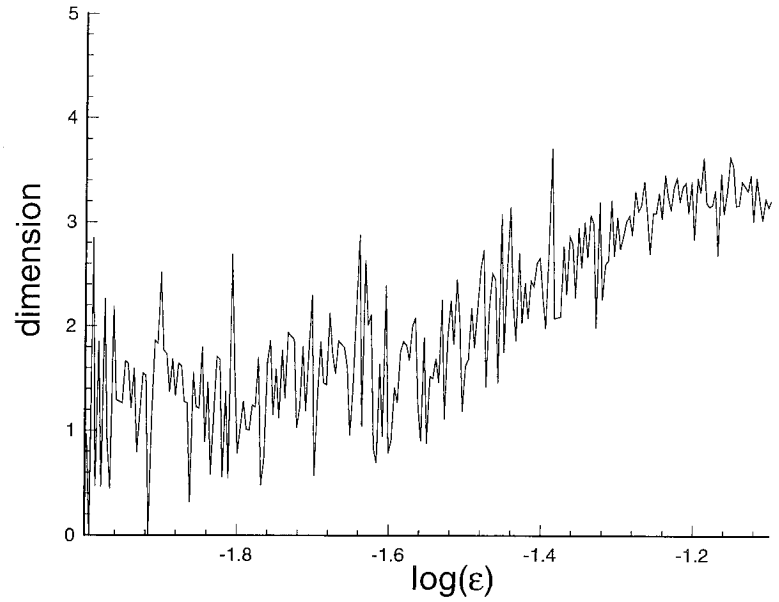

Figure 4.48: Plot of the slope from Fig. 4.46 for η=0.7, L_z=2.001, R=100, Pr=0.7 and Gr=-2100.

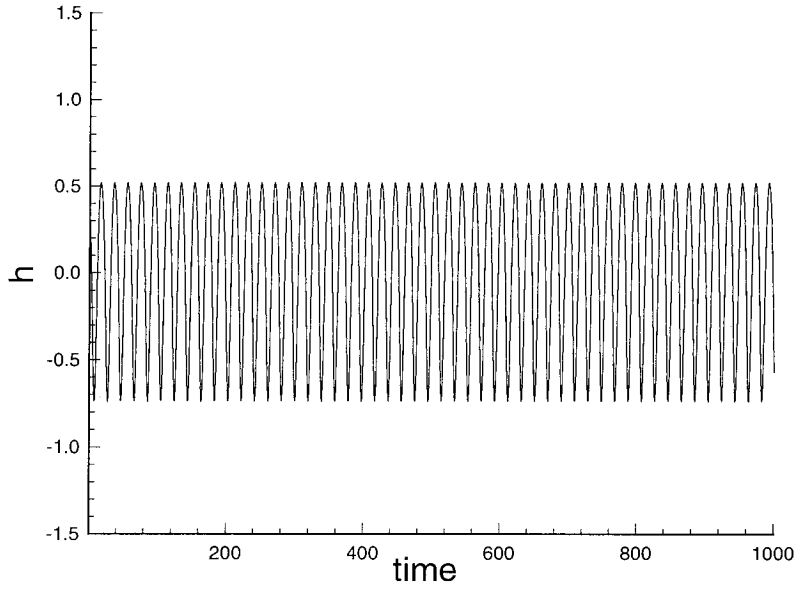

Figure 4.49: Local heat transfer coefficient signal for η=0.7, L_z=2.001, R=100, Pr=0.7 and Gr=-1700.

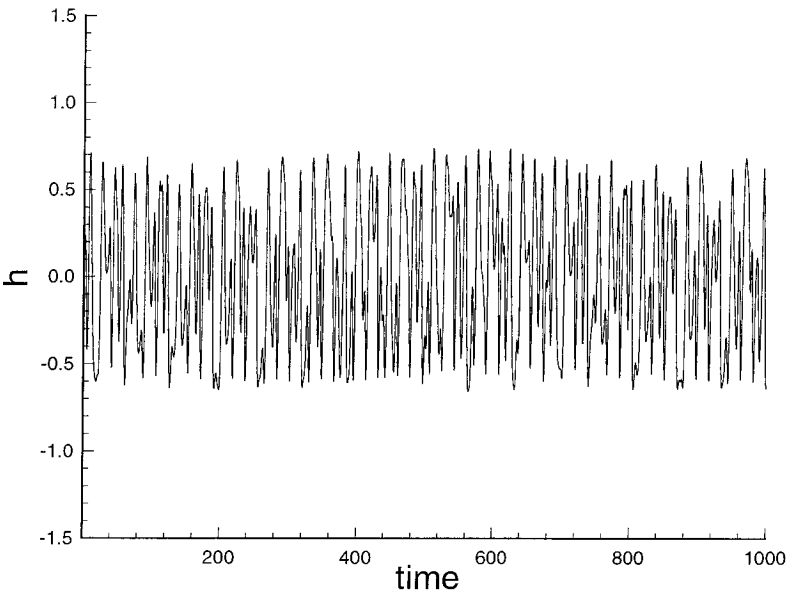

Figure 4.50: Local heat transfer coefficient signal for η=0.7, L_z=2.001, R=100, Pr=0.7 and Gr=-2100.

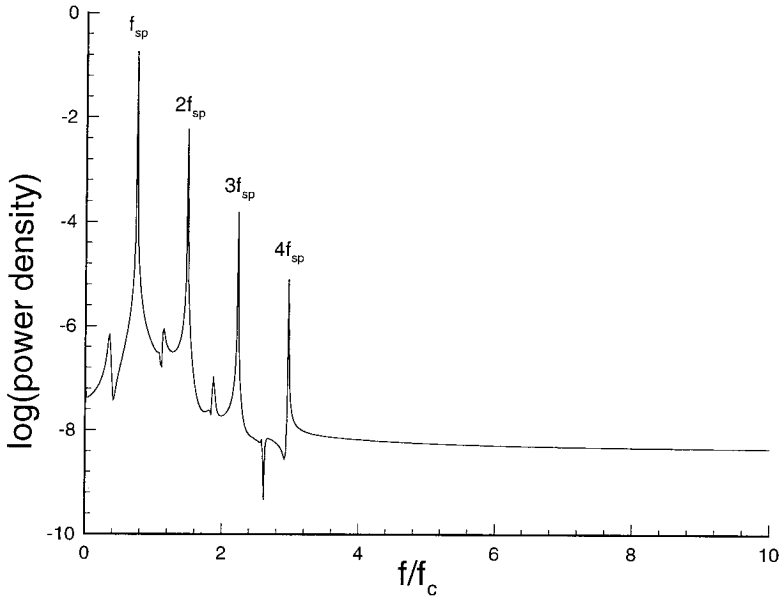

Figure 4.51: Power spectrum of the local heat transfer coefficient for η=0.7, L_z=2.001, R=100, Pr=0.7 and Gr=-1700.

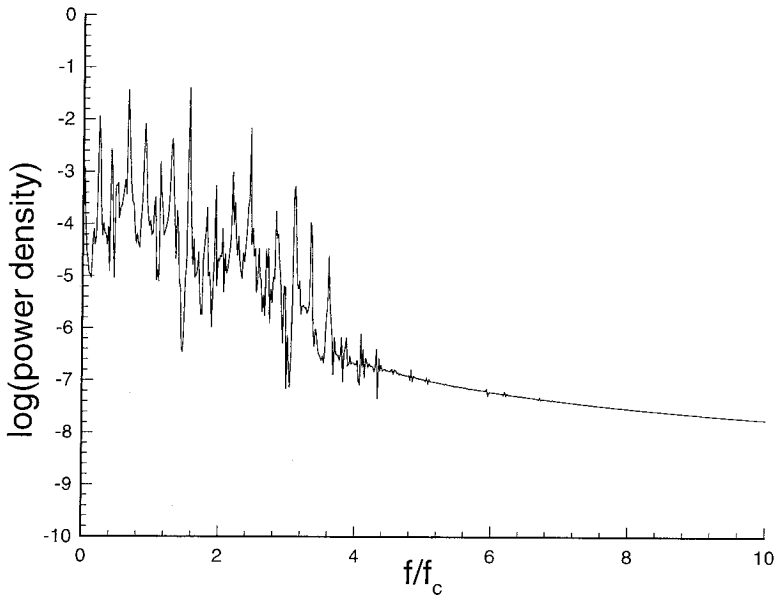

Figure 4.52: Power spectrum of the local heat transfer coefficient for η=0.7, L_z=2.001, R=100, Pr=0.7 and Gr=-2100.

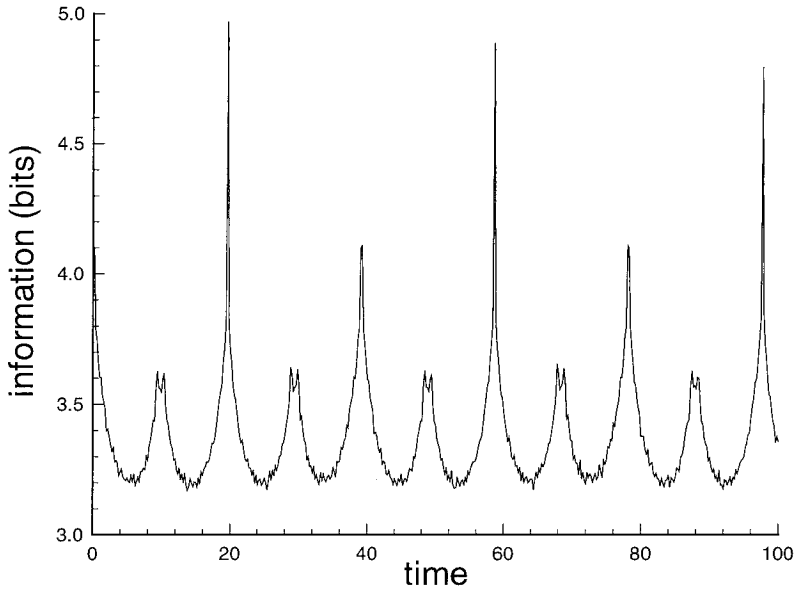

Figure 4.53: Mutual information of the local heat transfer coefficient for η=0.7, L_z=2.001, R=100, Pr=0.7 and Gr=-1700.

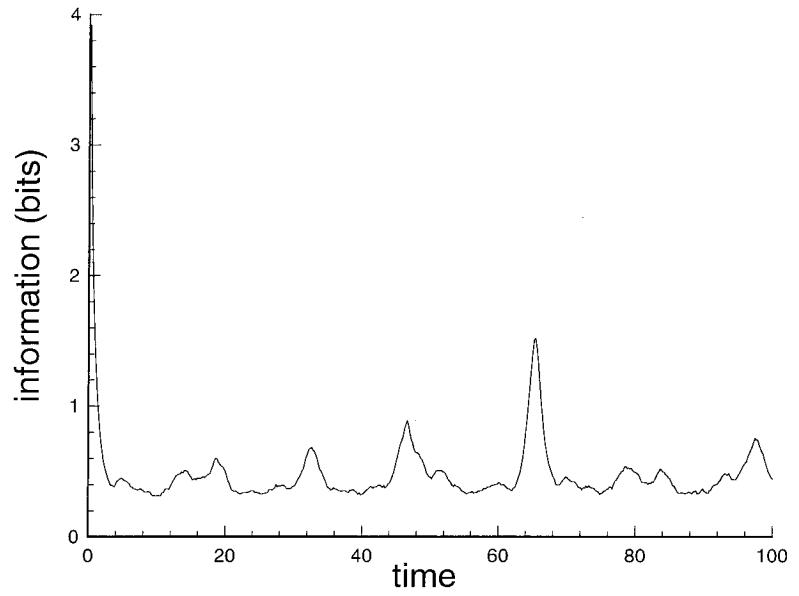

Figure 4.54: Mutual information of the local heat transfer coefficient for η=0.7, L_z=2.001, R=100, Pr=0.7 and Gr=-2100.

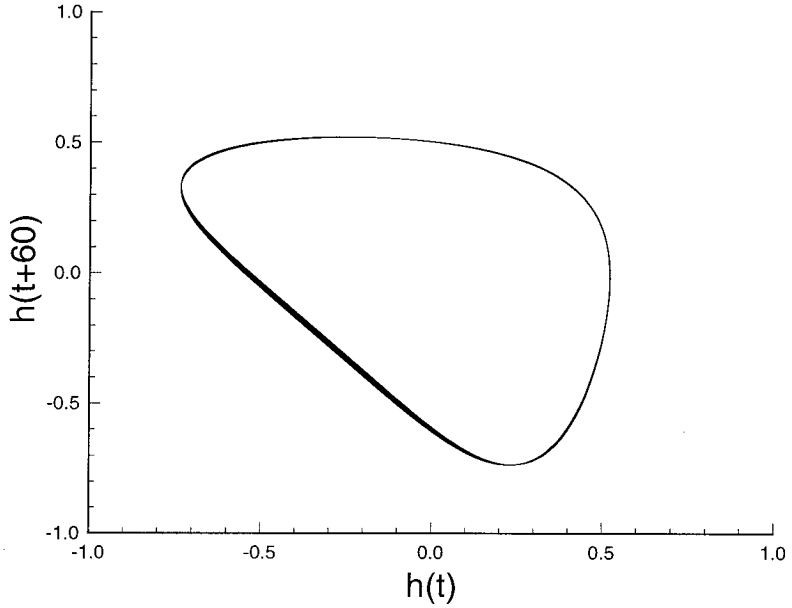

Figure 4.55: Phase plot of the local heat transfer coefficient for η=0.7, L_z=2.001, R=100, Pr=0.7 and Gr=-1700.

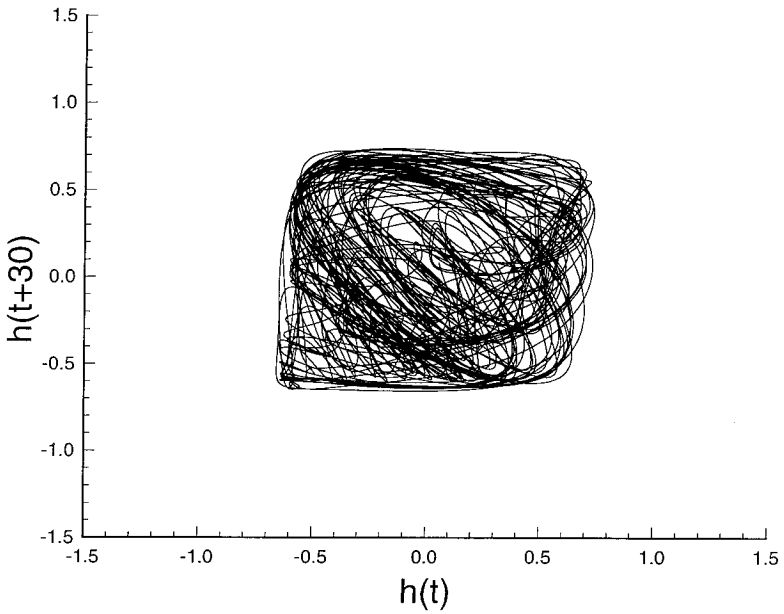

Figure 4.56: Phase plot of the local heat transfer coefficient for η=0.7, L_z=2.001, R=100, Pr=0.7 and Gr=-2100.

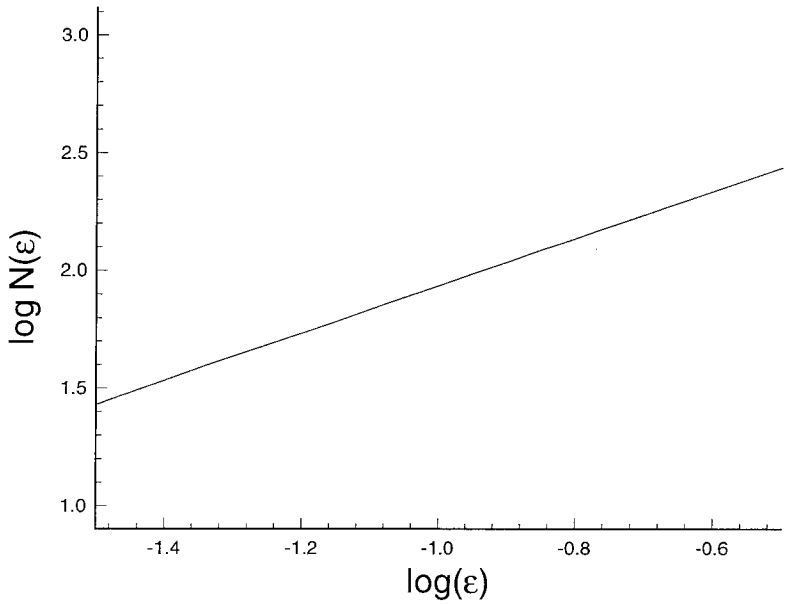

Figure 4.57: Plot of $\log N(\epsilon)$ versus $\log(\epsilon)$ from the local heat transfer coefficient for η=0.7, L_z=2.001, R=100, Pr=0.7 and Gr=-1700.

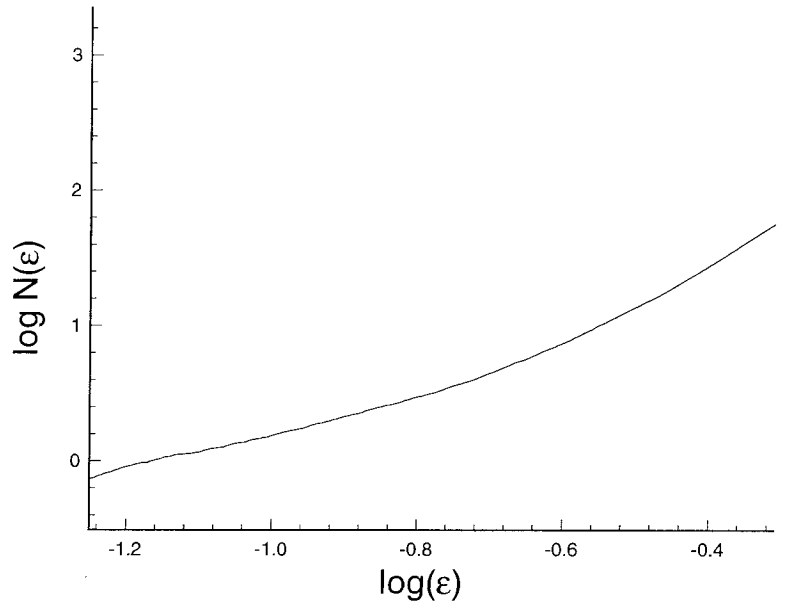

Figure 4.58: Plot of $\log N(\epsilon)$ versus $\log(\epsilon)$ from the local heat transfer coefficient for η=0.7, L_z=2.001, R=100, Pr=0.7 and Gr=-2100.

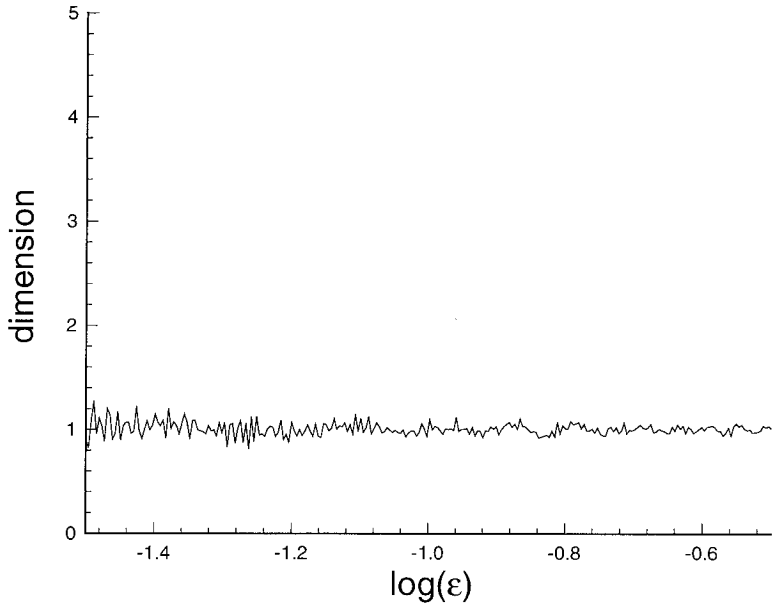

Figure 4.59: Plot of the slope from Fig. 4.57 for η=0.7, L_z=2.001, R=100, Pr=0.7 and Gr=-1700.

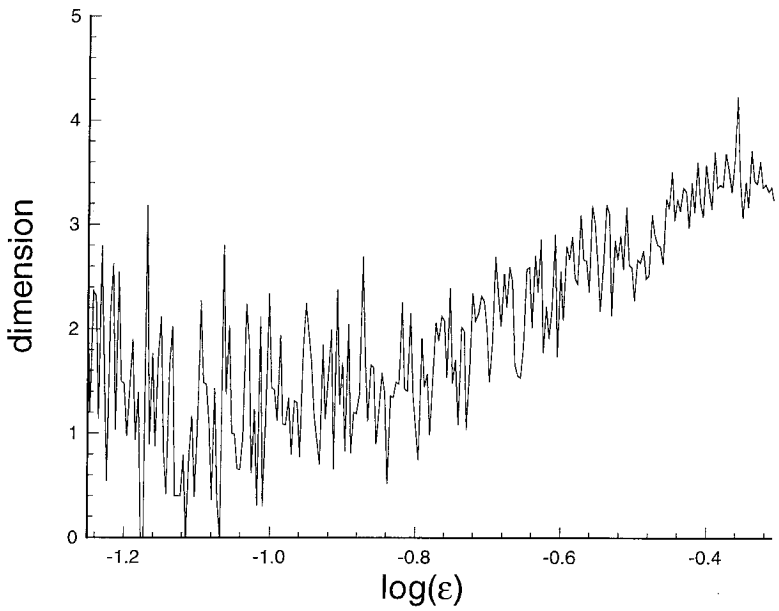

Figure 4.60: Plot of the slope from Fig. 4.58 for η=0.7, L_z=2.001, R=100, Pr=0.7 and Gr=-2100.

Chapter 5

Closure

5.1 Summary and Conclusions

Experiments and numerical simulations were performed to study the flow between two concentric cylinders. The isothermal experimental studies were conducted to investigate the dependence of the attractor dimension on the Reynolds number. The primary reason for the numerical simulations was to obtain information about the frequencies and amplitudes of the thermal environment.

Isothermal experiments were conducted to compare with previous Taylor-Couette studies for a range of Reynolds numbers. The critical Reynolds number for the onset of Taylor vortices was confirmed for η=0.89 and Γ=40. The measured axial wavelength corresponding to the critical Reynolds number was in close agreement with the value reported by other experiments and from linear stability analysis. The critical Reynolds number for the onset of wavy vortex flow, the wave number, and the wave speed also confirmed that measurements from the experiment agreed with existing literature on isothermal Taylor-Couette systems. The axial wavelengths were also measured as a function of Reynolds number by steadily increasing the rotation of the inner cylinder. The axial wavelength increased monotonically with the Reynolds

number. For R/R_c=1.6, the dimension of the attractor was found to be 1. Qualitatively, the dimension of the attractor increased with the Reynolds number but the quantitative results at higher Reynolds number were contaminated by the background noise.

Preliminary studies with a slightly heated axial flow showed that the temperature fluctuations were also contaminated by noise, especially at higher Reynolds numbers. Hence, it appeared that with the existing facility using air, experimental measurements of the transitions at higher Reynolds numbers and with a radial temperature gradient would not be feasible. Because of these reasons, the heat transfer experiment was abandoned. In its place, direct numerical simulations were performed to study the effects of the gravitational and centrifugal potentials on the stability of heated, incompressible Taylor-Couette flow. Both the aforementioned effects have not been considered together in previous numerical simulations. The three-dimensional equations were discretized using a Chebyshev/Fourier spectral method. Critical Reynolds number and wave speed agreed well with linear stability theory. The study concentrated on the radius ratio, the Reynolds number, and the Grashof number parameter space. The systematic investigation included heat transfer characteristics, maps of different stable states, hysteresis, validation of Colburn's empirical formula, and a time delay analysis of the numerical time series of the radial velocity component and the local heat transfer coefficient.

First, a study was performed to investigate the local variation of heat transfer on the stationary outer cylinder. The variation was found to be sinusoidal. The magnitude of the heat transfer was in agreement with the mass transfer experiments of Kataoka, et al. (1977), with 0.375 as the exponent of the Prandtl number. The Nusselt number slightly increased for higher Prandtl number (Pr=5). The mean equivalent conductivity was also calculated as a function of the Reynolds number.

The results showed a power law behavior, which had a lower coefficient and a higher exponent than the experimental results of Ball, et al. (1989). The counter-rotating Taylor cells were found to be of unequal size for the case of radial heating. Also, the heat transfer results were found to be sensitive to the imposed axial wavelength. A similar axial wavelength dependence on the torque was also observed by Meyer (1967). Maps showing different stable states present in the flow were also constructed for η=0.5, 0.6 and 0.7. Higher mode spirals formed for negative Grashof numbers as the value of A increased. In the axisymmetric Taylor vortex flow regime, higher radial heating decreased the heat transfer coefficient. The formation of stripes were marked by a significant increase in the heat transfer coefficients. The flow became aperiodic for higher Grashof numbers. The plots of the local variation of the Nusselt number as a function of z and θ were also presented. For spiral flows, the heat transfer became sinusoidal in both z and θ and varied in a complicated way for aperiodic flow. The validity of Colburn's correlation was also investigated. The function $f(Pr)$ was found to be slightly lower than $Pr^{\frac{2}{3}}$ (Note that the exponent is 0.77, which is higher than $\frac{2}{3}$) for the range of Reynolds number numerically investigated.

The frequencies and the amplitudes of local fluctuations of heat transfer coefficient were also presented for the three radius ratios (η=0.5, 0.6 and 0.7). The frequencies for n=1 spiral flow were found to be 0.35 times the frequency of the rotating inner cylinder and the amplitude of local fluctuations of heat transfer coefficient was about 95% of the mean. The thermal environment present in the flow could be the cause for thermal stress fatigue in pumps in BWR power plants.

The frequency power spectrum for n=2 spiral flow showed the single fundamental frequency and its harmonics for Gr=-1700. For Gr=-2100, new frequencies appeared in the power spectrum. The power spectrum became broad-banded for even lower Grashof numbers. The two dimensional projection of the reconstructed attractor

showed a limit cycle for Gr=-1700. The limit cycle behavior disappeared at Gr=-2100 and the reconstructed attractor became irregular. The pointwise dimension calculation gave a value of approximately 1 for Gr=-1700. The dimension value increased to about 3.2 for Gr=-2100 and the constant dimension region was found to be small.

One of the interesting properties of the nonlinear Navier-Stokes equations is non-uniqueness. With all other parameters fixed, the Grashof number was slowly varied to examine the existence of a hysteresis loop in heated Taylor-Couette flow. It was found that two stable states existed for the same Grashof number. One state was reached by increasing the Grashof number and the other by slowly decreasing it.

5.2 Directions for Future Research

This research could be extended to study the effects of various geometric parameters on the dimension calculations. The two geometric parameters are the radius ratio and the aspect ratio. The aspect ratio study can show the effect of the change of volume on the number of degrees of freedom of the physical system. Similarly, the study of the effect of different radius ratios would reveal the importance of the concentric cylinders in either maintaining order or increasing the dimension. Both of these studies need a very flexible experimental facility. The effect of a radial temperature gradient on the attractor dimension could be another interesting research area. Experimentally, the inner cylinder could be heated with a cartridge heater and the outer cylinder cooled with a cold water jacket. The negative temperature gradient would stabilize the flow. The study can show the effect of local change in the energy of the system on its dimension. Yet another study which would be of great importance is the correlation between the various vortices in the flow (Dr. M. Gorman, private communication).

If the vortices were well correlated, then the attractor dimension at a single point would give the true dimension of the entire physical system. If the flow were not correlated, then the estimated dimension would not represent the entire flow. Hence, a single point measurement would only give a partial dimension and the degrees of freedom of the physical system would be given by the sum of these partial dimensions.

References

Abarbanel, H.D.I., 1996, Analysis of observed chaotic data, Springer-Verlag, New York.

Ali, M. and Weidman, P.D., 1990, "On the stability of circular Couette flow with radial heating," J. Fluid Mech., Vol. 220, pp. 53-84.

Alziary De Roquefort, T. and Grillaud, G., 1978, "Computation of Taylor vortex flow by a transient implicit method," Comput. Fluids, Vol. 6, pp. 259-269.

Ball, K.S. and Farouk, B., 1987, "On the development of Taylor vortices in a vertical annulus with a heated rotating inner cylinder," Int. J. Num. Meth. Fluids, Vol. 7, pp. 857-867.

Ball, K.S. and Farouk, B., 1988, "Bifurcation phenomena in Taylor-Couette flow with buoyancy effects," J. Fluid Mech., Vol. 197, pp. 479-501.

Ball, K.S., Farouk, B., and Dixit, V.C., 1989, "An experimental study of heat transfer in a vertical annulus with a rotating inner cylinder," Int. J. Heat Mass Transfer, Vol. 32, No. 8, pp. 1517-1527.

Becker, K.M., and Kaye, J., 1962, "The influence of a radial temperature gradient on the instability of fluid flow in an annulus with an inner rotating cylinder," Trans. ASME, Journal of H.T., Vol. 80, pp. 106-110.

Bjorklund, I.S., and Kays, W.M., 1959, "Heat transfer between concentric rotating cylinders," Journal of H.T., August, pp. 175-186.

Brandstater, A. and Swinney, H.L., 1987, "Strange attractors in weakly turbulent

Couette-Taylor flow," Phys. Rev. A, Vol. 35, No. 5, pp. 2207-2220.

Burkhalter, J.E. and Koschmieder, E.L., 1973, "Steady supercritical Taylor vortex flow," J. Fluid Mech., Vol. 58, Part 3, pp. 547-560.

Buzug, Th. and Pfister, G., 1992,"Optimal delay time and embedding dimension for delay-time coordinates by analysis of the global static and local dynamical behavior of strange attractors," Phys. Rev. A, Vol. 45, No. 10, pp. 7073-7084.

Buzug, Th. and Pfister, G., 1992,"Comparison of algorithms calculating optimal embedding parameters for delay time coordinates," Physica D, Vol. 58, pp. 127-137.

Buzug, Th., Stamm, J. von., and Pfister, G., 1992,"Fractal dimensions of strange attractors obtained from the Taylor-Couette experiment," Physica A, Vol. 191, pp. 559-563.

Buzug, Th., Pawelzik, K., Stamm, J. von., and Pfister, G., 1994,"Mutual information and global strange attractors in Taylor-Couette flow," Physica D, Vol. 72, pp. 343-350.

Canuto, C., Hussaini, M.Y., Quarteroni, A., and Zang, T.A., 1988, Spectral methods in fluid dynamics, 3rd edn. Springer-Verlag, Berlin.

Chen, J. and Kuo, J., 1990, "The linear stability of steady circular Couette flow with a small radial temperature gradient," Phys. Fluids A, Vol. 2(9), pp. 1585-1591.

Choi, I.G., and Korpela, S.A., 1980, "Stability of the conduction regime of natural convection in a tall vertical annulus," J. Fluid Mech., Vol. 99, part 4, pp. 725-738.

Cole, J.A., 1967, "Taylor vortices with eccentric rotating cylinders," Nature 216, pp. 1200-1202.

Cole, J.A., 1969, "Taylor vortices with eccentric rotating cylinders," Nature 221, pp. 253-254.

Coles, D., 1965, "Transition in circular Couette flow," J. Fluid Mech., Vol. 21, pp. 385-425.

Constantin, P., Foias, C., Manley, O.P., and Temam, R., 1985, "Determining modes and fractal dimension of turbulent flows," J. Fluid Mech., Vol. 150, pp. 427-440.

Coughlin, K.T., and Marcus, P.S., 1992b, "Modulated waves in Taylor-Couette flow. Part 2. Numerical simulation," J. Fluid Mech., Vol. 234, pp. 19-46.

DiPrima, R.C., and Swinney, H.L., 1981, "Instabilities and transition in flow between concentric rotating cylinders ," Hydrodynamic Instabilities and the Transition to Turbulence (eds. Swinney, H.L. and Gollub, J.P), Springer-Verlag, Berlin, pp. 139-180.

Donnelly, R.J., and Simon, N.J., 1960, "An emperical torque relation for supercritical flow between rotating cylinders," J. Fluid Mech., Vol. 7, pp. 401-418.

Edwards, W.S., Beane, S.R., and Varma, S., 1991, "Onset of wavy vortices in the finite-length Couette-Taylor problem," Phys. Fluids A, Vol. 3, pp. 1510-1518.

Farmer, J. Doyne, Ott, E., and Yorke, J.A., 1983,"The dimension of chaotic attractors," Physica 7D, pp. 153-180.

Fenstermacher, P.R., Swinney, H.L., and Gollub, J.P., 1979, "Dynamical instabilities and the transition to chaotic Taylor vortex flow," J. Fluid Mech., Vol. 94, Part 1, pp. 103-128.

Fraser, A.M., and Swinney, H.L., 1986, "Independent coordinates for strange attractors from mutual information," Physical Review A, Vol. 33, No. 2, pp. 1134-1140.

Gardiner, S.R.M. and Sabersky, R.H., 1978, "Heat transfer in an annular gap," Int. J. Heat Mass Transfer, Vol. 21, pp. 1459-1466.

Gopalakrishnan, S., Vaghasia, G.K., and Reimers, C.R., 1992, "Crack propagation in main coolant pumps," presented at Fifth Int. Workshop on Main Coolant Pumps.

Gorman, M. and Swinney, H.L., 1982, "Spatial and temporal characteristics of modulated waves in the circular Couette system," J. Fluid Mech., Vol. 117, pp.

123-142.

Gray, D.D., and Giorgini, A., 1976, "The validity of the Boussinesq approximation for liquids and gases," Int. J. Heat Mass Transfer, Vol. 19, pp. 545-551.

Greenspan, H.P., 1968, The theory of rotating fluids, Cambridge University Press, New York.

Jones, C.A., 1981, "Nonlinear Taylor vortices and their stability," J. Fluid Mech., Vol. 102, pp. 249-261.

Kataoka, K., Doi, H., and Komai, T., 1977, "Heat/Mass transfer in Taylor vortex flow with constant axial flow rates," Int. J. Heat Mass Transfer, Vol. 20, pp. 57-63.

Kato, H., Kanno, H., Hosokawa, M., Watanabe, A., Shitara, C., Ashizawa, K., Miyano, H., Narabayashi, T., Iikura, T., Hayashi, M., Endoh, A., and Takehara, H., 1992, "The development of advanced nuclear primary loop recirculating pump (PLR Pump) for BWR plant considering thermal fatigue problem," Industrial and Environmental Applications of Fluid Mechanics, Proc. of the ASME Winter Annual Meeting, edited by Sherif et al., pp. 157-162.

Kato, H., Kanno, H., Hosokawa, M., Watanabe, A., Shitara, C., Ashizawa, K., Miyano, H., Narabayashi, T., Iikura, T., Hayashi, M., Endoh, A., and Takehara, H., 1993, "Experimental studies of temperature fluctuation phenomena for nuclear reactor primary loop recirculation pump (PLR Pump)," Proc. of the ICOPE.

King, G.P., Li, Y., Lee, W., Swinney, H.L., and Marcus, P.S., 1984, "Wave speeds in wavy Taylor-Vortex flow," J. Fluid Mech., Vol. 141, pp. 365-390.

Koschmieder, E.L., 1979, "Turbulent Taylor vortex flow," J. Fluid Mech., Vol. 93, pp. 515-527.

Kreith, F., 1968, "Convection heat transfer in rotating systems," Advances in Heat Transfer 5, Academic Press, New York, pp 129-251.

Kuo, D.C., and Ball, K.S., 1997, "Taylor-Couette flow with buoyancy: Onset of

spiral flow," Accepted for publication in Physics of Fluids.

Lai, W., 1962, "Stability of a revolving fluid with variable density in the presence of a circular magnetic field," Phys. Fluids, Vol. 5, No. 5, pp. 560-566.

Lee, Y.N., and Minkowycz, W.J., 1989, "Heat transfer characteristics of the annulus of two-coaxial cylinders with one cylinder rotating," Int. J. Heat Mass Transfer, Vol. 32, pp. 711-722.

Leonard, A., and Wray, A., 1982, "A new numerical method for the simulation of three-dimensional flow in a pipe.," In Proc. of the Eighth International Conference on Numerical Methods in Fluid Dynamics, Aachen, Lecture notes in Physics, vol. 170, Edited by E. Krause, Springer-Verlag, New York, pp. 335-342.

Marcus, P.S., 1984a, "Simulation of Taylor-Couette flow. Part 1. Numerical methods and comparison with experiment," J. Fluid Mech., Vol. 146, pp. 45-64.

Marcus, P.S., 1984b, "Simulation of Taylor-Couette flow. Part 2. Numerical results for wavy-vortex flow with one-travelling wave," J. Fluid Mech., Vol. 146, pp. 65-113.

Marcus, P.S., Orszag, S.A., and Patera, A.T., 1982, "Simulation of cylindrical Couette flow," In Proc. of the Eighth International Conference on Numerical Methods in Fluid Dynamics, Aachen, Lecture notes in Physics, vol. 170, Edited by E. Krause, Springer-Verlag, New York, pp. 371-376.

Meyer, K.A., 1967, "Time-Dependent numerical study of Taylor vortex flow," Phys. Fluids, Vol. 10, No. 9, pp. 1874-1879.

Moin, P., and Kim, J., 1980, "On the numerical solution of time-dependent viscous incompressible fluid flows involving solid boundaries," J. Comput. Phys., Vol. 35, pp. 381-392.

Moser, R.D., Moin, P., and Leonard, A., 1983, "A spectral numerical method for the Navier-Stokes equations with applications to Taylor-Couette flow," J. Comput.

Phys., Vol. 52, pp. 524-544.

Narabayashi, T., Miyano, H., Komita, H., Iikura, T., Shiina, K., Kato, H., Watanabe, A., and Takahashi, Y., 1993, "Study on temperature fluctuation mechanisms in an annulus gap between PLR Pump shaft and casing cover," Proc. of the second ICONE.

Neitzel, G.P., 1984, "Numerical computation of time-dependent Taylor-Vortex flows in finite-length geometries," J. Fluid Mech., Vol. 141, pp. 51-66.

Nissan, A.H., Nardacci, J.L., and Ho, C.Y., 1963, "The onset of different modes of instability for flow between rotating cylinders," A.I.Ch.E.J., Vol. 9, pp. 620-624.

Orszag, S.A., and Kells, L.C., 1980, "Transition to turbulence in plane Poiseuille and plane Couette flow," J. Fluid Mech., Vol. 96, pp. 159-205.

Patera, A.T., and Orszag, S.A., 1981, "Finite-amplitude stability of axisymmetric pipe flow," J. Fluid Mech., Vol. 112, pp. 467-474.

Pfister, G., Buzug, Th., and Enge, N., 1992,"Characterization of experimental time series from Taylor-Couette flow," Physica D, Vol. 58, pp. 441-454.

Press, W.H., Flannery, B.P., Teukolsky, S.A., and Vetterling, W.T., 1992, Numerical recipes in FORTRAN: the art of scientific computing, 2nd edn. Cambridge University Press, New York.

Roesner, K.G., 1978, "Hydrodynamic stability of cylindrical Couette-Flow," Arch. of Mech., Vol. 30, pp. 619-627.

Schuster, H.G., 1987, Deterministic chaos, VCH, Weinheim. West Germany

Schwarz, K.W., Springett, B.E., and Donnelly, R.J., 1964, "Modes of instability in spiral flow between rotating cylinders," J. Fluid Mech., Vol. 20, pp. 281-289.

Shih, A.C., 1994, "The study of Taylor-Couette flows with superimposed isothermal and heated axial flows at high Taylor numbers," Ph.D. thesis, California Institute of Technology.

Shih, A.C., and Hunt, M.L., "High-Taylor-Number Couette flows with a superposed isothermal or heated axial flow," presented at the 1992 Ntl. Heat Transfer Conf., San Diego, CA.

Shiina, K., Nakamura, S., Mizushina, Y., Yanagida, T., Endoh, A., Takehara, H., Narabayashi, T., Kato, H., and Watanabe, A., 1993, "Heat transfer characteristics of fluid flow in an annulus with an inner rotating cylinder having a labyrinth structure ," Proc. of the 3rd World Conference on Experimental Heat Transfer and Thermodynamics.

Singer, H.P., 1984, "Techniques of low pressure chemical vapor deposition," Semiconductor International, pp. 72-77.

Snyder, H.A., and Karlsson, S.F.K., 1964, "Experiments on the stability of Couette motion with a radial thermal gradient," Phys. Fluids, Vol. 7, No. 10, pp. 1696-1706.

Sorour, M.M., and Coney, J.E.R., 1979, "The effect of temperature gradient on the stability of flow between vertical, concentric, rotating cylinders," Int. Mech. Engr. Sci., Vol. 21, No. 6, pp. 403-409.

Strong, A.B., and Carlucci, L., 1976, "An experimental study of mass transfer in rotating Couette flow with low axial Reynolds numbers," Can. J. Chem. Engng, vol. 54, pp. 295-298.

Takens, F., 1981, "Detecting strange attractors in turbulence," in Lecture Notes in Mathematics 898, edited by D. Rand and L. S. Young, Springer, Berlin.pp.

Taylor, G.I., 1923, "Stability of a viscous liquid contained between two rotating cylinders," Phils. Trans. R. Soc. London, A, Vol. 223, pp. 289-343.

Walowit, J., Tsao, S., and DiPrima, R.C., 1964, "Stability of flow between arbitrarily spaced concentric cylinder surfaces, including the effect of a radial temperature gradient," Trans. ASME, Journal of Applied Mechanics, Vol. 31, pp. 585-592.

Watanabe, A., Takahashi, Y., Igi, T., Miyano, H., Narabayashi, T., Iikura, T., Sagawa, W., Hayashi, M., Endoh, A., Kato, H., Kanno, H., and Hosokawa, M., 1993, "The study of thermal fatigue problem on reactor recirculation pump on BWR plant," Proc. of the ICOPE.

White, F.M., 1991, Viscous fluid flow, 2nd edn. McGraw-Hill, New York.

Wood, H.G., 1983, Proc. Fifth workshop on gases in strong rotation, Charlottesville, Virginia.

Yih, C.S., 1961, "Dual role of viscosity in the stability of revolving fluids of variable density," Phys. Fluids, Vol. 4, No. 7, pp. 806-811.

Appendix A

The Treatment of the Boundary Conditions

The Navier-Stokes and the energy equations are given by:

$$\frac{\partial V}{\partial t} = -\nabla P - \frac{1}{R}\nabla \times \nabla \times V + V \times W + B \tag{A.1}$$

$$\frac{\partial T}{\partial t} + V \cdot \nabla T = \frac{1}{Pr\ R}\nabla^2 T \tag{A.2}$$

This can be re-written as:

$$L_1(V) = f \tag{A.3}$$

$$L_2(T) = g \tag{A.4}$$

where L_1 and L_2 are linear operators:

$$L_1(V) = \frac{\partial V}{\partial t} + \nabla P + \frac{1}{R}\nabla \times \nabla \times V \tag{A.5}$$

$$L_2(T) = \frac{\partial T}{\partial t} - \frac{1}{Pr\ R}\nabla^2 T \tag{A.6}$$

and

$$f = V \times W + B \tag{A.7}$$

$$g = -V \cdot \nabla T \tag{A.8}$$

Defining V' and T' such that:

$$V' = V - V_{CF} \tag{A.9}$$

$$T' = T - T_C \tag{A.10}$$

where V_{CF} and T_C are the analytical solutions of the Navier-Stokes and the energy equations for circular Couette flow. Now V' and T' satisfy the homogeneous boundary conditions. For the velocity field:

$$\begin{aligned} V' &= V - V_{CF} \\ L_1(V') &= L_1(V - V_{CF}) \\ &= L_1(V) - L_1(V_{CF}) \\ &= f - L_1(V_{CF}) \\ &= V \times (\nabla \times V) + B - L_1(V_{CF}) \\ &= (V' + V_{CF}) \times (\nabla \times (V' + V_{CF})) + B - L_1(V_{CF}) \end{aligned} \tag{A.11}$$

The right hand side of the previous equation gives the nonlinear terms for the Navier-Stokes equations. Similarly, for the temperature field:

$$
\begin{aligned}
T' &= T - T_C \\
L_2(T') &= L_2(T - T_C) \\
&= L_2(T) - L_2(T_C) \\
&= g - 0 \\
&= -V \cdot \nabla T \\
&= -(V' + V_{CF}) \cdot \nabla (T' + T_C) \qquad \text{(A.12)}
\end{aligned}
$$

The nonlinear terms for the energy equation is given by the right hand side of the above equation.

Appendix B

Derivation of Colburn's Analogy for Taylor-Couette Flow

The empirical formula given by Colburn is:

$$St.f(Pr) = C_f/2 \tag{B.1}$$

where St is the Stanton number and C_f is the friction factor as defined below.

$$St = \frac{h_{\overline{\theta},\overline{z},\overline{t}}}{\rho(\omega r_i)C_p} \tag{B.2}$$

$$C_f = \frac{\tau_w|_{\overline{\theta},\overline{z},\overline{t}}}{\frac{1}{2}\rho(\omega r_i)^2} \tag{B.3}$$

Also

$$h_{\overline{\theta},\overline{z},\overline{t}} = -\frac{k}{b}\frac{\partial T}{\partial r}\bigg|_{\overline{\theta},\overline{z},\overline{t}} \tag{B.4}$$

$$\tau_w|_{\overline{\theta},\overline{z},\overline{t}} = \frac{\mu(\omega r_i)}{b}\frac{\partial u_\theta}{\partial r}\bigg|_{\overline{\theta},\overline{z},\overline{t}} \tag{B.5}$$

For circular Couette flow, at the inner wall:

$$\left.\frac{\partial T}{\partial r}\right|_{\overline{\theta},\overline{z},\overline{t}} = \frac{1}{r_i}\frac{1}{\ln \eta} \tag{B.6}$$

$$\left.\frac{\partial u_\theta}{\partial r}\right|_{\overline{\theta},\overline{z},\overline{t}} = \frac{1}{r_i}\frac{1+\eta^2}{1-\eta^2} \tag{B.7}$$

Substituting Eqns. (B.2), (B.3), (B.4), (B.5), (B.6) and (B.7) in Eqn. (B.1):

$$f(Pr) = Pr(\ln \eta)\frac{\eta^2+1}{\eta^2-1} \tag{B.8}$$

As $\eta \to 1$, $(\ln \eta)^{\frac{\eta^2+1}{\eta^2-1}} \to 1$ and $f(Pr) \to Pr$. Hence for circular Couette flow:

$$St.Pr = C_f/2 \tag{B.9}$$